Physically Motivated Registration of Diagnostic CT and PET/CT of Lung Volumes

Habib Yusufi Baluwala

St Edmund Hall

Supervised by: Dr Julia Schnabel

Dr Kinda Saddi

Trinity Term, 2012.

This D.Phil Thesis is submitted to the

Department of Engineering Science, University of Oxford.

This thesis is submitted to the Department of Engineering Science, University of Oxford, in partial fulfillment of the requirements for the degree of Doctor of Philosophy. The thesis is entirely my own work, and expect where otherwise stated, describes my own research.

Habib Baluwala, St Edmund Hall, Oxford.

Abstract

Lung cancer is a disease affecting millions of people every year and poses a serious threat to global public health. Accurate lung cancer staging is crucial to choose an appropriate treatment protocol and to determine prognosis, this requires the acquisition of contrast-enhanced diagnostic CT (d-CT) that is usually followed by a PET/CT scan. Information from both d-CT and PET scan is used by the clinician in the staging process; however, these images are not intrinsically aligned because they are acquired on different days and on different scanners. Establishing anatomical correspondence, i.e., aligning the d-CT and the PET images is an inherently difficult task due to the absence of a direct relationship between the intensities of the images. The CT acquired during the PET/CT scan is used for attenuation correction (AC-CT) and is implicitly aligned with the PET image as they are acquired at the same time using a hybrid scanner. Patients are required to maintain shallow breathing for both scans. In contrast to that, the d-CT image is acquired after the injection of a contrast agent, and patients are required to maximally inhale, for better view of the lungs. Differences in the AC-CT and d-CT image volumes are thus due to differences in breathhold positions and image contrast. Nonetheless, both images are from the same modality. In this thesis, we present a new approach that aligns the d-CT with the PET image through an indirect registration process that uses the AC-CT. The deformation field obtained after the registration of the AC-CT to d-CT is used to align the PET image to the d-CT.

Conventional image registration techniques deform the entire image using homogeneous regularization without taking into consideration the physical properties of the various anatomical structures. This homogeneous regularization may lead to physiologically and physically implausible deformations. To register the d-CT and AC-CT images, we developed a 3D registration framework based on a fluid transformation model including three physically motivated properties: (i) sliding motion of the lungs against the pleura; (ii) preservation of rigid structures; and (iii) preservation of topology. The sliding motion is modeled using a direction dependent regularization that decouples the tangential and the normal components of the

external force term. The rigid shape of the bones is preserved using a spatially varying filter for the deformations. Finally, the topology is maintained using the concept of log-unbiased deformations. To solve the multi-modal registration problem due to the contrast injected for the d-CT, but lack thereof in the AC-CT, we use local cross correlation (LCC) as the similarity measure. To illustrate and validate the proposed registration framework, different intra-patient CT datasets are used, including the NCAT phantom, EMPIRE10 and POPI datasets. Results show that our proposed registration framework provides improved alignment and physically motivated deformations when compared to the classic elastic and fluid registration techniques.

The final goal of our work was to demonstrate the clinical utility of our new approach that aligns d-CT and PET/AC-CT images for fusion. We apply our method to ten real patients. Our results show that the PET images have much improved alignment with the d-CT images using our proposed registration technique. Our method was successful in providing a good overlap of the lungs, improved alignment of the tumours and a lower target registration error for landmarks in comparison to the classic fluid registration. The main contribution of this thesis is the development of a comprehensive registration framework that integrates important physical properties into a state-of-the-art transformation model with application to lung imaging in cancer.

Acknowledgments

This work would not be possible without the guidance of my advisors Dr. Julia Schnabel on the university side and Dr. Kinda Saddi from Siemens Molecular Imaging. I would like to thank them for their immense patience, invaluable guidance and the thorough advice that they have provided through the journey of my D.Phil. Their passion for research and dedication to the field of medical imaging has encouraged me throughout the project. They have also guided the evolution of my technical writing and made me see the value of using the right word at the right place. I would like to thank Dorothy Hodgkin postgraduate awards for funding my work in collaboration with the university and Siemens Molecular Imaging.

I am grateful to Sir Mike Brady whose intellectual power, enlightening guidance and steadfast optimism have always inspired me to work better and also feel confident that I will make it through in the worst of crisis. My gratitude also goes to Dr. Timor Kadir and Dr. Jerome Declerck for their continued support and guidance throughout this journey.

I am grateful to many individuals within the IBME and the Siemens Oxford lab that have supported me throughout my doctoral study. To name just a few, a hearty thanks goes to: Wen Chi (Jim), Matthias Heinrich, Sana Fathima, Ivor Simpson, Mitchell Chen, Bahbibi Rahmatullah, Syed Ahmar Shah, Manav Bhushan, Amalia Cifor, Gordon Stevenson, Matthew Kelly, Syed Ahmar Shah and Vaclav Potesil. All of you have made my time in the lab very enjoyable.

Finally, I also thank my parents and my family for providing me the freedom and the strength to pursue my dreams and goals. Without their love and affection, I would have never achieved as much as I have.

Glossary

PET	Positron emission tomography
CT	Computed tomography
MRI	magnetic resonance imaging
NMI	Normalized Mutual Information
AC-CT	attenuation corrected CT
d-CT	diagnostic CT
SSD	sum of squared differences
MI	mutual information
CC	cross correlation
NCC	normalized cross correlation
DSC	dice similarity coefficient
ANTs	advanced normalization tools
FDG	fluoro-deoxy-glucose
HU	Hounsfield unit
ITK	Insight Segmentation and Registration Toolkit
NCAT	NURBS-based cardiac torso phantom
ROI	region of interest
SCLC	small cell lung cancer
NSCLC	non-small cell lung cancer
EMPIRE	Evaluation of Methods for Pulmonary Image Registration
TRE	target registration error
PDE	partial differential equation

List of Publications - Habib Baluwala

Journal articles

1. Habib Y. Baluwala, Laurent Risser, Kinda A. Saddi, Julia A. Schnabel.

Towards physiologically motivated registration of diagnostic CT and PET/CT of lung volumes.

Journal of Medical Physics, 2013 (40).

http://dx.doi.org/10.1118/1.4771682

2. Laurent Risser, François-Xavier Vialard, Habib Y. Baluwala, Julia A. Schnabel.

Piecewise-diffeomorphic image registration: application to the motion estimation between 3D CT lung images with sliding conditions.

Medical Image Analysis, 2013 (17) : 182–193.

http://dx.doi.org/10.1016/j.media.2012.10.001

3. Habib Baluwala, Kinda A. Saddi, Julia A. Schnabel.

Non-rigid chest image registration with preservation of topology and rigid structures.

British Machine Vision Annals, 2011 (4) : 1-15.

http://www.bmva.org/annals/2011/2011-0004.pdf

Conference articles

1. Habib Y. Baluwala, Kinda A. Saddi, Julia A. Schnabel.

Elastic registration of chest CT images with log-unbiased deformations and rigidity constraint.

In Proc. IEEE 8th International Symposium on Biomedical Imaging: From Nano to Macro, 2011 (March 30 2011-April 2 2011, Chicago, IL), pp 1235-1238.

Eds: S Wright, X Pan, M Liebling.

http://dx.doi.org/10.1109/ISBI.2011.5872625

2. Laurent Risser, Habib Y. Baluwala, Julia A Schnabel.

Diffeomorphic registration with sliding conditions: Application to the registration of lungs CT.

In Proc. The Fourth International Workshop on Pulmonary Image Analysis (in association with MICCAI 2011, Toronto, CA, 2011), pp 79-90.

Eds: R Beichel, A Kiraly, J-M Kuhnigk, J McClelland, K Mori, E van Rikxoort, S Rit, M de Bruijne, B van Ginneken, S Kabus.

http://www.lungworkshop.org/2011/

3. Habib Y. Baluwala, Kinda A. Saddi, Julia A. Schnabel.

Log-unbiased elastic image registration with spatial constraint for 3D CT lung images.

In Proc. of Medical Image Understanding and Analysis (Warwick, July 2010).

Eds: A.H. Bhalerao, N.M. Rajpoot. ISBN: 978-0-9566150-0-8

http://www2.warwick.ac.uk/fac/sci/dcs/events/past/miua2010/proceedings/paper_35.pdf

Contents

Chapter 1

Introduction

1.1 Background

Lung cancer is the most common cause of cancer related deaths among men and women in developed countries and the third most frequent cause of death in general. Globally, it is responsible for 1.3 million deaths annually and with 1.6 million new cases being diagnosed every year [1]. In 2008, around 40,800 people were diagnosed with lung cancer in the United Kingdom [2]. Tobacco smoking is the primary cause of lung cancer, responsible for over 80% of cases [3]. The spread of tobacco use among the large middle class populations in developing countries like India and China has also led to a drastic increase in the incidence of lung cancer globally [4, 5]. Lung cancer is also prevalent among non-smokers due to passive smoking, occupational exposure to pollutants and genetic factors [6].

Cancer is a generic term used for a large group of diseases characterized by uncontrolled, abnormal cell division and growth. Lung cancer refers to the cancer that grows in the tissue of the lungs, usually in the epithelial cells of the lining air passages. As the cancer spreads through the lungs, it can restrict the flow of oxygen by obstructing the bronchus. It can also block off a part of the lung, causing it to collapse. Lung cancer is classified into two main types based on the size of the malignant cancer cells:

(a) Small cell lung cancer (SCLC) is highly aggressive and constitutes about 20-25% of all lung cancer cases. SCLC evolves very fast and has a poor prognosis.

Stage 0	Cancer in situ, i.e., tumour has not grown through lung lining.
Stage I	Cancer is very localized and is no bigger than 3cm in size.
Stage Ib	Cancer is larger than 3cm in size or has spread to the pleural membrane.
Stage IIa	The cancer is small and measures 3cm or less and affects the nearby lymph nodes.
Stage IIb	Cancer is larger than 3cm and spread to lymph nodes or the tumour has caused the lungs to collapse.
Stage IIIa	Cancer may be of any size and is found in the lymph nodes on the same side of the chest.
Stage IIIb	Cancer has spread to any side of the chest and another major structure like the heart or the windpipe
Stage IV	Cancer has spread to a distant part of the body such as the liver, bones or the brain

Table 1.1: Various stages of lung cancer [7].

(b) Non-small cell lung cancer (NSCLC) is a form of epithelial lung cancer. It is the most common kind of lung cancer affecting around 70% of all lung cancer patients. It evolves at a slower rate and has a better prognosis in comparison to SCLC.

Lung cancer can also spread to other regions of the body like the bones, liver and adrenal glands through the lymph nodes. This spread of cancer to other parts of the body is known as metastasis. The extent or the severity of the cancer is determined by a process called staging. Cancer staging takes into account the size and the number of cancerous tumours, the spread of cancer to nearby (regional) lymph nodes, and also any distant metastasis that have occurred on the body. Most tumours can be described as stage 0, stage I, stage II, stage III and stage IV. Some of these stages are further broken down into subgroups such as stage IIIa, IIIb and so forth. Stage 0 refers to the tumour being dormant or in early form, while stage IV refers to an advanced stage where the cancer has metastasized and spread to other parts of the body. Table 1.1 provides a brief overview of the classification for the various stages of lung cancer based on severity and extent of the tumours.

Lung cancer remains a disease with poor prognosis. It has the lowest survival rates compared to other cancers like prostate, breast and colorectal cancers [2]. More than two-thirds of the lung cancer cases are diagnosed at a later stage which reduces the survival rates

for patients. Overall, less than 20% of lung cancer patients survive the disease for at least five years after diagnosis [8]. The stage of the disease mainly dictates the chances of survival for the patient as shown in Figure 1.1. Detection of the disease at an earlier stage improves the chance of a 5 year survival rate significantly. Survival rates for early stages of cancer are quite high, sometimes reaching 80%, as reported in some studies [9]. Staging is used solely to determine the most appropriate treatment and can also help in prognosis. Existing treatments options for lung cancer include chemotherapy, radiotherapy, surgical resection and immunotherapy. These treatments can be used individually or in combination depending on the staging of the disease. Accurate clinical staging of lung cancer is required to stratify the patients into correct treatment protocols. An incorrect staging may result in the resection of benign nodules or early relapse after surgery. Hence, high sensitivity and specificity are required to establish proper staging.

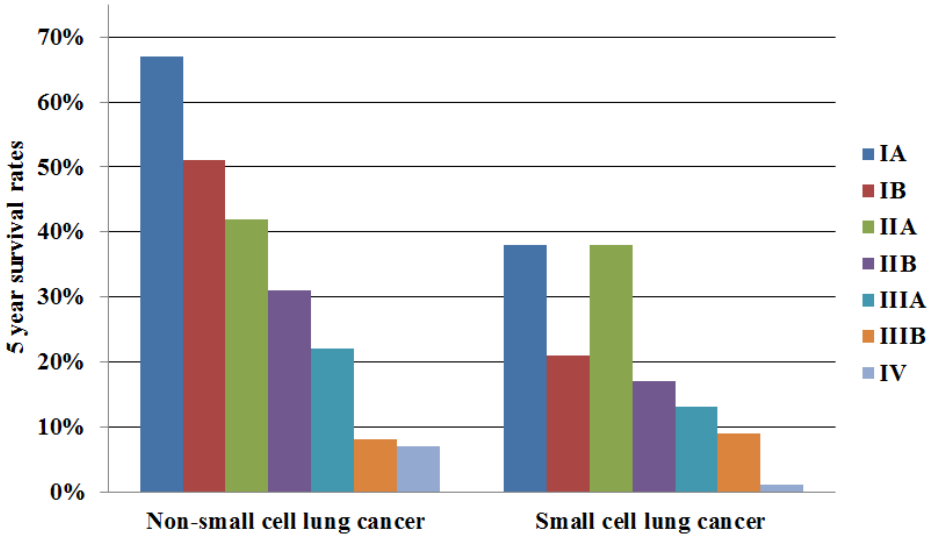

Figure 1.1: Survival rates for up to 5 years for lung cancer patients in England and Wales depending on the respective stages [10].

Non-invasive staging of lung cancer is achieved by using various imaging techniques to assess the extent and spread of the tumour. Conventional chest radiography is the means by which the lung cancer is incidentally first identified. It provides a coarse measurement of the primary tumour size and may give some information regarding the spread of the tumour to the lymph nodes. However, computed tomography (CT) provides an enhanced visualization

of the tumour and thus the means for a more accurate measurement of the tumour size. It also helps to assess the extent of intra-thoracic invasion of the tumour. The effectiveness of using CT over chest radiography is demonstrated by the National Lung Cancer screening trial which has announced in November 2010 that 20% fewer lung cancer deaths were seen among those who were screened with low-dose CT than with chest radiography [11]. However, it was also found that a large proportion of the lesions detected using CT were false positives, i.e., they were benign [12]. Positron emission tomography (PET), a functional imaging technique, can differentiate malignant from benign tumours, can detect the presence of metastases and also provide information on lymph node involvement. Studies have also established that PET, when used with CT, can help to minimize unnecessary invasive biopsy procedures for benign lesions by reducing the false positive findings of the CT [13]. A combination of CT and PET can also be used for quantifying the lung tumour response to therapy, and in detecting recurrence in previously treated lesions [14].

Novel magnetic resonance imaging (MRI) techniques allow for high resolution image acquisition of lung and pulmonary tumours during the respiratory cycle. MRI scanning does not involve exposure to radiation, so it can be safely used in people who may be vulnerable to the effects of radiation, such as pregnant women. They are also useful for showing soft tissue structures, such as ligaments and cartilage, and organs such as the brain, heart and eyes [15]. MRI allows for multiple and repeated measurements and can be used to assess motion and perfusion of the thoracic organs. Advances in MRI technology have helped to establish a complex technology such as cardiac MRI, which combines morphological information (wall thickness, edema, scarring of the myocardium) with functional assessment (wall motion, contractility, ejection fraction) and viability/perfusion (e.g. at rest and during stress) .

Though MRI possesses great potential, it suffers from some basic shortcomings. The main disadvantage of using MRI over CT is the related cost of the scan. MRI scanners are very expensive and a single scanner can cost over £1 million. Given the high investment into MRI equipment and the running costs for maintenance and personnel, the choice of MRI over CT needs to be justified by added diagnostic value that the modality can offer.

Other limitations for MRI include its restricted used for patients with metal pacemakers or other metal implants. MRI acquisitions involve longer scanning times, hence are affected by patient movement, making them unsuitable for investigating problems such as mouth tumours because coughing or swallowing can make the images that are produced less clear. People who are morbidly obese cannot fit into borehole of the MRI system. Hence, the current use of MRI techniques is limited to research studies, while clinically, CT and PET are the established gold standard for non-invasive staging of lung cancer [16].

In the following sub-sections, we review CT and PET imaging modalities including their advantages and limitations and explain the potential of fusing CT and PET images.

1.1.1 Computed Tomography

The first prototype of the computed tomography (CT) scanner was designed by Godfrey Hounsfield and Allan Cormack in 1971. CT imaging uses multiple X-ray projections to reconstruct the 3D structure of the body. The images are acquired by rotating an X-ray tube around the body and the transmitted radiation is measured by sensors placed on the gantry. The three dimensional CT image volume is generated from the large series of cross-sectional two-dimensional images of the body. Since the development of the first CT scanner, CT the imaging technology has gone through several phases or generations. The classification of these new CT systems is based upon the arrangement of components and mechanical motion used to collect the data. Each generation has a number associated with it but a higher generation number does not necessarily mean a superior performance system. The various generations and its features are presented in Table 1.2. Schematic diagrams of the CT generations are also shown in Figure 1.2-1.5.

The intensity readings of the transmitted radiation provide the linear attenuation coefficient of the body. A linear attenuation coefficient is a quantity that characterizes how easily the body can be penetrated by the X-ray beam, i.e., the radiological density of the body. Each voxel is assigned a numerical value, which is the average of all the linear attenuation coefficients contained within the corresponding voxel. This number is compared to the at-

CT Generation	**Design description**	**Features**
I	Single X-Ray source with a single dectector (Figure 1.2)	- Simple in design - Earliest versions took around 4.5 minutes for a single scan
II	Introduced Multiple detectors in a single row (Figure 1.3)	- Improved resolution and speed of image acquisition in comparison to the Ist generation -Latest IInd generation CT scanners allows image acquisition in a single breathhold -IInd generation scanners were translate and rotate scanners
III	Replaced a single row of detectors with an arc-shaped row of detectors.(Figure 1.4)	-Replaced the need for translation motion in the x-ray anode and detectors - Made it possible to use high power, rotating anode x-ray tubes
IV	Uses a stationary circular array of detectors (Figure 1.5)	- Eliminates the need to rotate the detectors - Scanners are expensive as it requires a larger number of detectors to achieve the same resolution and dose efficiency as the third generation
V	Includes a ring of X-ray tubes that circles the patient instead of a ring of detectors	- Primary use of Vth generation CT scanners is for cardiac tomographic imaging and is capable of 50 ms scan times

Table 1.2: CT generations

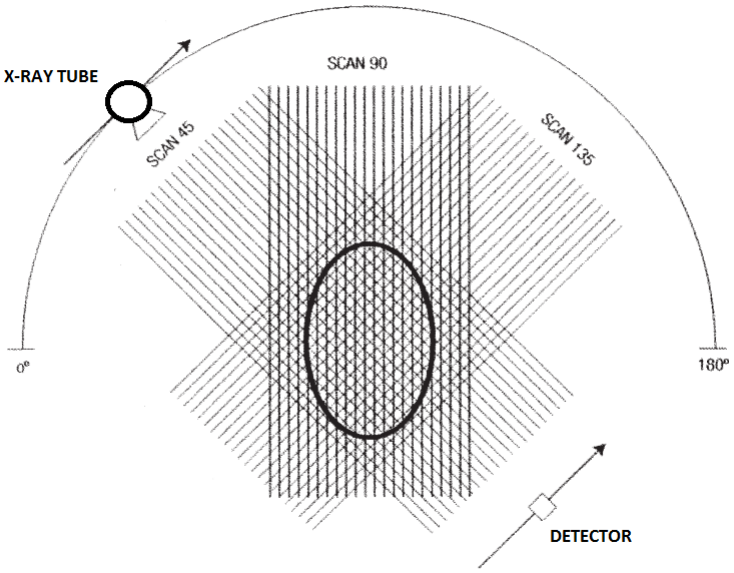

Figure 1.2: Ist generation: Linear and rotating pencil beam system. [17]

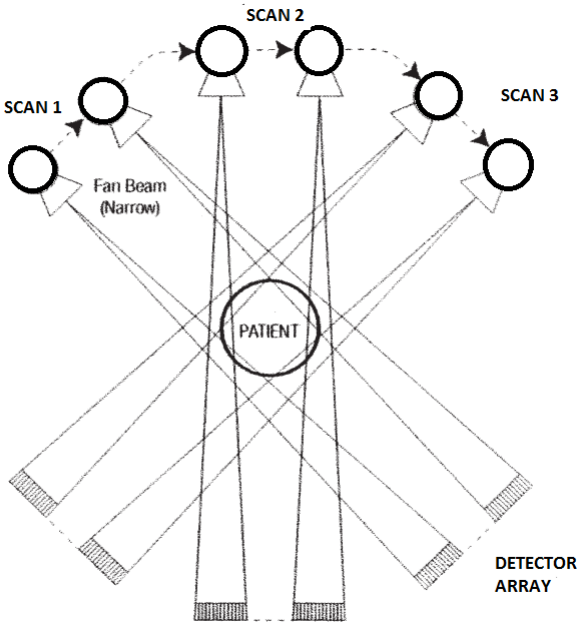

Figure 1.3: IInd generation : Linear and rotating fan beam system. [17]

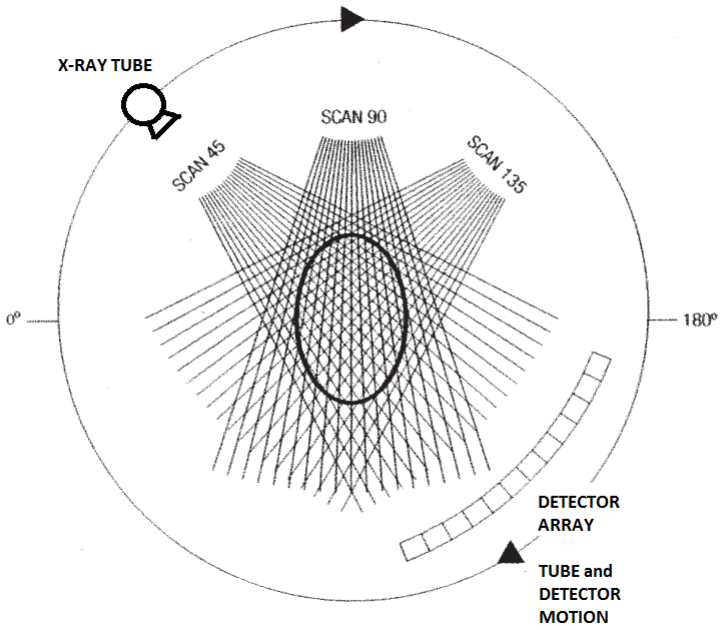

Figure 1.4: IIIrd generation: Rotation only (tube and detectors) wide angle fan beam system. [17]

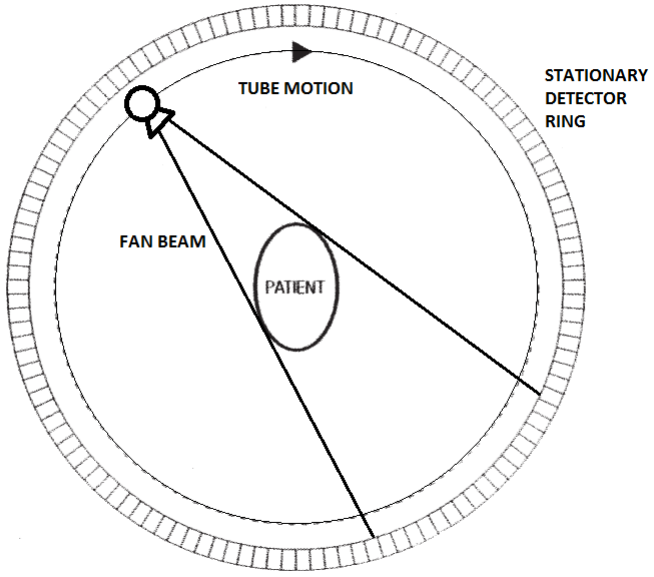

Figure 1.5: IVth generation: 360 degree detector ring-rotating tube system. [17]

tenuation value of water and displayed as scaled units called the Hounsfield Units (HU). The scale assigns water a HU value of zero. In a voxel with average linear attenuation coefficient μ_Y, the corresponding HU is given by:

$$HU = 1000 \times \frac{\mu_Y - \mu_{Water}}{\mu_{Water}}, \tag{1.1}$$

where μ_{Water} is the linear attenuation coefficient of water. Typical HU values for human tissues such as bones, fat, water, lungs, blood and muscles is provided in Table 1.3. Modern CT scanners are calibrated to yield images within the accuracy of a few HU.

Tissue Type	**Hounsfield Units**
Bone (ribs, vertebrae, etc)	+400 to +1000
Soft tissues (liver , muscle, kidney, etc)	+20 to +120
Water	0
Fat	-60 to -200
Lungs	-700
Air	-1000

Table 1.3: Hounsfield units value calculated for various tissues based on the density of water [18].

CT is the radiographic imaging method of choice for lung cancer detection and staging. Two advantages of CT in particular have made it the ideal choice for chest imaging. A very high resolution in the axial plane provides anatomical details of the lungs similar to that available from pathology specimens [19]. Modern medical CT scanners acquire images with a high spatial resolution (as high as 0.5 mm). The other advantage of CT imaging is the large difference in the attenuation values between biological tissue and air which provides a very good contrast between the lungs and its surrounding structures. Bones and water are also clearly distinguishable from the soft tissues. CT images also serve as a tool to decide on the approach for biopsy of the lymph nodes. Lymph node diagnosis on CT is based on significant enlargement of the node (>1.0cm) [20]. However, there are also certain limitations of CT. Different soft tissues share the same intensity range on the Hounsfield unit scale, which implies low soft tissue contrast. CT images can fail to provide accurate tumour definition (i.e. size, and shape) if the tumour is the same density as the normal tissues surrounding

it. This is especially true for organs of the mediastinum. Other concerns for using CT are related to the harmful effects of radiation exposure.

Most diagnostic scans for lung cancer are performed after an intravenous administration of a contrast agent. The CT contrast medium is used to improve the delineation of the vessels to increase the sensitivity and accuracy of lesion detection and characterization [21]. CT contrast agents are available in different forms, but iodine based agents are widely used in hospitals. The CT volumes acquired with the administration of the contrast agent are generally referred to as diagnostic CT (d-CT). An example of the d-CT scan is shown in Figure 1.6.

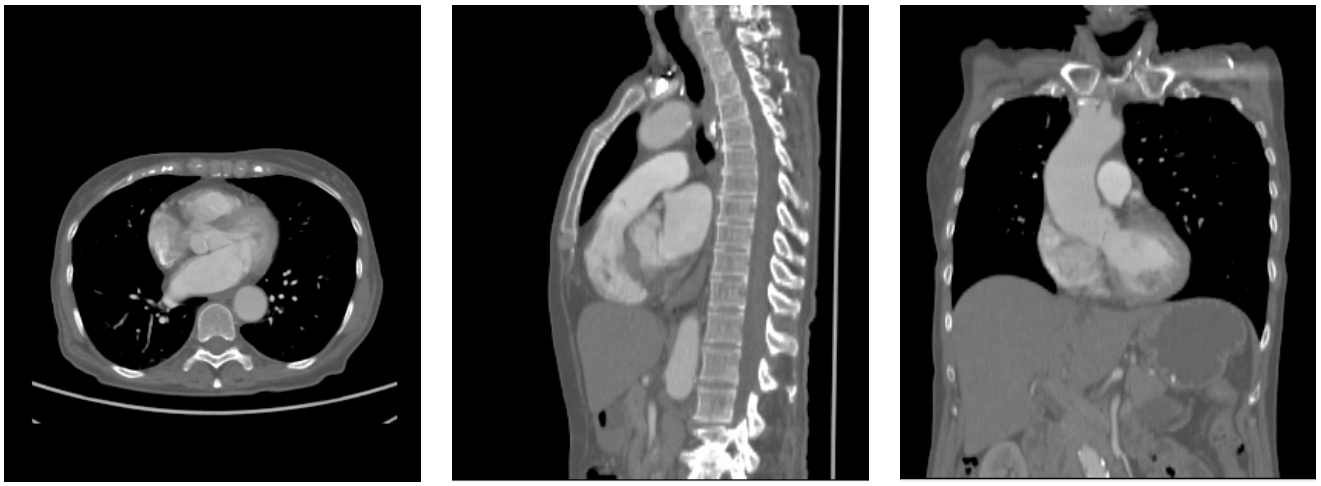

(a) An axial slice (b) A sagittal slice (c) A coronal slice

Figure 1.6: An example of diagnostic CT scan of the chest. The axial, coronal and sagittal slices are extracted from a three dimensional scan.

1.1.2 Positron Emission Tomography

First developed in the late 1950s by David Kuhl and Roy Edwards [22], positron emission tomography (PET) is an imaging technique that maps the metabolic activity of the body. A short lived radioactive tracer isotope that is biologically active is injected into the patient. The radioactive tracer is labelled with a positron emitting isotope such as ^{18}F, ^{15}O, ^{11}C or ^{64}Cu. A list of commonly used radioactive tracers and the biological activities that they are used to detect is provided in Table 1.4.

Fluoro-deoxy-glucose (FDG), a glucose analogue that is labeled to the radioactive positron

emitter Fluorine-18, is the most commonly used radioactive tracer in PET imaging. FDG has biological properties similar to glucose. FDG injected into the patient travels through the body via the circulatory system. The tracer gets accumulated in regions of high metabolic activity and is taken up by high glucose using cells such as the brain and tumours. FDG is used as a marker to show the distribution of glucose metabolic activity in PET imaging. Most tumours use glucose as their primary energy substrate for fueling cell division and growth. The increased glucose uptake of these cancer cells can be identified and localised in FDG-PET images. The positrons emitted by the radioactive tracer get annihilated within the body and produce gamma rays which travel in opposite directions, as illustrated in Figure 1.7. These gamma rays are detected by gamma detectors. The reconstructed PET image intensities are proportional to the counts of the gamma rays detected by the cameras. The PET image helps to map the location of the tracer within the body. PET scanning is used for diagnosis, staging and follow-up of various malignancies. FDG-PET scanning has better sensitivity than CT scanning in the detection of distant metastases in patients with NSCLC and SCLC [24]. FDG-PET also helps in accurate staging of mediastinal nodes [25]. However, one limitation of PET imaging is that it has a low resolution compared to other modalities.

Tracer	**Biological Process**
FDG	Glucose metabolism
^{18}FMISO	Hypoxia
^{64}Cu-ATSM	Hypoxia
^{18}FLT	Proliferation
$H_2^{15}O$	Blood flow
^{11}C-methionine	Amino acid uptake
^{18}F-dopa	Dopamine storage

Table 1.4: Commonly used radiotracers for PET imaging [23].

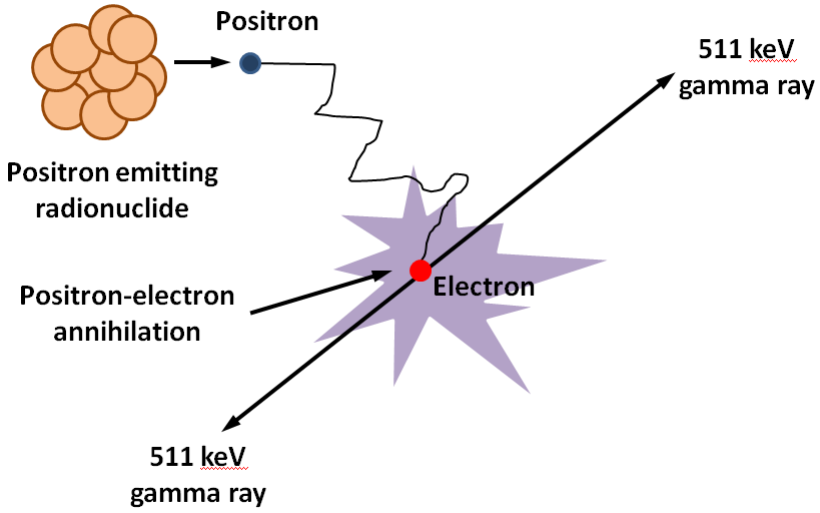

Figure 1.7: Positron emission and positron-electron annihilation.

As the gamma rays travel through the different layers of tissue with varying thickness and density, they get attenuated. The loss of counts due to attenuation causes a false reading which shows lower tracer uptake in deeply situated organs. A low dose CT scan is acquired to construct an attenuation map of density differences throughout the body that can be used to correct for the absorption of the gamma rays. This information is used to correct for the counts in areas that are more attenuated due to the presence of dense structures or areas that are deeply situated. The low dose CT image acquired to correct for the attenuation errors is generally known as the attenuation correction CT (AC-CT). Integrated PET/CT scanners are currently used in many healthcare centers to facilitate faster acquisition and better alignment. This ultimately helps in improving diagnostic accuracy and localisation of tumours. An example of the attenuation corrected PET image and the AC-CT is shown in Figure 1.8.

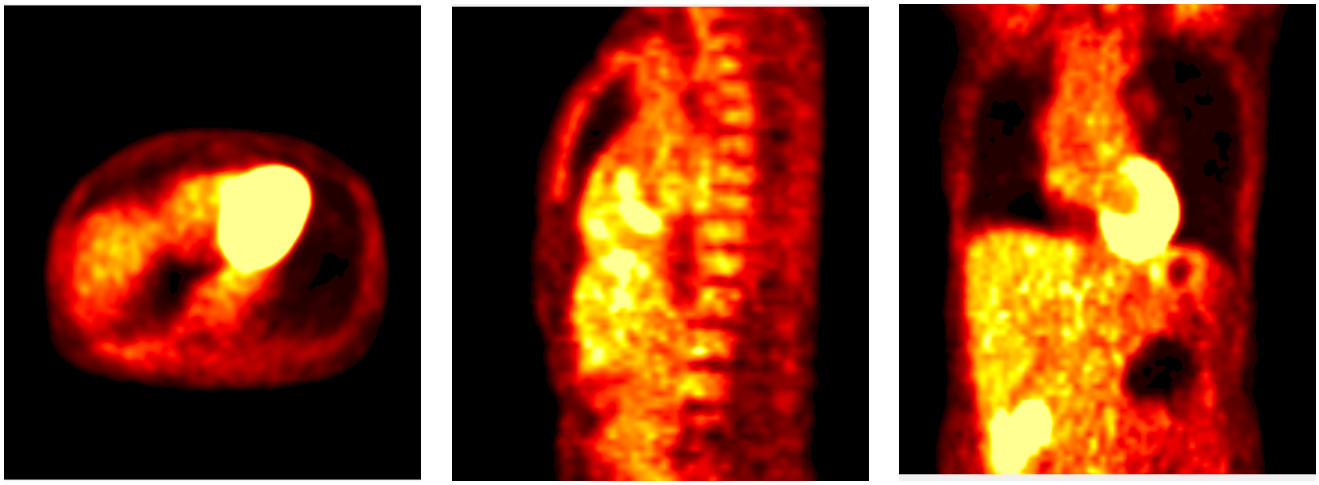

(a)An axial slice (b)A sagittal slice (c)A coronal slice

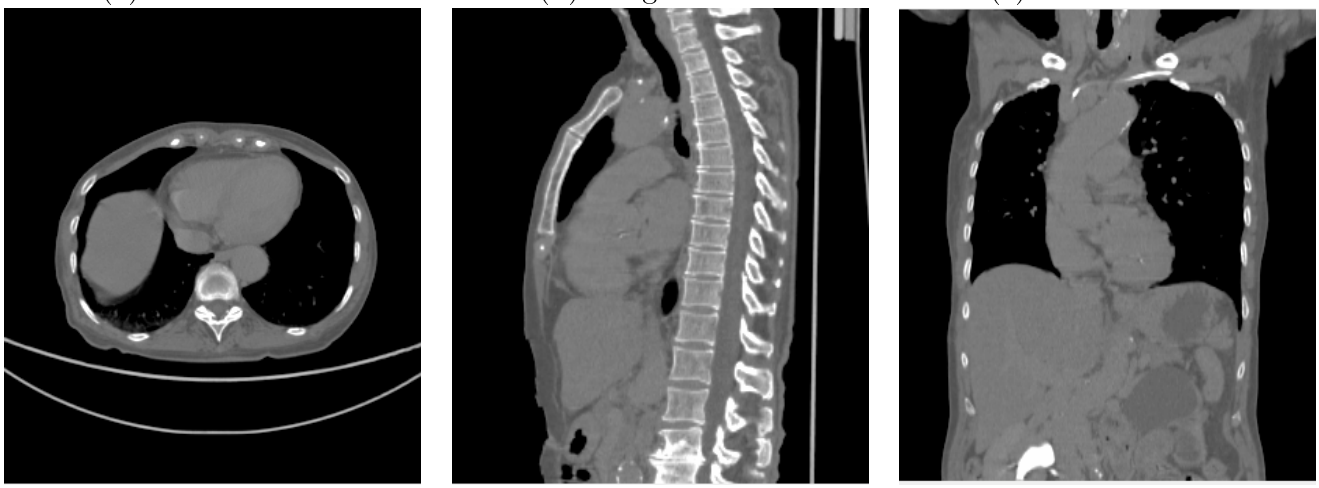

(a)An axial slice (b)A sagittal slice (c)A coronal slice

Figure 1.8: An example of an attenuation corrected PET image (top row) and AC-CT (bottom row).

1.1.3 Radiation Exposure

Whole-body PET/CT scanning is accompanied with a substantial radiation dose and cancer risk. CT alone can deliver a radiation dose which 100-500 times the amount of radiation associated with an ordinary X-ray. Thus, CT and PET examinations should be clinically justified by radiologists, and measures should be taken to reduce the dose. The exposure dose for ionizing radiation is expressed in mSv (milli-Sieverts). mSv is a quantity that represents the stochastic biological effects of radiation. Everyone is exposed to a certain amount of background radiation - about three mSv a year from cosmic rays, radon gas and the earth's radioactive elements. The average radiation doses for various procedures are expressed in

Diagnostic exams	Approximate radiation exposure during exam expressed in mSv
X-ray of the chest	0.04
Mammogram	2 to 5
CT scan of the head	1.4
CT scan of the chest	6.6
Whole body CT scan	10
PET tumour scan	14.1
Coronary Angiogram	4.6 to 15.8

Table 1.5: Radiation exposure during various medical imaging exams.[26, 27]

Table 1.5. For people working with radiation (Nuclear reactors, X-ray labs), 20 mSv is the UK legal limit, as set by the Ionising Radiations Regulations (1999), that a classified person who works with radiation may be exposed to in any given year. Workers normally receive considerably less than this. However, patients who undergo medical imaging procedures are not monitored or limited, and since the amount of radiation varies from patient to patient, from test to test and from machine to machine, there's no way of knowing exactly how much radiation we're getting.

1.2 Clinical Problem and Motivation

In current lung cancer clinical protocols, the d-CT is used as the primary modality to image the tumour pathology and the surrounding structures, largely due to the short acquisition time (takes generally few seconds), high resolution and image contrast. The d-CT is acquired at maximum inspiration to give a better view of the fully expanded lung tissue. After confirmation of the presence of tumours in the d-CT, the patient is recommended for a whole body acquisition of PET volume using an integrated PET/CT scanner. The PET image is acquired over a period of 30-40 minutes at shallow breathing. This results in a reconstructed static PET image that is blurred due to patient breathing and other motion artifacts occurring during the acquisition. The AC-CT used for attenuation correction of the PET image is acquired using a free-breathing protocol.

Image fusion is defined as the process of combining relevant information from two or

more different images into a single highly informative image. Fusing the anatomical and the metabolic information helps to combine two complementary sets of information into a single visualization. In practice, fusion of medical images is carried out by overlaying the two images over each other and then adjusting the transparency of each image to visualize a maximum amount of information. Fusing the PET and AC-CT helps to visually observe the metabolic activity and the anatomical information of the body in a single image. An example of visual fusion of the aligned PET and AC-CT images is shown in Figure 1.9(a). The fusion of these images is helpful in identifying and locating the tumours. PET-CT fusion was found to help identify positive nodes that were not considered malignant on CT, as well as to enhance tumour definition for poorly defined tumours [28, 29]. Image fusion can also be used for radiotherapy planning and for longitudinal studies of tumour response [30, 31, 32]. The combination of PET and CT has been shown to provide the best available information for lung cancer and is recommended for use in clinical practice by the IAEA expert group [33]. PET and AC-CT image fusion is easily obtained as the various structures within the images are implicitly aligned with each other due to their acquisition from the same scanner.

Similar to the PET and AC-CT fusion, fusing the d-CT and PET scans might facilitate better diagnosis and staging [34, 35, 36]. However, the PET and the d-CT images are not anatomically aligned with each other. Hence, a direct visual fusion without proper mapping of the anatomical structures can be misleading. An example of directly fused image volumes of d-CT and the PET image is shown in Figure 1.9(b) where the structures like the liver, lymph nodes and tumours are clearly misaligned between the d-CT and the PET image. There are two reasons for this misalignment: (1) the images are acquired in two different scanners, so the patients have been repositioned and (2) there is a difference in the breathing phases of the image acquisition protocols. Without correct anatomical mapping between the PET and d-CT, the fusion between the images is **clinically irrelevant**. Current clinical practice require reading the PET/CT and the d-CT separately on different screens and then mentally correlating the structures.

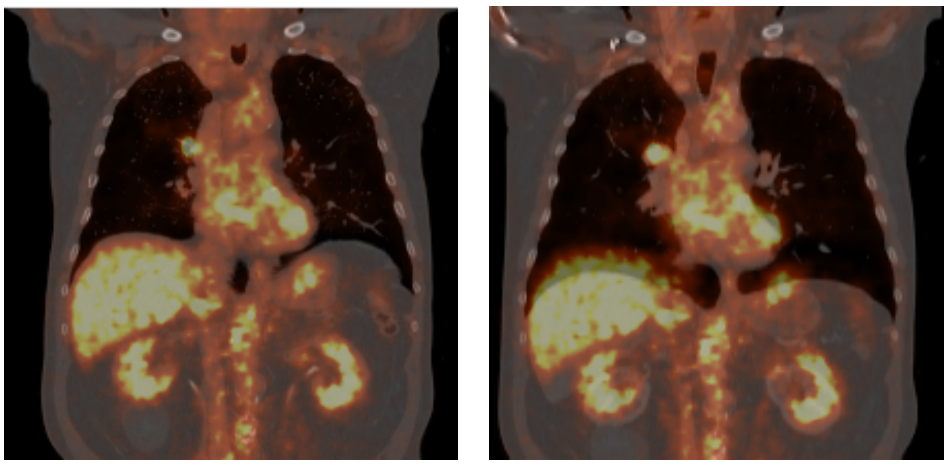

(a) (b)

Figure 1.9: (a) Fused PET/ AC-CT image (inherently registered as they are acquired from the same scanner) (b) Fused PET/D-CT (contrast-enhanced) image without registration.

Establishing a correct alignment of the anatomical positions between the d-CT and the PET image is essential before they can fused together [37, 38]. Currently available tools are not able to find accurate mapping between the physical spaces of the d-CT and the PET images. Finding an accurate anatomical mapping is particularly difficult as these two modalities do not have an established relationship between their intensities. The d-CT volume represents the anatomical information with enhanced vascular structures while the PET image characterizes the physiological function of the body. However, the d-CT and the AC-CT volumes belong to the same imaging modality. As there is an established relationship between the intensities, an anatomical mapping between these images can be accurately derived. This process of finding the mapping of the physical spaces between two images is known as image registration. However, establishing an anatomical mapping between the d-CT and the AC-CT is also challenging due to their image acquisition at different breathing stages and the presence of the contrast agent in the d-CT.

In this thesis, we adopt a two-step approach towards the fusion of d-CT and PET images. The first step involves registering the d-CT with the AC-CT which is facilitated by the fact that both images represent the same modality. The deformations obtained during this process are used to implement the second step, i.e., these deformations are then used to fuse the d-CT and the PET image volumes. Current registration algorithms cannot accurately

register the d-CT and AC-CT images because they do not consider the physiological and physical properties of the various organs during the registration process. In this thesis, we will concentrate on developing a new framework for the registration of the d-CT and AC-CT image volumes. The new framework is based on the physical properties of the various organs and structures present within the image.

The main contribution of this thesis is the development of a registration framework for the anatomical alignment of d-CT with AC-CT volumes of lung cancer patients. By extending the state-of-the-art approach in image registration, physical properties of various structures such as the bones and lungs are incorporated in the registration framework to provide biologically plausible image deformations. This framework incorporates physical properties such as preservation of rigidity and image topology. We also introduce a term to preserve the physiological motion of the lungs along the boundaries (generally known as the sliding motion). Finally, the deformation field obtained from the d-CT and AC-CT registration is applied to fuse the d-CT with the PET image. The fusion of d-CT with PET can potentially help in accurate diagnosis and staging of lung cancer.

1.3 Outline of the Thesis

The thesis is structured as follows:

Chapter 1 has introduced the clinical problem of lung cancer imaging and fusion, and has stated the aims and contributions of this thesis.

Chapter 2 develops a general framework for image registration. It explores the various components of image registration which consists of the transformation models, similarity measures and optimization. Finally, we provide an overview of the state-of-the-art techniques available for lung image registration followed a critical analysis of their effectiveness for d-CT and AC-CT registration.

Chapter 3 focuses on physics based transformation models, namely the elastic and fluid registration techniques. We describe the implementation details for elastic and fluid registration problem, followed by a comparison between the two methods. We also discuss

the problems that emerge due to lack of physical constraints to preserve the topology of the image and the rigidity of the bones. To address these problems, we present a new framework for image registration which includes an additional force term to preserve the topology of the image and a spatially variable filtering technique to preserve the rigidity of the bones.

Chapter 4 presents the results based on the image data provided by the lung registration challenge, "Evaluation of Methods for Pulmonary Image Registration 2010" (EMPIRE10) conducted in conjunction with the Grand Challenges in Medical Image Analysis Workshop in 2010. The deformations generated using the classic elastic method and the elastic version of the proposed new framework from Chapter 3 were applied to the challenge data and the final results are included in this thesis.

Chapter 5 motivates the need for incorporating sliding motion modeling in our new registration framework. Initially, our sliding motion model is tested on a 2D synthetic image to establish its concept. Later, the sliding motion model is incorporated in our proposed registration framework and tested on two image volume datasets, namely the POPI dataset and the EMPIRE10 dataset.

Chapter 6 investigates the application of our work for fusing d-CT with PET. First, we register the d-CT and the AC-CT using our proposed registration framework composed of topology preservation, rigidity preservation and sliding motion model. The deformations obtained from this step are used to anatomically align the d-CT and PET image so that they can be fused together.

Chapter 7 summarizes our work, points out possible extensions, and concludes with suggestions for future work.

Chapter 2

Image Registration for Lung Images

In order to map the data from different images into a single coordinate system image registration is required. In this work, we address the registration of diagnostic CT (d-CT) and attenuation correction CT (AC-CT). For this, we will first review the underlying principles of image registration. This is followed by a brief summary of the state-of-the-art image registration algorithms used for lung and chest imaging, and the challenges involved in obtaining a biologically plausible registration solution.

2.1 Introduction to Image Registration

In medical applications, the spatial alignment of structures is required to combine information from different images. Image registration is the process of determining this geometrical relationship between two images to achieve anatomical or functional correspondence. A more detailed description and a thorough classification of the components of image registration are provided in image registration reviews by Brown [39] and Maintz [40]. Image registration is important in many aspects of medical image analysis such as:

1. Motion correction/compensation: Image registration can used to correct/compensate the movement of the patient between scans taken at different time points. A common example of this application is to correct for motion between pre-operative, intra-operative and post-operative scans. These deformations are mainly physical in nature

and are caused by patient movement, physiological breathing motion, motion associated with the heart, peristalsis or other muscle groups.

2. Motion analysis: Image registration is also used to quantify physiological motion like changes in lung volume during respiration, pumping cycles of the heart, or compression of the joints. The quantified motion can be used for diagnosis or therapy.

3. Cross-modality image fusion: Different imaging modalities contain complementary information that can be used to improve disease diagnosis or assist the clinician for a therapeutic procedure. It is important to establish anatomical correspondence between the images by registration before fusing them. Image fusion combines information of same patient acquired using different imaging modalities like CT, X-ray, MRI, ultrasound and PET. point

4. Longitudinal studies: To detect and measure structural or functional changes over time. This information could be very helpful in aiding diagnosis or therapy. Examples include hormone therapy, Alzheimer's disease, drug trials, multiple sclerosis and morphological changes resulting from surgical interventions. Similarly, image registration of chest CT scans has been successfully used for monitoring nodule growth [41] and estimating progression of interstitial lung diseases like Chronic Obstructive Pulmonary Disease (COPD) [42].

5. Atlas construction: A simultaneous registration over a cohort of subjects is required for the creation of an average template. This average template is more commonly known as an atlas. The registration of the images is necessary to define all the subjects in a common coordinate system.

For the purpose of this thesis, we are interested in aligning d-CT and the AC-CT images that were acquired at different breathing stages and at different time points, we will focus on image registration techniques used for motion compensation. To correct for any image motion due to acquisition in different scanners and breathing motion, images need to be aligned both globally and locally, to recover the displacement of the various organs.

Given two images, a target image I_T and a source image I_S, the task of image registration is to find the transformation $\boldsymbol{T}$ that will relate the anatomical correspondences between the images. Three dimensional (3D) image volumes like CT or PET scans are defined by a finite set of voxels. A voxel represents the unit of graphical information that defines a point in three dimensional space, and is the 3-D equivalent of a pixel (picture element). A voxel in image I_T at point $\boldsymbol{x}$ is represented as $I_T(\boldsymbol{x})$ with $\boldsymbol{x} = (x, y, z)$. Image registration deforms the source image so that it resembles as closely as possible to the target image. A transformation describes the mapping between the spatial coordinates in the target image $I_T(\boldsymbol{x})$ and coordinates in the source image $I_S(\boldsymbol{x})$. The transformation is described by the displacement field $\boldsymbol{u}$ such that $\boldsymbol{T} = T(\boldsymbol{x} + \boldsymbol{u})$, where T is known as the transform function that provides the resulting displacement vectors of every voxel. If $I_S(\boldsymbol{x})$ is the source image which denotes the intensity value at each point $\boldsymbol{x}$ in the source image, then $I_S(\boldsymbol{T(x + u)})$ denotes the corresponding intensity value in the transformed source image. The process of deforming the source image with the transformation is called image warping. Image registration algorithms in general consist of three elements:

1. A transformation model: A class of admissible geometrical transformations $\boldsymbol{T}$ that can be applied to the images, i.e., employed to spatially warp the image.

2. A cost function: A quantity that measures the similarity between the images, as well as the quality of the transformation estimate

3. An optimizer: An iterative optimization method which determines the best transformation parameters with respect to the cost function.

Figure 2.1 illustrates the block diagram for a generic registration algorithm operating on these three components. The source and the target images act as the input while the output of a generic registration algorithm is the final transformation achieved after convergence of the optimization. After each iteration, the source image is warped using the current transformation estimate to yield the deformed image, while the cost function is re-calculated at each iteration.

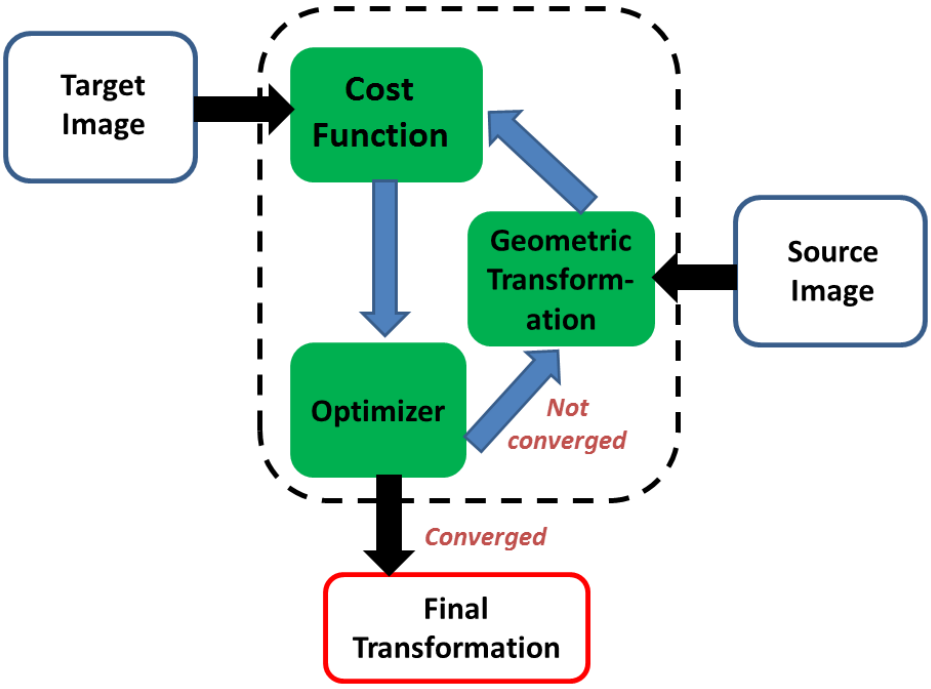

Figure 2.1: A generic image registration algorithm with three basic components namely, (1) Geometric transformation models (2) Cost Function and (3) Optimizer

2.1.1 Rigid and Affine Registration

The transformation model determines the type of spatial mapping function that is to be applied to the image. Transformation models are generally classified into two types: global and local. Global transformations compensate for the global repositioning of the patient. They preserve the parallelism between the grid lines in the image. Global transformations are classified into two main types: rigid and affine. Rigid transformations form a sub-class of affine transformations. A rigid transformation for 3D images is described by the translation vector $\boldsymbol{t} = [\ t_x \quad t_y \quad t_z]$ (three degrees of freedom for each of the x, y and z orthogonal directions) and the rotations α, β and γ about the axes (three degrees of freedom). The rigid transformation $\boldsymbol{T}_{\text{rigid}}$ is represented as:

$$\boldsymbol{T}_{\text{rigid}} = \boldsymbol{R}\boldsymbol{x} + \boldsymbol{t}, \tag{2.1}$$

where $\boldsymbol{R}$ represents a 3×3 orthogonal rotation matrix. The rigid transformation is often extended to affine transformations, which include scaling (three degrees of freedom) and shears (three degrees of freedom). Hence affine transformations have a total of 12 degrees of freedom in equation 2.2. The coupling of scaling with the rigid registration is effective when registrations must account for erroneous or unknown scales in the image acquisition process. Affine transformations map parallel lines into parallel lines but do not preserve the lengths and the angles of the lines. The affine transformation can partially correct for calibration differences across scanners or gross differences in scale between subjects. The affine transformation is represented by the following equation:

$$\boldsymbol{T}_{\text{affine}}(\boldsymbol{x}) = \begin{bmatrix} a_{00} & a_{01} & a_{02} & t_x \\ a_{10} & a_{11} & a_{12} & t_y \\ a_{20} & a_{21} & a_{22} & t_z \\ 0 & 0 & 0 & 1 \end{bmatrix} \begin{bmatrix} x \\ y \\ z \\ 1 \end{bmatrix}, \tag{2.2}$$

where a_{ij} is the coefficient of the affine components and $[x\ y\ z]$ represents the voxel position. Rigid and affine transformations are expressed in matrix notation to represent the elemental transformations of rotation, translation, scaling and shearing. An example of rigid and affine transformations is presented in Figure 2.2. Rigid or affine registration is often used as the first step in pulmonary image registration to correct for the distortions created by the imaging device.

2.1.2 Non-Rigid Registration

Global (rigid or affine) transformations can not handle images that are deformed locally. The problem of local deformations can be solved by the use of local registration, which is appropriate for compensation of local tissue motion and longitudinal tissue changes. Local transformations allow regions to deform more independently. Local transformations do not preserve the parallelism or the straightness of lines in the image and could map the straight lines into curved lines. Non-rigid transformation models can be classified into parametric

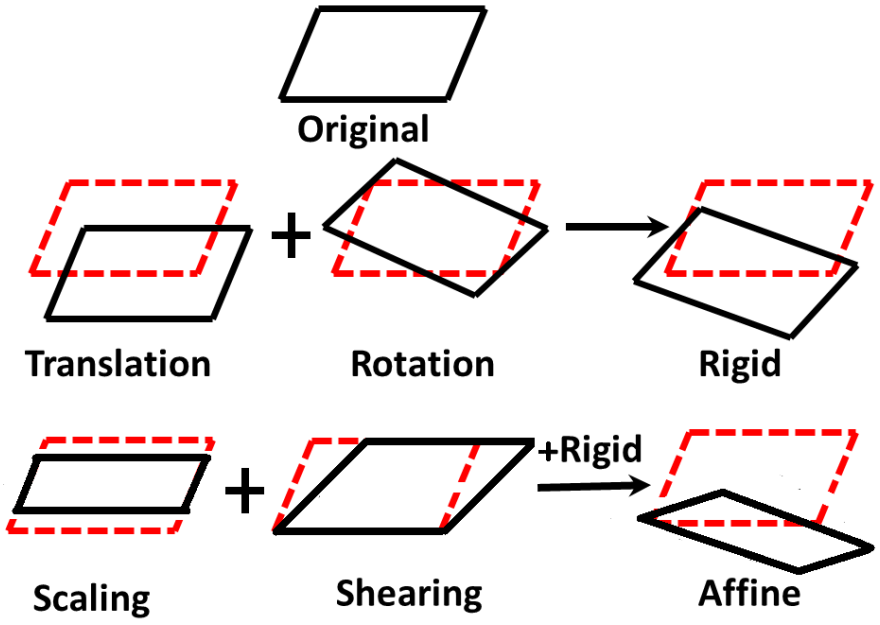

Figure 2.2: Rigid and Affine transformation

and non-parametric registration.[1]

2.1.2.1 Parametric Transformation Models

For parametric models, the registration process is designed to find a compact set of optimal parameters that can transform the source image to the target image. For this, the deformations are not calculated for every voxel, but instead they are defined for a set of sparse grid points. The dense deformations for all image voxels are interpolated from the deformations defined at the grid points. Among parametric techniques, spline based methods are most commonly used. The term spline is derived from the ship building industry where it refers to a plank of wood which is bent by applying varying amount of weights along its length to obtain smooth shapes. In mathematics, a spline is a special function that is defined piecewise by polynomials and is used in applications requiring data interpolation and smoothing. Splines have a very simple form locally, but at the same time they are globally flexible, thus making them useful to model arbitrary functions. Two of the most widely used spline based

[1]Despite affine transformations being technically non-rigid, we will in the following use the term non-rigid transformations to refer to local transformation models.

registration techniques are thin-plate splines (TPS) [43] and cubic B-splines for Free Form Deformations (FFDs) [44]. In the following, both spline models will be briefly reviewed.

a. Thin-plate splines (TPS): refers to a physical analogy involving the bending of a thin sheet of metal. TPS registration is a landmark based registration technique which is usually used with a set of homologous features and anatomical landmarks that are manually or automatically selected in the image. TPS was introduced to the computer vision community by Grimson et al. [45] as a form of method to interpolate surfaces from visual information. Bookstein [43] established the modeling of shape deformation using TPS. TPS registration interpolates the displacement necessary to map the location of the landmark point in the target image to its corresponding counterpart in the source image. The advantages of TPS over other landmark based methods include better registration results and ease of incorporation of additional constraints such as directional constraints [46].

b. FFDs using B-splines: B-splines are mathematical functions that have a compact support region with respect to the degree of the polynomial function, smoothness and domain partition. In computer vision, B-splines generally refer to a spline curve expressed as linear combination of the B-spline mathematical function. Since B-splines are locally controlled, they are computationally efficient even for large number of control points. Rueckert et. al [44] proposed the use of cubic B-splines in combination with FFDs and normalized mutual information (NMI) as a similarity measure for image registration. The degrees of freedom of the transformation will depend on the resolution of a mesh of regularly distributed control points. B-spline registration has shown superior performance for the registration of dynamic contrast enhanced MR breast images. A study by Klein et al. [47] has also demonstrated B-spline registration to be among the top three registration techniques for human brain MRI registration.

Other options for parametric methods exist beyond the models presented above. Rohr et al. [48] and Fornefett et al. [49] have performed detailed investigation in the use of radial basis functions and their variants for registration. Amit et al. [50] proposed to model the deformation as a wavelet expansion in 2D while considering registration as a variational

problem. An overview and implementation details for the various parametric methods could be found in the image registration review by Holden et al. [51].

Most of the parametric methods mentioned (with the exception of FFDs using B-splines) are landmark based registration techniques. These methods pose a problem because the registration depends only on the landmarks. The original image is not taken into consideration during the registration process. The global influence of these landmark leads to incorrect results as it diminishes the effect of the local deformations. The other disadvantage with landmark based image registration is that determining the right amount and correct placement of landmarks at sensible locations is difficult and time consuming. Automatic extraction of landmarks can be acheived by using landmarks selected along segmented airways, vessels and fissures [52]. However, the automatically selected landmarks points need to manually verified and corrected in many cases before they are used for registering the images [53]. For accurate chest CT registration, we also require a large number of landmarks with an equal amount of spread across the entire image. Due to partial volume effects, limited scanner resolution, and errors during skeletonization, only about 20 to 30 branching points per lung can be reliably matched using this approach. Hence landmark based methods on their own are avoided for registering the chest CT but they can be used in combination with intensity based registration methods.

2.1.2.2 Non-Parametric Transformation Models

In non-parametric image registration, the focus is not on specific grid points or markers, but to find a dense deformation field with a displacement vector for each voxel. The deformations for non-parametric methods are assumed to fulfill a certain physics based model. These physics based models can be based on material properties such as elasticity, fluid dynamics or optical flow, and are generally defined by an associated system of partial differential equations. One of the first non-parametric methods based on elastic model of deformations was proposed by Broit [54] and further developed by Bajcsy et al. [55]. The model based on fluid dynamics was proposed by Christensen et al. [56] , while optical flow based registration was introduced

by Horn and Schunck [57]. Other forms of non-parametric transformations include models based on image diffusion [58] and curvature [59] which attempt to evaluate the smoothness of the deformation itself. A detailed overview of the various non-parametric registration techniques could be found in Zitova et al. [60] and Maintz et al. [40].

2.1.3 Cost Function

The cost function defines a quantity to measure the similarity between the images and the quality of the deformations. The choice of the cost function is crucial to the success of the registration process.

2.1.3.1 Similarity Measure

In order to establish a relationship between the intensities of the target and the source images, one must define a similarity criterion to measure the degree of alignment between the images. This similarity criterion can be based on voxel information such as image intensity. To achieve this objective, there are many different types of similarity measures. Their performance and application depends on various factors such as modality of the images, presence of contrast agents, the type and degree of noise present in the images, intensity inhomogeneities, geometrical distortions, partial image overlap, etc. Some of the widely used similarity measures are described in the following sections.

Sum of Squared Differences

Sum of squared differences (SSD) is the simplest type of similarity measure available and is based on the assumption of an identity relationship between the source and target image intensities. This assumption is valid for intra-subject images that have been acquired from the same sensor under the same conditions. SSD makes the implicit assumption that after registration the images only differ by noise. SSD can be defined by the equation below:

$$SSD = \sum_{i} (I_A(\boldsymbol{x_i}) - I_B(\boldsymbol{x_i}))^2 \tag{2.3}$$

where N is the number of voxels, and I_A and I_B represent the two images. SSD has a poor performance in the presence of high image noise [61] as compared to other measures. In our application, SSD is unsuitable for registration of d-CT and AC-CT images as the d-CT acquisition is done with a contrast agent present, whereas the AC-CT is acquired without a contrast agent.

Mutual Information

Mutual information (MI) was proposed as a similarity measure for rigid and affine image registration independently by Collignon et al. [62] and Wells et al. [63]. MI measures the statistical dependence between two random variables or the amount of information that one variable contains about the other. The mutual information $MI(I_A, I_B)$ between two images I_A and I_B can be defined in terms of the marginal entropies $H(I_A)$ and $H(I_B)$ of the image intensities, combined with their joint entropy $H(I_A, I_B)$, as follows :

$$MI(I_A, I_B) = H(I_A) + H(I_B) - H(I_A, I_B) \tag{2.4}$$

The marginal entropy is the measure of the uncertainty associated with a random variable while the joint entropy $H(I_A, I_B)$ is the measure of the uncertainty associated with I_A and I_B as shown in equation 2.6:

$$H(I_A) = -\sum_a p(a) log(a) \tag{2.5}$$

and

$$H(I_A, I_B) = -\sum_a \sum_b p(a, b) log(a, b) \tag{2.6}$$

where $p(a, b) = h(a, b)/N$, $p(a) = \sum p(a, b)$ and $h(a, b)$ is the count value of the 2D joint histogram. However, mutual information is not independent of the overlap of two images, and may fail as a similarity measure in cases of indefinite overlap. Mutual information also shows problems when the size of the images becomes smaller making the overlap statistics less reliable.

In registration problems where the image misalignment can be large with respect to the imaged field, it is important to have information theoretic measures independent of the overlap statistics. Studholme et al. [64] solved this problem by the introduction of Normalized Mutual Information (NMI) as a measure of image alignment. NMI represents a normalized entropy measure which is the ratio of the sum of the marginal entropies and the joint entropy. NMI provides a fully robust and automated similarity measure and has been used in a number of multi-modality imaging studies [65, 66, 67] and is described by equation:

$$NMI(I_A, I_B) = \frac{H(I_A) + H(I_B)}{H(I_A, I_B)} \tag{2.7}$$

Cross Correlation

Cross correlation (CC) between two signals is a standard approach in signal analysis. Cross correlation can be calculated in both space and frequency domains and is a common similarity measure in image registration problems. Cross correlation depends on local image intensity average and variance, using only few samples. CC is defined as follows:

$$CC(I_A, I_B) = \frac{\sum_i I_A(x_i) I_B(x_i)}{(\sum_i (I_A(x_i))^2)^{1/2} (\sum_i (I_B(x_i))^2)^{1/2}} \tag{2.8}$$

The value of the similarity measure lies in the interval [-1, 1]. The cross correlation value is 1 if the images are completely identical , the value is 0 if the images are completely uncorrelated and the value is -1 if one image is negative of the other. Cross correlation has shown improved results and robustness compared to SSD in cases of unpredictable illumination, reflectance or bias fields. It has a superior performance for images with low noise, however it has a poorer performance for extremely noisy images such as ultrasound images.

Normalized cross correlation (NCC) is a variant of cross correlation where the images are normalized by subtracting the mean of the pixel value in each image. NCC is invariant to the contrast or intensity ramping of the images.

$$NCC(I_A, I_B) = \frac{< \bar{I_A}, \bar{I_B} >}{< \bar{I_A} >< \bar{I_B} >} \tag{2.9}$$

where $\bar{A} = I_A - \mu_A$ and the inner product is taken over a local neighborhood. μ is the local mean which is also calculated over a local neighborhood at each position $\boldsymbol{x}$. Correlation coefficient is used for registering multi-modal images. One disadvantage of the cross correlation methods is that they can incorrectly match smooth regions without prominent details.

In Table 2.1, a qualitative comparison of the five main similarity measures across four different categories is presented. NCC establishes itself as the most suitable similarity measure for our application with a simple implementation, low computational time, good robustness and local measure capabilities [68]. NCC also has partial multi-modal capabilities [69, 70] and thus can be used to register contrast enhanced CT images with non-contrast enhanced CT. MI and NMI are reliable global similarity measures for intensity-based matching of multi-modal images but have a higher computational complexity, and limited capabilities as local similarity measures [68].

Name	Computational Complexity	Multi-modal capabilities	Robustness	Local measure
SSD	+	−	−	+
MI	−	+	−	±
NMI	−	+	±	±
CC	+	+	±	+
NCC	+	±	+	+

Table 2.1: In this table five similarity measures are qualitatively compared. We indicate whether the approaches satisfy some properties ('+') or not ('−') or whether a certain property is partially fulfilled ('±'). The four categories are (i) The algorithm is easy to implement and has low computational time (ii) Multi-modal capabilities of the similarity measure (iii) Robustness of the measure for cases of unpredictable illumination, reflectance, bias fields etc. (iv) Local measure capabilities.

2.1.3.2 Transformational / Regularization Cost

In medical imaging, the end-goal is not only to register the images to achieve maximum similarity but also to obtain plausible deformations. The quality of the deformations can be controlled by using additional force terms introduced into the cost function term. These additional force terms are discussed in greater detail in Chapter 3.

2.1.4 Optimization Techniques

Optimization techniques search for the optimal transformation that maximizes the similarity between the images. It generally takes a series of guesses from an initial starting position which is gradually refined by trial and error. At each step, the cost function which relates how well the two images are registered, is computed and evaluated. In high resolution images there is a large amount of data which makes processing the data during registration a time-consuming process. Hence, a choice of search strategy plays an important role in registration algorithms. Some of the conditions required for an optimization technique in image registration algorithms are:

- It must be a non-linear multidimensional optimization technique. This is an essential requirement to handle multidimensional images and also take into account the non-linearity of the cost function.
- The optimization technique must have the ability to avoid local optima of the cost function.
- The optimization technique should minimize the number of evaluations required to reach the global optimum. This is because the calculation of the cost function generally comes at a high-computational cost.
- The optimum local value of a similarity measure can be found within a portion of parameter space termed as the capture range. Capture range of the optimum is an important property to consider while selecting the optimization technique. Optimization started outside the capture range of the desired optimum has a very low probability of reaching the correct transformation.

The optimization technique used determines the speed and success of the registration algorithm. Most registration algorithms can employ standard optimization techniques to find a good transformation such as steepest gradient descent, conjugate gradient method, Powell's method, Gauss-Newton method, etc. Along with these mentioned techniques, multiresolution optimization is generally used to prevent the algorithm from falling into local optima.

The multiresolution step is used to first solve the problem at a coarser resolution and then use this solution as a initialization for the higher resolution of the images.

In this section, we have reviewed some of the commonly used transformation models, similarity measures and optimization techniques used in image registration.

2.2 State-of-the-Art Registration Methods for Lung or Chest Images

The success of respiratory medicine is dependent on a thorough description and understanding of the human lung and its response to disease, injury and treatment. Many researchers in medical imaging have focused on post-processing algorithms to provide fast, automated, objective, quantifiable measures characterizing lung pathology. Chest CT image registration has been established as an important post-processing step used by clinicians and radiologists to map multiple lung volumes together, for purposes of evaluating regional lung mechanics [71] and tracking pathology over time [52]. Image registration is also commonly used during radiotherapy sessions to reduce the risk of irradiating vital organs due to patient motion and reduced tumour coverage. Many surgical procedures also employ image registration techniques to assist the clinician in accurate surgical planning of tumour resection [72, 73].

Chest image registration is more complex than registration of other parts of the body like the brain, in particular because of the unique non-rigid motion of lung and the thoracic structures. To further elaborate on the complexity of the problem, we take the example of the most commonly encountered problem of breathing motion artifacts. During breathing the lungs change in position, volume and shape, while the ribs and the spine deform rigidly, i.e., they do not change in shape or volume. In contrast to that, during breathing the liver also changes in shape but its volume remains the same. Registering a combination of such diverse movements of organs is further complicated by the lack of accurate anatomical landmarks.

Many efforts have been made in the field of chest CT image registration but the lack of a gold standard has prevented an accurate validation of the registration accuracy. The

MICCAI 2010 Grand Challenge on Evaluation of Methods for Pulmonary Image Registration 2010 (EMPIRE10) has been an important step in establishing an automated assessment of registration accuracy for the vast array of algorithms available in research [74]. The competing algorithms in the EMPIRE study included a wide variety of registration methods with different combinations of transformation models, optimization techniques and similarity measures. Some of the algorithms were designed for lung CT applications while others arose from completely generic registration applications. A detailed study of the participating algorithms provides a good understanding of the current areas of development and research interest for CT image registration. The challenge participants were evaluated on the basis of four criteria:

a. Lung Boundary alignment

b. Fissure alignment

c. Landmark registration error

d. Singularities of the deformation field, i.e., topology preservation

The Advanced Normalization Tools (ANTS) algorithm based on the symmetric image normalization method showed to have the best performance for the EMPIRE challenge data [75, 76]. The algorithm uses normalized cross correlation (NCC) as the similarity measure in a local neighborhood around each voxel. The use of NCC compensates for the inhomogeneity of the density changes over the lung volume in the image pair. The ANTS algorithm models diffeomorphic transformations to ensure one to one topological properties. Diffeomorphic transformations ensure the invertibility of the transformations and the preservation of the deformation field topology. Many other algorithms participating in the challenge incorporated some form of topology preservation that highlights its increased attention. A large number of algorithms within the challenge were based on B-spline parametric registration techniques. The variation between the various algorithms was mainly based on the use of varying similarity measures and in some cases the introduction of additional constraints. One of the participants extended the B-Spline method by including a robust 3D registration of the vessel trees [77]. The B-spline methods performed well for cases with considerable difference

in lung volumes but they underperformed in some cases due to the smoothing effect caused by the linear interpolation and the B-spline transformation.

The fast elastic image registration algorithm proposed by Kabus et al. [78] was also introduced in the challenge. The algorithm was based on simultaneous minimization of the SSD similarity measure and the Navier-Lamé operator. The algorithm was ranked 10th out of the 34 participating algorithms. The weakest point of the algorithm's performance was the presence of folding in the deformation field that lowered its overall rank . The algorithm did not contain any additional constraint for preserving the topology. One of the other non-parametric methods participating in the challenge was the algorithm by Heinrich et al. [79] who introduced a variant of the optical flow model to achieve discontinuity preservation. The proposed algorithm used a variational formulation of the optical flow model with non-quadratic regularization. The algorithm performed very well for aligning the fissures and the landmarks but was unsuccessful in complete preservation of the topology.

The validation process of the algorithms used in the EMPIRE challenge was very thorough, uniform and the first of its kind for lung image registration. However, one of the primary disadvantages of the challenge was that the evaluation criteria were based only on the lung volume and the effect of the registration on the other external structures was effectively ignored. The rigidity of the bones, the preservation of the topology outside the lungs and the quality of the deformation are some of the additional validation steps that could have provided a further improved evaluation of the chest image registration. Thus in the EMPIRE challenge, the different registration algorithms stressed on higher lung overlaps and topology preservation. None of the algorithms proposed a solution to solve the three major problems encountered in chest image registration which are rigidity preservation, discontinuity preservation/ sliding motion and topology preservation for the entire image domain in one single framework. The lack of such physical properties in the registration framework would not be able to provide a physically plausible deformation. A comparison of the various registration algorithms participating in the EMPIRE challenge is provided in Table 2.2 with regards to the three physical properties discussed.

There is a growing amount of research that tries to address these problems individually, and that introduces physiologically based models into image registration. We have divided this literature into three categories based on the problems that they address, namely:

- Topology preservation of the deformation field
- Rigidity preservation for the bones and other rigid structures
- Sliding motion of the lungs

Registration Technique	**Topology preservation**	**Rigidity preservation**	**Sliding motion**
ANTS [76, 75]	+	−	−
Feature point extraction and matching [80]	+	−	−
Fast elastic image registration [78]	−	−	−
Regularized registration by preserving tissue volume and vesselness measure [81]	+	−	−
Statistical modeling of diffeomorphic registration [82]	+	−	−
Optical flow with robust measures [83]	−	−	−
Registration with sub-anatomical segmentations [84]	−	−	+
Discontinuity preserving regularization for variational optical flow [79]	−	−	+
Non-rigid registration with adaptive, content-based filtering of the deformation field [85]	−	+	−

Table 2.2: Review of various algorithms used for CT lung image registration. We indicate whether the algorithms satisfy some properties ('+') or not ('−'). The three properties highlighted are: a) Topology preservation (whether the registration algorithm is able to preserve the topology of the deformation field for the entire image domain or not). b) Rigidity preservation (whether the algorithm is able to preserve the rigidity of the bones or not). c) Sliding motion (whether the algorithm is able to preserve the discontinuous movement at the lung boundaries or not).

None of the currently available techniques in literature are able to simultaneously address all these problems. Thus the aim of the thesis is to provide a comprehensive registration framework that incorporates all the three properties in one solution. To obtain this solution , we start with a very basic transformation model and then add constraints and models to the

framework to achieve topology preservation, rigidity preservation and the sliding motion. For this purpose, we choose the physics based transformation models as our initial model. Our rationale for using physics based models for registering the CT lung images is the following:

- Physics based transformation models like the elastic and fluid models are the closest representations of the physical properties of the organs in the CT image. Other transformation models use mathematical based functions and do not consider the physical properties of the organs involved.

- Additional constraints can be easily added and removed from the registration process by configuring the external forces applied.

- Elastic and fluid registration are already widely used and have shown good results for medical image registration problems [78].

- Physical transformation models can accommodate for large variations in physical behavior of the objects and also the kind of movement for each organ.

In the next chapter, we investigate the properties of elastic and fluid transformation models and generate a framework to provide biologically plausible deformations.

Chapter 3

Physics Based Models for Image Registration

The chapter first provides a general introduction to elastic and fluid transformation models upon which the work in this thesis is based. This is followed by an introduction to topology preservation and the use of log-unbiased deformations for preserving the topology. After that the need for adding a rigidity constraint for bones will be motivated and discussed, and a solution will be presented that applies a spatially varying filter to obtain linear deformations in bony regions within the registration framework. The chapter concludes with a discussion of the results obtained on phantom data when incorporating the log-unbiased deformations and the spatially varying rigidity filter into the elastic and fluid registration framework.

3.1 Physics Based Models

Physics based models used in image registration are based on the theory of linear elasticity. Linear elasticity focuses on balancing the external forces applied to deform the object and the internal stress generated based on the physical properties of the body. These physical models have been broadly divided into two categories: elastic and fluid transformations. Elastic and fluid transformation models make use of continuum mechanics in the registration process and are described in greater detail in the following subsections.

3.1.1 Elastic Registration

Elastic image registration refers to the use of a physical model over a continuous medium with elastic properties to impose smoothness constraints on the image mapping. The image is treated as an elastic body subject to external forces which drive the deformation [55]. Under the impact of the external forces, the image gets deformed. The internal forces (also called stresses) impose a smoothness constraint that controls the deformation of the image driven by the external forces. The elastic body will undergo deformation until an equilibrium state is established between the external and internal forces. The behavior of the model in terms of the displacement vector field $\boldsymbol{u} = (u_x, u_y, u_z)$ is described by the Navier-Lamé linear partial differential equation (PDE) given as:

$$\begin{aligned} \mu\nabla^2 u_x + (\lambda+\mu)\tfrac{\partial(\nabla.\boldsymbol{u})}{\partial x} + F_x = 0 \\ \mu\nabla^2 u_y + (\lambda+\mu)\tfrac{\partial(\nabla.\boldsymbol{u})}{\partial y} + F_y = 0 \ , \\ \mu\nabla^2 u_z + (\lambda+\mu)\tfrac{\partial(\nabla.\boldsymbol{u})}{\partial z} + F_z = 0 \end{aligned} \tag{3.1}$$

where $\boldsymbol{F} = \{F_x, F_y, F_z\}$ represents the external force component that drives the registration. The parameters λ and μ are the Lamé elasticity constants describing the properties of the material. The shear modulus $'\mu'$ describes the response of the material to shearing strains. The second Lamé parameter $'\lambda'$ defines the material's resistance to uniform compression and controls the rate of growth or shrinkage of local regions within the deforming source image. The incremental deformation is calculated for each iteration and then added to get the final transformation. The Laplacian term $\nabla^2\boldsymbol{u}$ constraints the deformation field to vary smoothly while the divergence term maintains the coupling of the x, y and z components due to its mixed derivative terms. These equations are derived from conservation of mass, momentum, and energy; they are experimentally measured material properties. A detailed derivation of the equations is provided in the Appendix A. A vector notation of equation 3.1 is given as:

$$\mu\nabla^2\boldsymbol{u} + (\lambda+\mu)\nabla(\nabla.\boldsymbol{u}) + \boldsymbol{F} = 0. \tag{3.2}$$

The extent of deformation within the elastic body will depend on the selection of Lamé elastic parameters. For large values of Lamé parameters (in relation to the external forces), the body appears to be more rigid. For small Lamé values, the amount of deformation is dictated by the external forces [55]. This can lead to the generation of unrealistic deformations as the smoothness constraint is weak especially if the signal-to-noise ratio is low [56]. In literature for most cases λ is set to zero and μ is used to balance the internal and external forces [55, 58]. The physical significance of Lamé's constant can be expressed in terms of Young's modulus E and Poisson ratio σ:

$$E = \mu \frac{3\lambda + 2\mu}{\lambda + \mu}, \tag{3.3}$$

$$\sigma = \frac{\lambda}{2(\lambda + \mu)}, \tag{3.4}$$

where σ is the ratio between lateral shrink and the longitudinal stretch. E relates tension of the image and its stretch in the same direction. Broit [54] introduced the idea of elasticity modeling in image registration by solving the equation 3.2 using a finite difference technique. Bajcsy et al. [55] further expanded on the method by numerically solving the PDE for a discrete deformation field using a three step multiresolution approach to recover large deformations. The external forces designed by Bajcsy et al. [55] used normalized cross correlation of image features as a similarity measure. Some of the image features included the local mean intensity and the horizontal or vertical edges extracted from the image [55]. Since then, different variants of elastic image registration have been introduced for various applications. One of the widely used applications of the elastic method has been for inter-subject brain image registration. Davatzikos and Bryan [86] designed an elastic algorithm for the registration of the cortical gray matter. Gee et al. [87] modified the previous approach of Bajcsy et al. for brain registration, by solving the elastic PDE for a basis function expansion of the deformation field. The classic elastic registration algorithm has also been used for lung image registration by Kabus et al. [78].

3.1.2 Fluid Registration

Although elastic registration provides a close representation of the material properties of the tissues and organs in an image [88], it can not handle very large deformations. The Navier-Lamé PDE equations are based on the assumption of an infinitesimally small deformation and the internal forces increase monotonically with the deformed distance. Both these conditions limit the amount of deformation that can be achieved through elastic registration. To cope with these shortcomings, Christensen et al. [56] developed a registration technique based on a viscous fluid model. Here, the image is modeled as a viscous fluid flowing under the effect of the external forces to match the source and target images. In the fluid model, the internal restoring forces disappear over time, and consequently large deformations can be achieved. The fluid model has to fulfill physical laws such as the conservation of mass, energy and linear angular momentum. The PDE of the viscous fluid model is defined by the Navier-Stokes equations as follows:

$$\mu\nabla^2\boldsymbol{v} + (\lambda+\mu)\nabla(\nabla.\boldsymbol{v}) + \boldsymbol{F} = 0, \tag{3.5}$$

where $\boldsymbol{F} = (F_x, F_y, F_z)$ is the external force and $\boldsymbol{v} = (v_x, v_y, v_z)$ is the velocity field. Equation 3.5 is similar to the PDE for elastic registration with the only difference that for the elastic registration the smoothing was applied on the displacement field whereas in fluid registration the PDE is working on the velocity field. Another modification attributed to fluid registration is the use of a Eulerian reference framework instead of the Lagrangian reference framework. The Eulerian framework helps in achieving larger deformations.The reference frameworks are explained in greater detail in Section 3.1.3. The relationship between displacement and the velocity is established using equation 3.6:

$$\boldsymbol{R}^k = \frac{\partial \boldsymbol{u}}{\partial t} = \boldsymbol{v} - \sum_{i=1}^{3} v_i \frac{\partial \boldsymbol{u}}{\partial x_i}, \tag{3.6}$$

where $\boldsymbol{R}^k$ is the perturbation of the deformation field, x_i and v_i refer to the ith component of the location vector $\boldsymbol{x}$ and the velocity vector $\boldsymbol{v}$, respectively. Using the above equation and

decomposing the non-linear PDE into a set of linear equations on the velocity field for each period of time, the displacement field at iteration $k+1$ can be obtained using the following update equation:

$$\boldsymbol{u}^{k+1} = \boldsymbol{u}^k + \boldsymbol{R}^k \Delta t. \tag{3.7}$$

The time step Δt is controlled by $\Delta t \leq \max(||\boldsymbol{R}^k||)\Delta \boldsymbol{u}$ with $\Delta \boldsymbol{u}$ being the maximum displacement admissible in one iteration, usually set to be half the voxel size. The total deformation field is obtained by addition of the incremental deformation fields. A faster version of the fluid registration was proposed by Bro Nielsen et al. [89] that used a convolution filter in a scale-space framework as a replacement for finding the solution of the linear equations for the velocity field of the fluid. However, using the convolution filter leads to poorer results in comparison to the solution of the linear equations [58, 90].

Both registration models, elastic and fluid, require finding the solution for a large system of equations that is computationally expensive and time consuming, especially for large 3D images. In this work, we employ the technique used by Fischer et al. [91] that uses fast inversion of matrices to solve a large linear system of equations. The system of equations produced by the linear elastic operator forms a circulant matrix. A circulant matrix is a $n \times n$ matrix where each row has the same elements as the previous row but shifted one column to the right [92]. This circulant matrix arrangement helps in diagonalizing the linear elastic matrix using a discrete Fourier transform. The linear elastic operator is explicitly inverted by using a Fast Fourier Transform (FFT) followed by calculation of the Moore-Penrose pseudo-inverse to prevent it from becoming singular. Similarly, the external force terms are transformed into the Fourier domain using an FFT, and then multiplied by the inverted linear elastic operator. The result of this step is then transformed back to the time domain to obtain the smoothed velocity field, allowing the computation of the displacements using equations 3.6 and 3.7.

3.1.3 Reference Frame

The reference frame defines the time evolution of the mapping of the deformation field with respect to the co-ordinate system. The movement of a voxel during the registration process can be tracked based on its initial or final position. The reference frame is considered Lagrangian if the voxel is tracked with respect to its initial co-ordinates. In the Lagrangian co-ordinate system the displacements of the individual voxels are tracked over time. This may cause the voxel to move to locations that do not correspond to voxel locations on the fixed grid. The Lagrangian framework introduces an additional step in the registration process of projecting the deformations onto a voxel lattice for calculating the cost function for the next iteration. The Lagrangian frame is also more natural for landmark registration as shown by Joshi and Miller [93] and Twining et al. [94] . Alternatively, the reference frame is called Eulerian if a voxel is tracked with respect to its final co-ordinates, i.e., the deformation is tracked with respect to a fixed voxel lattice. The Eulerian reference frame was first used for fluid registration by Christensen et al. [56] as it is more natural for tracking large distance, non-linear deformations. The Eulerian frame of reference is a better strategy for fluid registration as it eliminates the need to trace the path of the movement of the particle. Throughout our work, we use the Eulerian reference frame during the registration process.

3.1.4 External Driving Forces

External forces determine the amplitude and the direction of the force that should be applied to obtain the deformation field. The external force is obtained from the cost function as explained in Chapter 2. One of the tasks of the external forces is to bring similar regions in correspondence and reduce the dissimilarity between the images. They are responsible for guiding the solution locally as well as globally, based on the similarity measure. However, external forces can also be used for introducing additional constraints in the transformation model such as maintaining the topology of the image or to introduce new biological constraints. The external force using sum of squared differences (SSD) of the image intensities

as a cost function can be defined as follows:

$$C(\boldsymbol{u}) = \frac{1}{2}\int_{\Omega}(I_S(\boldsymbol{x}-\boldsymbol{u}) - I_T(\boldsymbol{x}))^2 d\boldsymbol{x}, \tag{3.8}$$

where Ω represents the image space for the source and target images I_S and I_T respectively. This similarity measure is the function is to be minimized and should approach zero when the images are correctly aligned.The formation of such a force component with these properties can be achieved by defining the force as a derivative of the cost function with respect to the displacement vector $\boldsymbol{u}$. The derivative of a functional $\boldsymbol{F}$ with respect to a vector is given as:

$$\lim_{\epsilon\to 0}\frac{C(\boldsymbol{u}+\epsilon\boldsymbol{w}) - C(\boldsymbol{u})}{\epsilon} = \int_{\Omega}\boldsymbol{F}(\boldsymbol{x},\boldsymbol{u})\cdot\boldsymbol{w}d\boldsymbol{x}, \tag{3.9}$$

where $\boldsymbol{w}$ is an arbitrary vector of the same dimension as $\boldsymbol{u}$. Replacing equation 3.8 in 3.9, we get:

$$\lim_{\epsilon\to 0}\frac{C(\boldsymbol{u}+\epsilon\boldsymbol{w}) - C(\boldsymbol{u})}{\epsilon} = \lim_{\epsilon\to 0}\frac{1}{2\epsilon}\int_{\Omega}|I_S(\boldsymbol{x}-(\boldsymbol{u}+\epsilon\boldsymbol{w})) - I_T(\boldsymbol{x})|^2 - |I_S(\boldsymbol{x}-\boldsymbol{u}) - I_T(\boldsymbol{x})|^2, \tag{3.10}$$

$$\lim_{\epsilon\to 0}\frac{C(\boldsymbol{u}+\epsilon\boldsymbol{w}) - C(\boldsymbol{u})}{\epsilon} = \frac{1}{2}\int_{\Omega}\lim_{\epsilon\to 0}\frac{A(\boldsymbol{x},\boldsymbol{u}+\epsilon\boldsymbol{w}) - A(\boldsymbol{x},\boldsymbol{u})}{\epsilon}d\boldsymbol{x}, \tag{3.11}$$

where A is the square of the differences between the images : $A(\boldsymbol{x},\boldsymbol{u}) = |I_S(\boldsymbol{x}-\boldsymbol{u}) - I_T(\boldsymbol{x})|^2$, and the derivative of A with respect to the vector $\boldsymbol{u}$ is equal to:

$$2(I_S(\boldsymbol{x}-\boldsymbol{u}) - I_T(\boldsymbol{x}))I_S'(\boldsymbol{x}-\boldsymbol{u};\boldsymbol{w}) = 2(I_S(\boldsymbol{x}-\boldsymbol{u}) - I_T(\boldsymbol{x}))\nabla I_S|_{\boldsymbol{x}-\boldsymbol{u}}\bullet\boldsymbol{w}, \tag{3.12}$$

where $I_S'(\boldsymbol{x}-\boldsymbol{u};\boldsymbol{w})$ is the derivative of the $I_S(\boldsymbol{x}-\boldsymbol{u})$ in the direction of $\boldsymbol{w}$. Taking the above equations in consideration, the external force component $\boldsymbol{F(x,u)}$ for the SSD is given as:

$$\boldsymbol{F}(\boldsymbol{x},\boldsymbol{u}) = -((I_S(\boldsymbol{x}-\boldsymbol{u}) - I_T(\boldsymbol{x}))\nabla I_S|_{\boldsymbol{x}-\boldsymbol{u}}). \tag{3.13}$$

One of the problems with the above measure is that if two similar regions are supposed to be matched, there is no guarantee that the force will act in the right direction if there is no overlap between the two regions. Therefore for real images a rigid or an affine registration is necessary before starting the local registration process. The algorithm for the classic elastic registration method can then be formulated as:

Algorithm 3.1 Classic elastic registration

Initialize the iteration $k = 0$ and $\boldsymbol{u}^{\boldsymbol{0}}(\boldsymbol{x}) = 0$.

1. Given $\boldsymbol{u}^{\boldsymbol{k}}(\boldsymbol{x}, t)$, calculate the external force term using equation 3.13 $\boldsymbol{F}(\boldsymbol{x}, \boldsymbol{u}) = -((I_S(\boldsymbol{x} - \boldsymbol{u}) - I_T(\boldsymbol{x}))\nabla I_S|_{\boldsymbol{x}-\boldsymbol{u}})$.
2. Solve equation 3.2 for the incremental update $\delta\boldsymbol{u}^{\boldsymbol{k}}(\boldsymbol{x})$ using a standard 3D FFT method described by Modersitzki et al.[58].
3. Update the final displacement solution $\boldsymbol{u}^{k+1}(\boldsymbol{x})$ by using the formula $\boldsymbol{u}^{k+1}(\boldsymbol{x}) = \boldsymbol{u}^{k}(\boldsymbol{x}) + \delta\boldsymbol{u}^{\boldsymbol{k}}(\boldsymbol{x})$.
4. If the cost function in equation 3.8 increases as compared to the previous iteration, then stop or if $k \geqq k_{max}$, then stop. Otherwise move to step 5.
5. Let $k = k + 1$ and go to step 1.

The fluid registration algorithm is similar to the elastic method with the exception that in fluid registration, the linear PDE is solved to smooth the velocity field instead the deformation field. The fluid registration algorithm has two added steps (step 3 and 4 as shown in Algorithm 3.2) for calculating the deformation from the velocity field:

Algorithm 3.2 Classic Fluid registration

Initialize the iteration $k = 0$, $t = 0$ and $\boldsymbol{u}(\boldsymbol{x}, 0) = 0$.

1. Given $\boldsymbol{u}(\boldsymbol{x}, t)$, calculate the external force term using equation 3.13
   $\boldsymbol{F}(\boldsymbol{x}, \boldsymbol{u}) = -((I_S(\boldsymbol{x} - \boldsymbol{u}) - I_T(\boldsymbol{x}))\nabla I_S|_{\boldsymbol{x}-\boldsymbol{u}})$.
2. Solve the linear PDE equation 3.5 for the instantaneous velocity $\boldsymbol{v}(\boldsymbol{x}, t)$ using a standard 3D FFT method described by Modersitzki et al. [58]. Steps 3-5 describe the procedure for solving equation 3.7, advancing $\boldsymbol{u}(\boldsymbol{x}, t)$ in time.
3. Calculate the perturbation of the deformation field $\boldsymbol{R}^k = \frac{\partial \boldsymbol{u}}{\partial t} = \boldsymbol{v} - \sum_{i=1}^{3} v_i \frac{\partial \boldsymbol{u}}{\partial x_i}$.
4. Calculate the time step using $\Delta t \leq \max(||\boldsymbol{R}^k||)\Delta \boldsymbol{u}$.
5. Advance equation 3.7 solving for $\boldsymbol{u}^{k+1}$
   $\boldsymbol{u}^{k+1} = \boldsymbol{u}^k + \boldsymbol{R}^k \Delta t$.
6. If the cost function in equation 3.8 increases as compared to the previous iteration, then stop or if $k \geqq k_{max}$, then stop. Otherwise move to step 7.
7. Let $t = t + dt$, $k = k + 1$ and go to step 1.

3.2 Topology Preservation

During the registration process, the structures in the source image might expand or compress to align with the corresponding target image structures. In certain regions of the image, the deformation field might undergo folding, an undesirable distortion of the deformation as shown in Figure 3.1 (d). A desirable property of intra-patient registration is the preservation of the topology of the anatomical structures and the avoidance of any folds. If the images for intra-patient registration have been acquired after a considerable period of time, there might occur a loss of structure between the two images as a result of resection or chemotherapy. Since, the intra-patient images considered in our work have been acquired mostly on the same day itself, hence any tissue loss will not need to be considered. Topology preservation helps to ensure that the neighborhood relationship between the structures is maintained

and the various connected structures remain connected. It also prevents the appearance or disappearance of existing or new structures. The preservation of the topology is also related to the continuity of the transformation and the one-to-one mapping between the target image and the deformed source image. The presence or absence of folding can be confirmed by inspecting the determinant value of the Jacobian of the deformation field. The determinant of the Jacobian of the deformation field is also commonly expressed as just the Jacobian of the deformation field. This term that measures the local volume change imposed by the transformation between the source and the target image. A negative Jacobian value indicates local folding. The Jacobian of the deformation field (determinant of the Jacobian of the deformation field) is calculated as:

$$J(Id + \boldsymbol{u}) = \begin{bmatrix} 1 + \frac{\partial u_x}{\partial x} & \frac{\partial u_x}{\partial y} & \frac{\partial u_x}{\partial z} \\ \frac{\partial u_y}{\partial x} & 1 + \frac{\partial u_y}{\partial y} & \frac{\partial u_y}{\partial z} \\ \frac{\partial u_z}{\partial x} & \frac{\partial u_z}{\partial y} & 1 + \frac{\partial u_z}{\partial z} \end{bmatrix}, \tag{3.14}$$

where Id is the identity matrix and $J(Id+\boldsymbol{u})$ denotes the Jacobian matrix of the deformation field (determinant of the Jacobian of the deformation field) . An illustration of the range of Jacobian values for the various transformations to the deformation field is displayed in Figure 3.1. If there is an expansion of the local volume , the Jacobian is greater than 1, while the Jacobian lies between 0 and 1 during contraction . Estimating the Jacobian value is an essential tool to qualitatively assess the deformations.

Many techniques have been suggested for preservation of topology in image registration. Christensen et al. [95] proposed to preserve the topology by jointly estimating the forward and reverse transformations between the two images and constraining these transformations to be inverses of each other. Topology preservation can also be ensured by composing a sequence of free-form deformations (FFDs) while ensuring that individual FFDs are one-to-one transformations [96]. Chun et al. [97] preserved topology by using a modified quadratic penalty function that imposed condition for one-to-one transformations directly on the B-spline coefficients. Another approach to preserve topology is to use stationary velocity fields

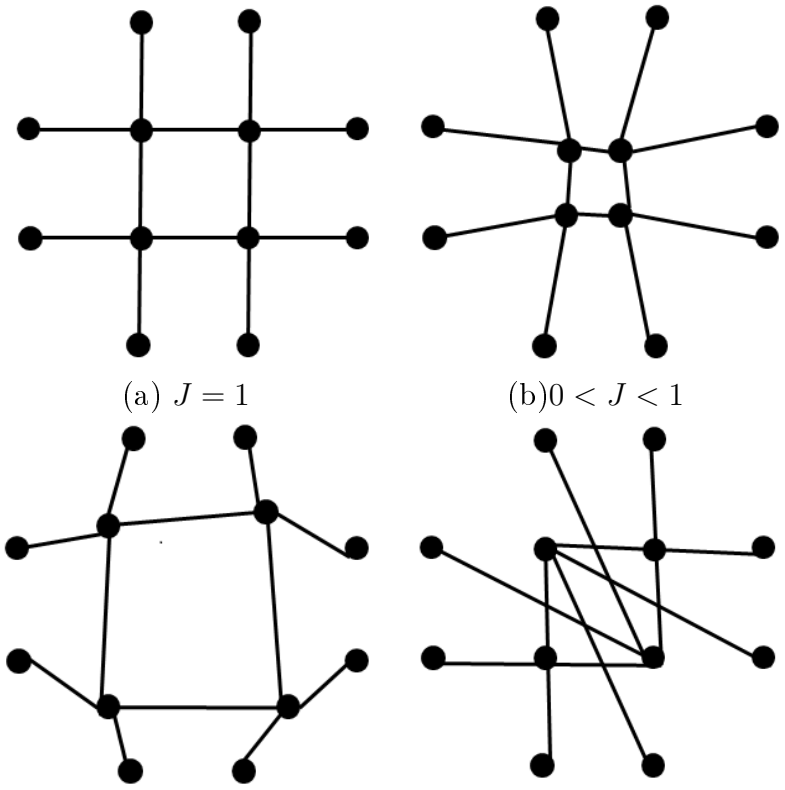

(a) $J = 1$ (b)$0 < J < 1$

(c)$J > 1$ (d)$J < 0$

Figure 3.1: Jacobian value of the deformation field : (a) Without any deformation (b) With contraction (c) With expansion (d) With folding of the deformation field.

which are integrated through exponential maps [98]. None of these methods can be directly incorporated into the elastic and fluid framework.

To solve the challenge posed by topology preservation, we propose to incorporate the approach taken by Yanovsky et al. [99] into the elastic and fluid registration framework. Yanovsky et al. [99] proposed the use of the statistical distribution of the Jacobian maps in the logarithmic space to define a log-unbiased deformation. The method consists of three steps:

3.2.1 Quantifying the Magnitude of the Deformations using Information Theory

The inverse of the deformation field $\boldsymbol{u}$ is denoted as $\boldsymbol{u}^{-1}$ and the Jacobian matrix of $\boldsymbol{u}$ as $J(\boldsymbol{u})$. The Jacobian of the deformation map is defined as the determinant of the Jacobian

matrix of the deformation. The underlying assumption for the topology preserving term is that the deformation field is globally volume preserving. As $\boldsymbol{u}$ and $\boldsymbol{u}^{-1}$ are bijective and globally volume preserving, the preservation of global density can expressed as:

$$\int_{\Omega} \mid J(\boldsymbol{u}) \mid d\boldsymbol{x} = 1, \tag{3.15}$$

$$\int_{\Omega} \mid J(\boldsymbol{u^{-1}}) \mid d\boldsymbol{x} = 1. \tag{3.16}$$

Given the constraint for global preservation of volume, we can associate the three probability functions of $\boldsymbol{u}$, $\boldsymbol{u}^{-1}$ and the identity matrix (id) with the Jacobian values in the following manner:

$$P_{\boldsymbol{u}} =\mid J(\boldsymbol{u}) \mid, \tag{3.17}$$

$$P_{\boldsymbol{u^{-1}}} =\mid J(\boldsymbol{u^{-1}}) \mid, \tag{3.18}$$

$$P_{id} = 1. \tag{3.19}$$

The next step involves translating this association to quantify the deformation field. This is done using the symmetric Kullback-Leibler distance measure from information theory defined as:

$$sKL(P_{\boldsymbol{u}}, P_{Id}) = KL(P_{\boldsymbol{u}}, P_{Id}) + KL(P_{Id}, P_{\boldsymbol{u}}), \tag{3.20}$$

where KL is the non-symmetric Kullback -Leibler distance between two density functions and is defined as:

$$\begin{aligned} KL(P_{\boldsymbol{u}}, P_{Id}) &= \textstyle\int_{\Omega} P_{\boldsymbol{u}} log \frac{P_{\boldsymbol{u}}}{P_{Id}} d\boldsymbol{x}, \\ &= \textstyle\int_{\Omega} |J(\boldsymbol{u})| \, log \frac{|J(\boldsymbol{u})|}{1} d\boldsymbol{x} \end{aligned} \tag{3.21}$$

Thus symmetric Kullback-Leibler distance (sKL) can be further simplified as:

$$sKL = KL(P_{\boldsymbol{u}}, P_{Id}) + KL(P_{Id}, P_{\boldsymbol{u}}),$$

$$sKL = \int_{\Omega} P_{\boldsymbol{u}} log \frac{P_{\boldsymbol{u}}}{P_{Id}} d\boldsymbol{x} + \int_{\Omega} P_{id} log \frac{P_{id}}{P_{\boldsymbol{u}}} d\boldsymbol{x},$$

$$sKL = \int_{\Omega} |J(\boldsymbol{u})| \, log \frac{|J(\boldsymbol{u})|}{(1)} d\boldsymbol{x} + \int_{\Omega} (1) \, log \frac{(1)}{|J(\boldsymbol{u})|} d\boldsymbol{x},$$

$$sKL = \int_{\Omega} (J(\boldsymbol{u}) - 1) \, log|J(\boldsymbol{u})| \, d\boldsymbol{x}. \tag{3.22}$$

Equation 3.22 is used as the energy functional to design the force term for topology preservation.

$$\boldsymbol{E_2(u)} = \int_{\Omega} (J(Id + \boldsymbol{u}(\boldsymbol{x})) - 1) log|J(Id + \boldsymbol{u}(\boldsymbol{x}))| d\boldsymbol{x}. \tag{3.23}$$

This energy term would increase in value whenever the deformation field experience a large change in volume (contraction or exapnsion). For example if a region of the deformation field is moving towards folding the logarithmic value of the Jacobian would increase and the energy term would increase with it. The energy term in equation 3.23 only approaches zero when the deformation $\boldsymbol{u}(\boldsymbol{x})$ is volume preserving everywhere (Jacobian value of $\boldsymbol{u}(\boldsymbol{x})$ is 1 everywhere). By treating this energy term as a cost and minimizing it, we introduce a force term that will add as a topology preserving constraint to the registration methodology. This force term will help to evenly distribute the deformations to avoid a large change in local volume and reduce the standard deviation in Jacobian values.

3.2.2 Formulation of the External Force Component

Minimizing this energy functional in equation 3.23 leads to an external force component due to the topology constraint defined as:

$$\boldsymbol{F}_2(\boldsymbol{x},\boldsymbol{u}) = \gamma \begin{bmatrix} -\frac{\partial}{\partial x}\left(\frac{\partial u_y}{\partial x}L'\right) + \frac{\partial}{\partial y}\left(\frac{\partial u_y}{\partial x}L'\right) \\ \frac{\partial}{\partial x}\left(\frac{\partial u_x}{\partial y}L'\right) - \frac{\partial}{\partial y}\left(\frac{\partial u_x}{\partial x}L'\right) \end{bmatrix}, \tag{3.24}$$

where $L' = L'(J(Id+\boldsymbol{u})) = 1 + log|J(Id+\boldsymbol{u})| - \frac{1}{J(Id+\boldsymbol{u})}$ and γ represents a scalar weighting factor for the topology force component. Thus, the new external force is expressed as an addition of the force derived from similarity $\boldsymbol{F}_1$ (equation 3.13) and the topology constraint force $\boldsymbol{F}_2$ as shown below:

$$\boldsymbol{F}(\boldsymbol{x},\boldsymbol{u}) = \boldsymbol{F}_1(\boldsymbol{x},\boldsymbol{u}) + \boldsymbol{F}_2(\boldsymbol{x},\boldsymbol{u}). \tag{3.25}$$

The derivation of the 3D version of the $\boldsymbol{F}_2$ term for the topology constraint is provided in Appendix B.

3.3 Rigidity Preservation

Spatially homogenous regularizers used in non-rigid registration techniques apply a uniform smoothing of the deformation field defined over the image space. A globally uniform smoothing across different organs in the image will however not necessarily lead to physically or physiologically plausible deformations for the human body. The chest contains both soft and rigid tissues. Soft tissues, such as the lungs require more freedom in movement and can deform in a non-rigid manner. However, for rigid objects like the ribs and the spine, any non-rigid behavior needs to prevented and their movement must be constrained to be linear. A vast majority of current registration techniques treat the entire image as a single flexible object with the same physical properties. This approach creates a problem for rigid structures such as the bones, the ribs and the spine; and may lead to implausible deformations.

An example of the effect of uniform smoothing on the bones is shown in Figure 3.2. The source and the target images are registered by FFD using B-splines method as described in Rueckert et al. [44]. The spine and the ribs undergo a change in shape and volume that is not physically plausible for intra-subject registration. Thus, an additional constraint or model component is needed to compensate for globally uniform smoothing.

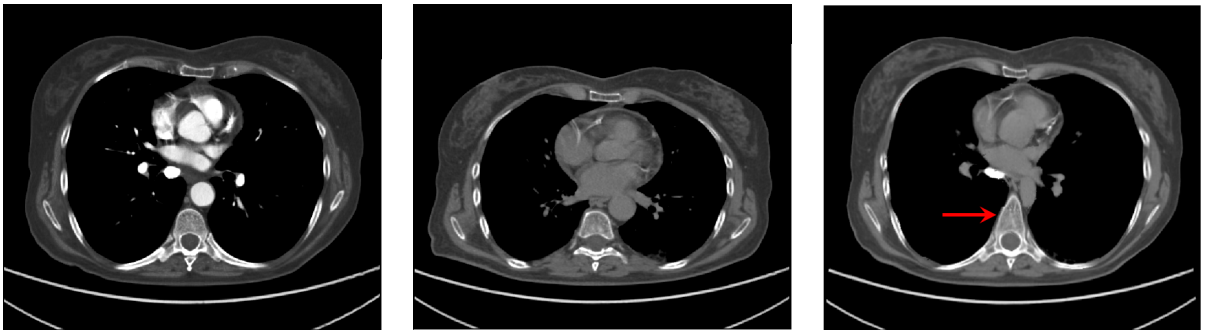

(a) (b) (c)

Figure 3.2: (a) Target image (b) Source image (c)Transformed source image using B-spline FFD registration. The implausible deformations of the spine is highlighted using a red arrow.

A range of approaches has been investigated to address the problem of rigid motion of the bones and the non-rigid motion of the soft tissues in image registration. For example, Little et al. [100] developed a method that allows the segmented vertebrae to move as individual rigid bodies, while the surrounding tissue was smoothly deformed using a combination of inverse-distance weighted interpolation and radial basis function interpolation. Edwards et al. [101] modeled a three component system consisting of elastic, fluid and rigid regions, for 2D brain shift compensation. A biomechanical finite element model was incorporated into the registration process by Ferrant et al. [102] to drive the registration process in intra-operative brain imaging. Lester et al. [103] employed spatially varying Lamé parameters within the fluid registration to achieve locally adaptable regularization in head and neck images. Tanner et al. [104] coupled the control points of a B-spline deformation to enforce rigidity within breast tumours. Miller et al. [105] classified chest CT images into regions with linear and non-linear displacements and then regularized them based on their individual transformation model. Staring et al. [85] applied an adaptive filter on a B-spline control point mesh to preserve the rigidity of bones in thoracic images.

To preserve the rigidity of the bones, we adopt the concept of a spatially varying filter proposed by Staring et al. [85] into the elastic and fluid registration frameworks. The method proposed by Staring et al. [85] The preservation of the rigid structures is achieved by filtering the deformation field using a spatially varying filter. The filtering step is used to calculate the average amount of deformation around local regions of voxels, and then assigning this mean deformation to be the deformation at that particular voxel. Estimation of a stiffness coefficient map $c(\boldsymbol{x})$ forms the first stage of the filter design. The stiffness map encodes the rigid properties of each voxel and can be obtained by thresholding the Hounsfield units at bone attenuation level from the CT image. The map assigns a value close to zero for highly deformable materials such as soft tissues and a value close to one for rigid structures like bones. The second stage of the filtering process then calculates the mean deformation $\boldsymbol{m}(\boldsymbol{x})$ for each pixel neighborhood using:

$$\boldsymbol{m}(\boldsymbol{x}) = \frac{\sum c(\boldsymbol{x})\boldsymbol{m}(\boldsymbol{x})}{\sum c(\boldsymbol{x})}. \tag{3.26}$$

Finally, the filter assigns a value close to the mean deformation at location $\boldsymbol{x}$ when the stiffness coefficient $c(\boldsymbol{x})$ is high and a value close to the original deformation $\boldsymbol{u}$ for low stiffness coefficients as shown in the following equation:

$$\boldsymbol{u}_{\text{new}} = (1 - c(\boldsymbol{x}))\boldsymbol{u} + c(\boldsymbol{x})\boldsymbol{m}(\boldsymbol{x}). \tag{3.27}$$

This helps to ensure that rigid deformations are achieved in regions where the tissue is fairly stiff, whereas regions with low stiffness can deform freely. The rigidity preservation term is based on a weighted mean. Hence, the movement of the bones will slowly be transformed into a translational field. The rigidity preservation term does not allow rotation of the rigid structures.

3.4 Phantom Data Studies

We aim to propose new elastic and fluid frameworks which preserve the topology of the deformation field and the rigidity of the bones. These new frameworks are compared with the classic elastic and fluid methods on phantom data. Thus, the four algorithms used for this phantom study are:

1. Classic elastic registration,
2. Classic fluid registration,
3. Constrained elastic registration (including topology and rigidity constraints),
4. Constrained fluid registration (including topology and rigidity constraints).

The algorithms for the constrained elastic and fluid framework are described in algorithms 3.3 and 3.4 respectively.

Algorithm 3.3 Constrained elastic registration

Initialize the iteration $k = 0$ and $\boldsymbol{u^0}(\boldsymbol{x}) = 0$.

1. Given $\boldsymbol{u^k}(\boldsymbol{x}, t)$, calculate the external force term using equation 3.25 $\boldsymbol{F}(\boldsymbol{x}, \boldsymbol{u}) = \boldsymbol{F}_1(\boldsymbol{x}, \boldsymbol{u}) + \boldsymbol{F}_2(\boldsymbol{x}, \boldsymbol{u})$.
2. Solve equation 3.2 for the incremental update $\delta\boldsymbol{u^k}(\boldsymbol{x})$ using the standard 3D FFT method described by Modersitzki et al. [58].
3. Update the final displacement solution $\boldsymbol{u}^{k+1}(\boldsymbol{x})$ by using the formula $\boldsymbol{u}^{k+1}(\boldsymbol{x}) = \boldsymbol{u}^k(\boldsymbol{x}) + \delta\boldsymbol{u^k}(\boldsymbol{x})$.
4. Apply the spatially varying filter mentioned in equation 3.27 to preserve the rigidity of the bones
5. If the cost function in equation 3.8 increases as compared to the previous iteration, then stop or if $k \geqq k_{max}$, then stop. Otherwise move to step 6.
6. Let $k = k + 1$ and go to step 1.

Algorithm 3.4 Constrained fluid registration

Initialize the iteration $k = 0$, $t = 0$ and $\boldsymbol{u}(\boldsymbol{x}, 0) = 0$.

1. Given $\boldsymbol{u}(\boldsymbol{x}, t)$, calculate the external force term using equation 3.25
   $\boldsymbol{F}(\boldsymbol{x}, \boldsymbol{u}) = \boldsymbol{F}_1(\boldsymbol{x}, \boldsymbol{u}) + \boldsymbol{F}_2(\boldsymbol{x}, \boldsymbol{u})$.
2. Solve the linear PDE equation 3.5 for the instantaneous velocity $\boldsymbol{v}(\boldsymbol{x}, t)$ using the standard 3D FFT method described by Modersitzki et al. [58]. Use the external force component in equation 3.25 will also consist of the topology preserving force. Steps 3-5 describe the procedure for solving equation 3.7, advancing $\boldsymbol{u}(\boldsymbol{x}, t)$ in time.
3. Calculate the perturbation of the deformation field $\boldsymbol{R}^k = \frac{\partial \boldsymbol{u}}{\partial t} = \boldsymbol{v} - \sum_{i=1}^{3} v_i \frac{\partial \boldsymbol{u}}{\partial x_i}$.
4. Calculate the time step using $\Delta t \leq \max(||\boldsymbol{R}^k||)\Delta \boldsymbol{u}$.
5. Advance equation 3.7 solving for $\boldsymbol{u}^{k+1}$
   $\boldsymbol{u}^{k+1} = \boldsymbol{u}^k + \boldsymbol{R}^k \Delta t$.
6. Apply the spatially varying filter mentioned in equation 3.27 to preserve the rigidity of the bones.
7. If the cost function in equation 3.8 increases as compared to the previous iteration, then stop or if $k \geqq k_{max}$, then stop. Otherwise move to step 8.
8. Let $t = t + dt$, $k = k + 1$ and go to step 1.

3.4.1 Parameter Selection

3.4.1.1 Elastic and Fluid Transformation

The focus of the constrained registration algorithm is to obtain a biologically meaningful deformation. In our experiments, we choose $\lambda = 0$ so that the tensile stress would produce only a stretch without a lateral shrink. This is also the common choice used in earlier work by Bajcsy et al. [55] and Broit et al. [54]. The choice of μ is explicitly stated for the experiments and varies according to the extent of deformation required to successfully match the images. For large deformations a lower value of μ is used to recover the deformations while we use a higher value of μ for smaller deformations to achieve a meaningful registration. For all the

experiments, the maximal displacement of the voxel per iteration is defined not more than 0.5 times the voxel size. If the displacement for a particular iteration exceeds more than the set limit, we re-scale the actual displacement such that the norm of the re-scaled displacement becomes 0.5 times voxel size. For all the experiments in this section, the Lamé parameters are set as $\lambda = 0$ and $\mu = 100$. A detailed analysis of the Lamé parameters is provided in Appendix C.

3.4.1.2 Topology Preservation

For topology preservation, the scalar variable γ is used as the weighting term for the topology preserving force. The objective of topology preservation is to prevent the folding of the deformation field but there should also be maximum alignment of the matching regions. If γ is set at a lower value then the registration might not be able to prevent folding and if it is set at a very high value then the effect of the similarity measure force will be suppressed. The topology weighing factor has been empirically selected after experimenting with a range of values for γ.

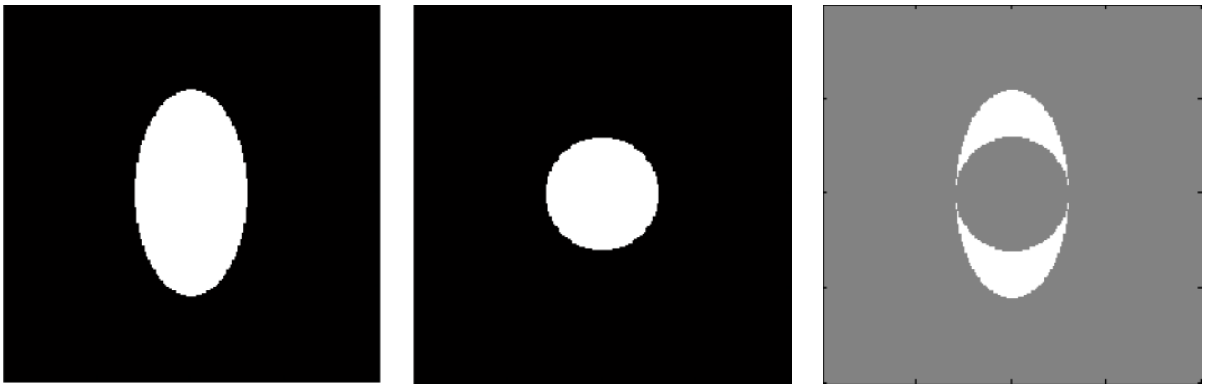

(a)Target Image (b)Source image (c) Difference image

Figure 3.3: Circle to ellipse example: Target, source and difference images.

An initial experiment was conducted to register the 2D images shown in Figure 3.3 using values of $\gamma = \{0, 0.25\ 1.0\}$ for the same number of iterations. The circle in Figure 3.3(b) is the source image while the target image is the ellipse is shown in Figure 3.3(a). When $\gamma = 0$, the registration algorithm behaves like the classic elastic registration method and as the value of γ increases, the log-unbiased force component becomes active. The deformed source results for

$\gamma = 0$ and $\gamma = 0.25$ generate a close match between the deformed image and the target image. However, the x and y deformations produced as a result of the registration process for $\gamma = 0$ and $\gamma = 0.25$ are very different as seen in 3.4 (d)-(e) and (g)-(h), respectively. The Jacobian maps for the two values of γ are also very different as shown in Figure 3.4 (j) and (k). In case of $\gamma = 0$, we find that there is a high standard deviation of 0.3654 in the Jacobian values. The minimum Jacobian value for the image domain is also very low at 0.0819 which is close to folding of the deformation. This shows that without the topology constraint the registration solution moves towards folding. When $\gamma = 0.25$, the standard deviation of Jacobian values is 0.1683 while the minimum Jacobian value is 0.4721. Thus, the topology constraint has shown a better performance by providing a plausible solution. The registration for $\gamma = 1.0$ was not able to fully match the source with the target image even after running for the same number of iterations as shown in Figure 3.4(c) . This occurs because the topology preserving term starts dominating over the similarity measure force term leading to slower approach towards the final solution. The registration algorithm requires a balance between the preservation of topology and the similarity measure. Thus, for all our experiments, the value of γ is set to 0.25 to achieve that balance.

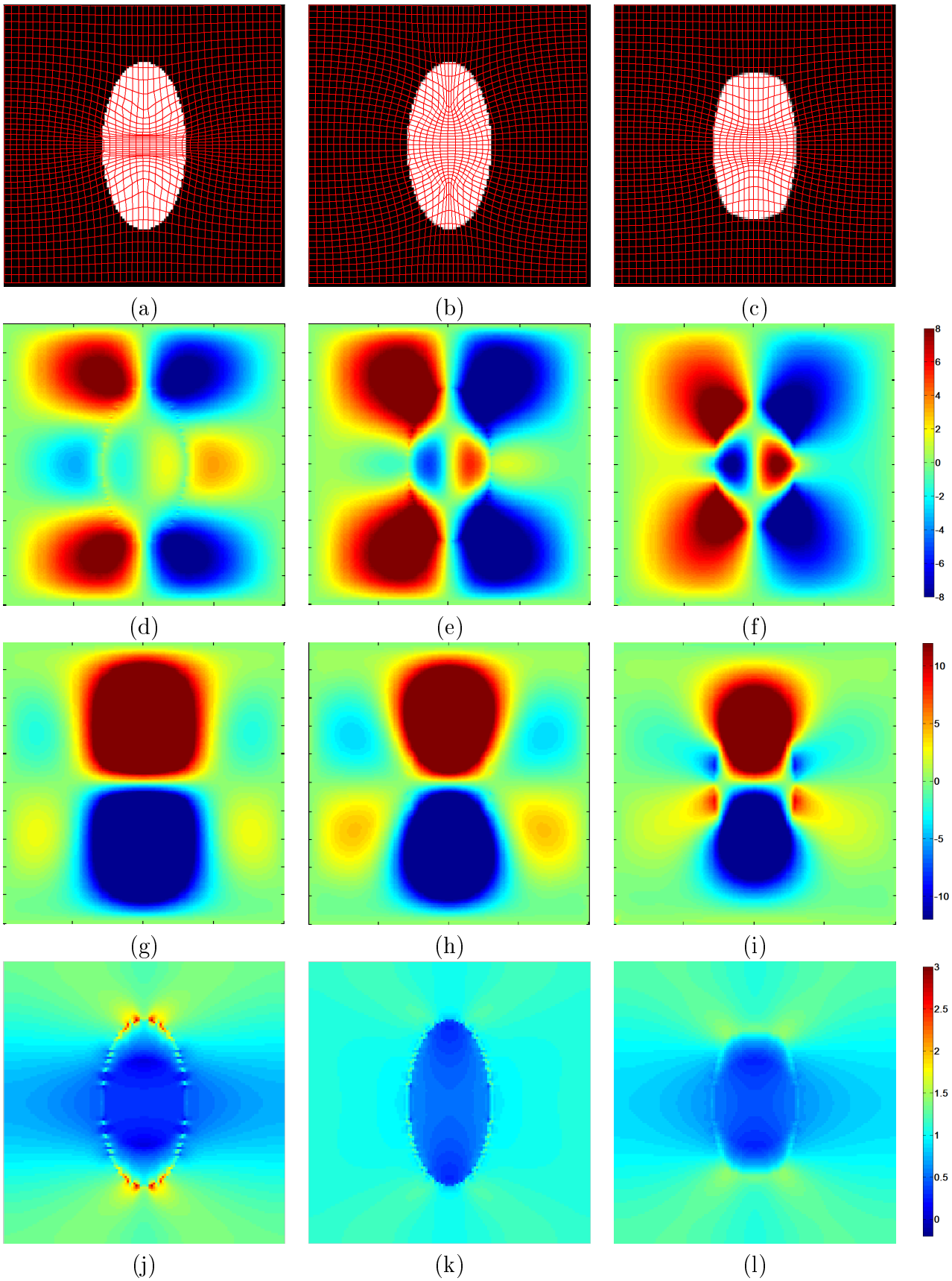

Figure 3.4: Results for elastic registration with topology preservation term and increasing values of weighing factor γ from 0, 0.25 and 1 (left to right). 1st row: Transformed source images, 2nd row: Deformation field along x, 3rd row: Deformation field along y, 4th row: Map of Jacobian values.

3.4.1.3 Rigidity Preservation

One of the initial tasks to implement the rigidity preservation in our framework is to segment the bones to calculate the local stiffness map $c(\boldsymbol{x})$. This process is done manually by selecting a threshold for the bones and using that for the segmentation. The stiffness coefficient $c(\boldsymbol{x})$ for bones is set at 0.9 while the stiffness coefficient for the non-rigid tissue is set at 0.1. The spatially adaptive filter is generally performed every nth iterations as to yield a smoother deformation field. For all of our experiments, we apply the filter every two iterations to maintain the rigidity of the bones.

3.4.2 NCAT Images and Evaluation Criteria

All the algorithms were tested on a phantom dataset generated from the 4D NURBS (Non-Uniform Rational B-Splines) Cardiac Torso (NCAT phantom) toolkit developed by Segars [106]. The CT volumes obtained from this phantom provide a plausible simulation of cardiac and respiratory motion in a normal human subject. NURBS surfaces were used to generate the complex organ shapes in the NCAT phantom. Five CT volumes were generated at different breathing stages, starting from full expiration to full inspiration. The generated images have a resolution of 192×192×192 with an isotropic voxel size of 0.48 *mm*. Gaussian noise with zero mean and a variance of 0.05 has been added to the images. Figure 3.5 shows an example of two breathing stages of the NCAT phantom along with the difference between the images. The Lamé parameters during registration are set as $\lambda = 0$ and $\mu = 100$.

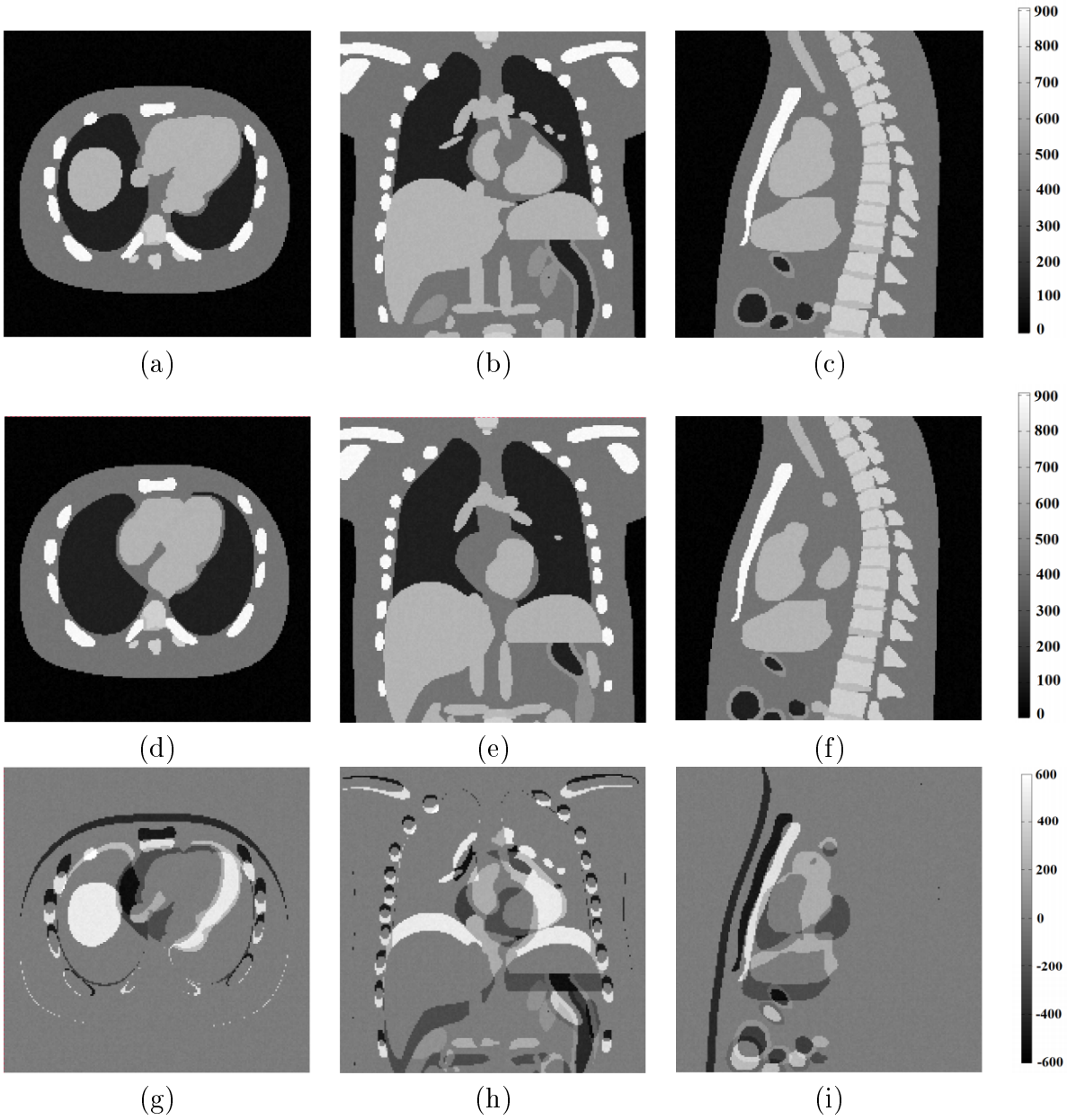

Figure 3.5: (a), (b) and (c): Orthogonal slices through the target image (first breathing stage of NCAT phantom). (d), (e) and (f): Orthogonal slices through the source image (here, the fourth breathing stage of NCAT phantom). (g), (h) and (i): Orthogonal slices through the difference image, when subtracting the source from the target.

The different registration methods are quantitatively validated by measuring the volume overlap of the organs (lungs, liver, ribs and spine) in the target and the source images after registration. The overlap ratio, also named Dice similarity coefficient (DSC), is defined as:

$$DSC = \frac{2|V_1 \cap V_2|}{|V_1| + |V_2|}, \tag{3.28}$$

where V_1 and V_2 are the number of voxels representing a particular organ in the target and the source image respectively. The average Dice coefficients are calculated for each organ and each registration. The quality of the deformation field is analyzed visually and also by computing the percentage of negative Jacobian values, i.e., number of voxels that have undergone folding.

3.4.3 Results and Discussion

The overlap ratios before and after registration using the four methods are shown in Table 3.1. The classic and the constrained fluid methods have shown an overall better performance in alignment of the various organs than the corresponding elastic techniques. The classic fluid method has an average overlap of 0.9726, while the constrained method has a slightly higher overlap of 0.9779. The overlap for the classic and constrained elastic methods have shown a comparatively lower overlap as they can only cope with small deformation and it is difficult to recover larger deformations due to the restrictive nature of the internal strain in the elastic continuum. The fluid version of the registration algorithm, in contrast, allows the relaxation of the forces over time, and consequently the recovery of larger deformation, leading to better overlap measures. The constrained fluid transformation has outperformed the classic fluid registration in overlap for all organs. Thus, with the selection of optimized parameters, the incorporation of the topology and the rigidity preservation terms does not affect the volume overlap.

Method \ Organ	Lungs	Ribs	Spine	Liver	Average
Before registration	0.8339	0.7797	0.9355	0.7342	0.8208
Classic elastic	0.9820	0.9021	0.9214	0.9211	0.9316
Elastic (topology+rigidity)	0.9756	0.9638	0.9538	0.9423	0.9589
Classic fluid	0.9923	0.9799	0.9632	0.9562	0.9726
Fluid (topology+rigidity)	**0.9964**	**0.9832**	**0.9639**	**0.9679**	**0.9779**

Table 3.1: Average overlap (Dice coefficient) of the individual organs for the NCAT phantom experiment.

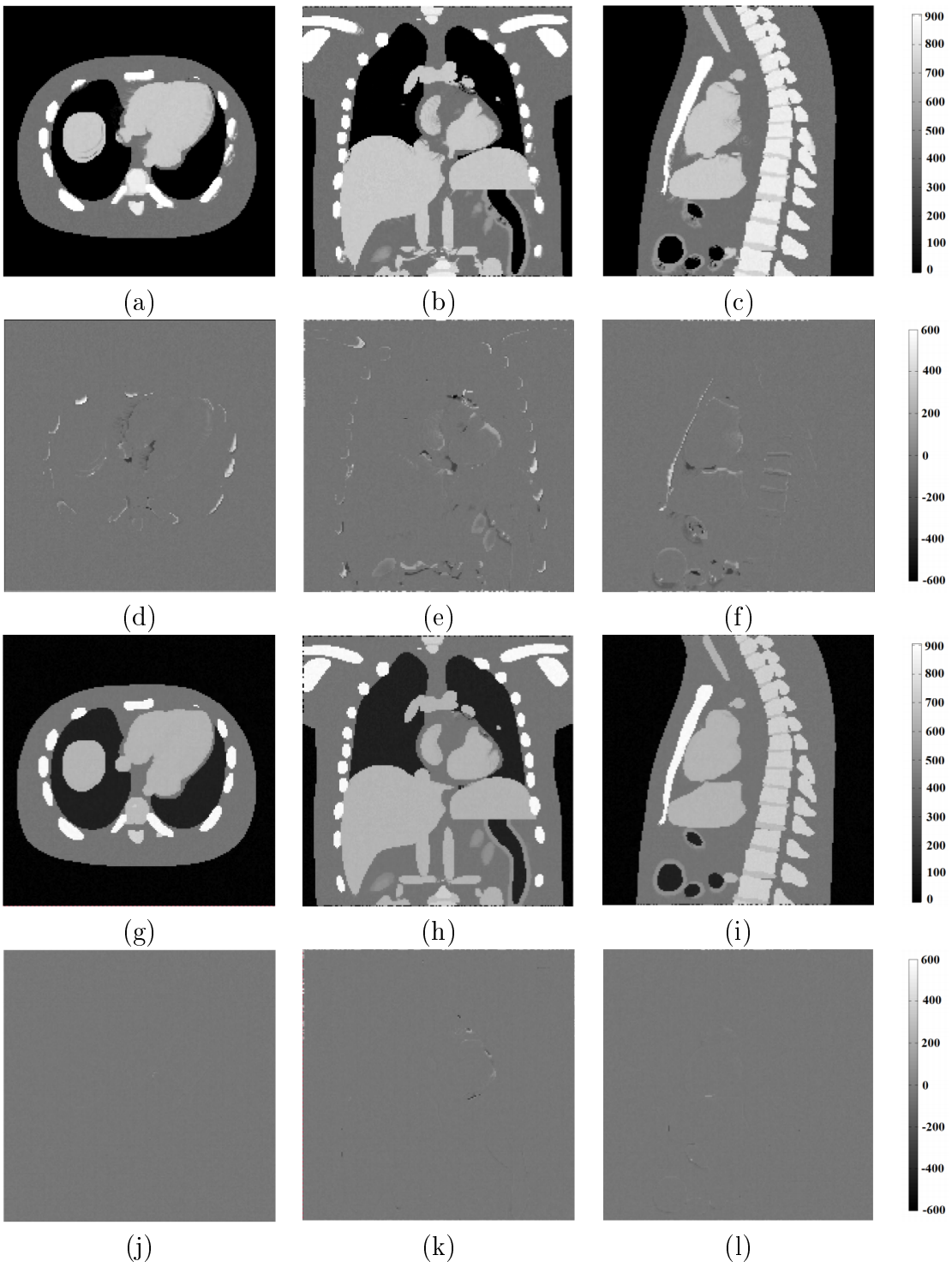

Figure 3.6: (a), (b) and (c): Transformed source image using the constrained elastic image registration technique on the NCAT phantom data. (d), (e) and (f) difference image between target and transformed source image obtained using the constrained elastic method. (g), (h) and (i): Transformed source image using the constrained fluid registration. (j), (k) and (l) difference image between target and transformed image obtained using the constrained fluid method.

In Figure 3.6, we show the deformed source and the difference images for the constrained

Pairs of registered images	Classic Elastic	Classic Fluid	Constrained Elastic	Constrained Fluid
2nd to 1st frame	0.39%	0.34%	0.00066%	0.00056%
3rd to 1st frame	1.1%	0.93%	0.00094%	0.00080%
4th to 1st frame	1.8%	1.3%	0.0022%	0.0012%
5th to 1st frame	3.1%	2.5%	0.0089%	0.0048%

Table 3.2: Percentage of negative Jacobian values for the registration methods.

elastic and the constrained fluid method. The constrained fluid registration incorporating the constraints is able to better recover the large deformations between the target and source images, including the expansion of the chest and lungs and the movement of the liver as seen from the difference images. The constrained elastic method has not fully recovered the deformation in aligning the lungs and also shows error in the overlap of other structures like the ribs.

Both the constrained elastic and fluid registration have succeeded in reducing the number of negative Jacobian values in comparison with both classic versions, as shown in Table 3.2. The constrained fluid method also results in slightly lower percentage of negative Jacobian than its elastic variant.

Table 3.3 lists the mean Jacobian values of the bones after the registration process. The Jacobian values of the bone help to quantify the extent of non-rigid deformations within the bones. If the mean value of Jacobian is close to 1, then amount of non-rigid deformations will be low. If it deviates away from 1 on either side, then the contribution of the non-rigid motion increases. The elastic and fluid version of the proposed constrained algorithm are the most successful ones in preventing the deformations of the bone while achieving a high overlap compared to the other techniques. The classic fluid registration has the worst performance as it gives greater freedom for deformations without any constraint. The non-rigid deformations of the bones for classic elastic and fluid method increases as larger deformations need to be recovered. There is an almost a negligible increase in the mean Jacobian values of the bones for constrained elastic and fluid methods over the increasing magnitude of deformation for different breathing cycles.

Pairs of registered images	Classic elastic	Classic fluid	Constrained elastic	Constrained fluid
2nd to 1st frame	1.10	1.17	1.01	1.01
3rd to 1st frame	1.14	1.21	1.03	1.02
4th to 1st frame	1.16	1.27	1.04	1.03
5th to 1st frame	1.21	1.33	1.05	1.05

Table 3.3: Jacobian values of the bones for the NCAT dataset. The constrained elastic and constrained fluid methods have better performance in comparison to classic elastic and classic fluid methods.

As illustrated in Figure 3.7, the constrained fluid and constrained elastic registration techniques are able to restrict any deformations within the ribs and preserve the rigidity whereas the classic elastic and classic fluid registration fails and allows their deformation.

3.5 Conclusion

In this chapter, we have the validated the incorporation of the topology preservation and the rigidity preservation methods into the elastic and fluid registration framework. We have also shown our justification for choosing $\gamma = 0.25$ as the weighing parameter value for the topology preserving term. As we increase the weighting the topology preserving term, the topology preservation term starts overtaking the similarity measure and preventing the registration process from achieving full deformation. The results from the previous section also show that the constrained fluid registration method has the best overall performance in terms of overlap ratios, quality of the deformation field and the preservation of rigidity of the bones. In Appendix D we have provided a detailed analysis of the effects of the constraints on an individual basis. In the next chapter, we validate the topology preservation and the rigidity preservation terms on real 3D data.

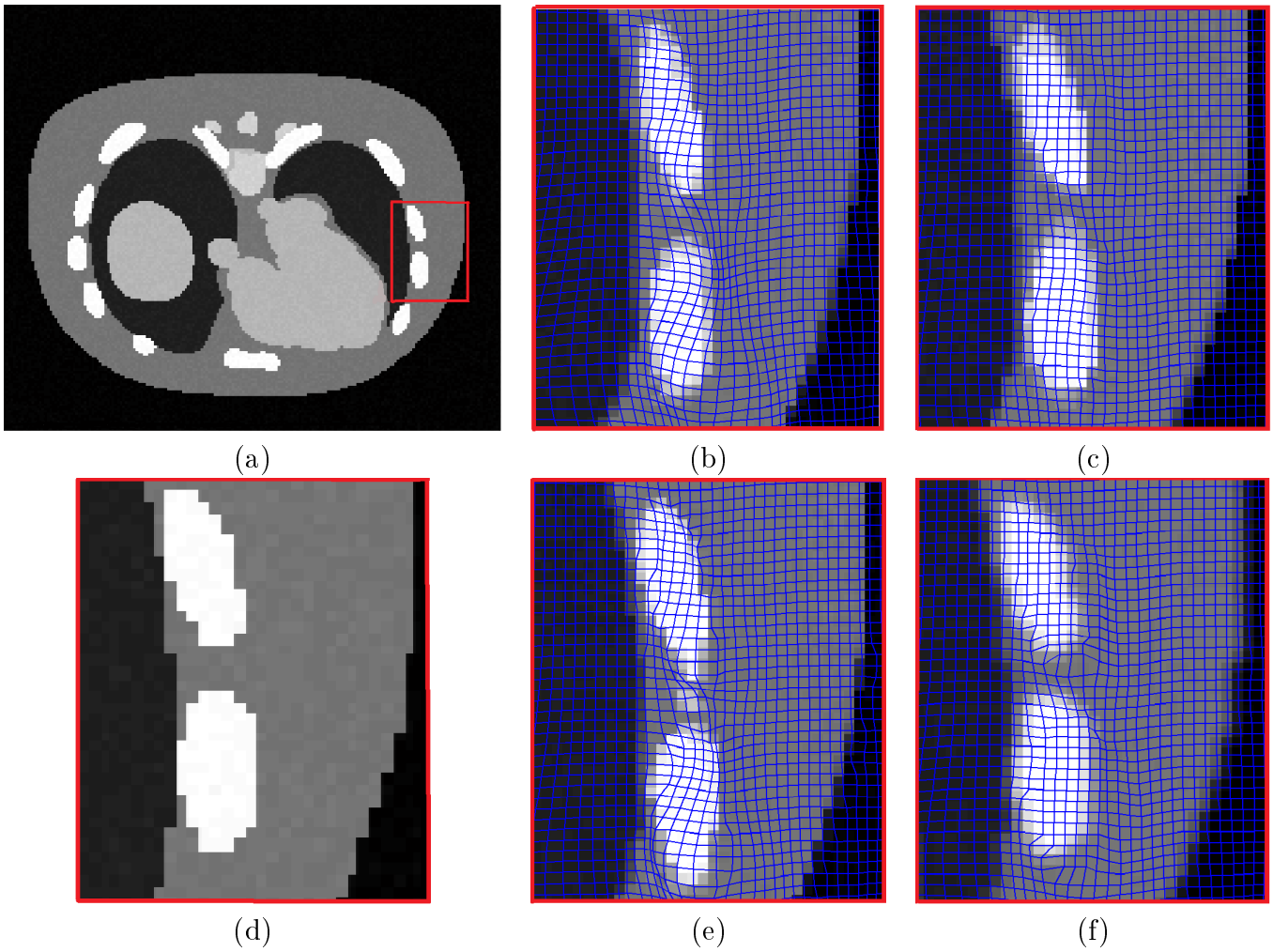

Figure 3.7: Preserving rigidity of the bones ; (a) Target image. (d) Zoomed image of the ribs (labeled by red box) in the target image. (b), (c), (e) and (f) Zoomed transformed images of the ribs with deformation field superimposed; the transformed images have been obtained using (b) the classic elastic registration, (c) the constrained elastic registration, (e) the classic fluid registration (f) the constrained fluid registration.

Chapter 4

Application of Elastic Registration Framework to EMPIRE10 Challenge Data

In this chapter, we apply the proposed elastic registration framework with topology and rigidity preservation constraints to real CT image volumes. We use the Evaluation of Methods for Pulmonary Image Registration (EMPIRE) challenge dataset comprising of thirty intra-patient thoracic CT images. The results were evaluated using criteria determined by the EMPIRE challenge and a couple of additional criteria. The results have provided us with valuable insight into the advantages and the shortcomings of the topology preserving, rigidity preserving constraint, and the elastic regularizer. In the final section, we also discuss the motivation to move towards the fluid registration framework.

4.1 EMPIRE10 Challenge

The EMPIRE10 challenge that was announced in April 2010 was organized as part of the Grand Challenges in Medical Image Analysis Workshop at the Medical Image Analysis and Computer Assisted Intervention (MICCAI) 2010 conference. We participated in the challenge and evaluated the elastic registration including topology and rigidity constraints. The

primary objective of the EMPIRE challenge was to provide a public platform for comparison of the available registration algorithms that are applied to a dataset of intra-patient thoracic CT image pairs. The challenge has also helped us to investigate the common problems of the existing state-of-the-art registration methods.

4.2 Material and Methods

4.2.1 Datasets

The EMPIRE challenge dataset consists of 30 intra-subject thoracic CT image pairs. The images are acquired from variety of sources and represent a variety of scenarios encountered in clinical practice. The scan pairs can be classified into 6 categories:

- Breathhold inspiration scan pairs
- Breathhold inspiration and expiration scan pairs
- Individual breathing phases of scan pairs
- Ovine data scan pairs
- Contrast and non-contrast scan pairs
- Artificially warped scan pairs

The scans have a slice thickness of 0.70 *mm* and in-plane pixel resolution varied from 0.66 *mm* to 0.80 *mm* with an average value of 0.74 *mm*. The images are cropped by the EMPIRE10 organizers using a bounding box around the lungs to reduce the volume of data. An example of the cropped image pairs is shown in Figure 4.1. The challenge also provided the participants with segmentations of the lungs. For this the CT images were segmented using an automatic hybrid method developed by van Rikxoort et al. [107], based on the conventional region growing technique with an additional error detection step. The segmentations are checked and altered manually where necessary. The lung segmentations are used to estimate the

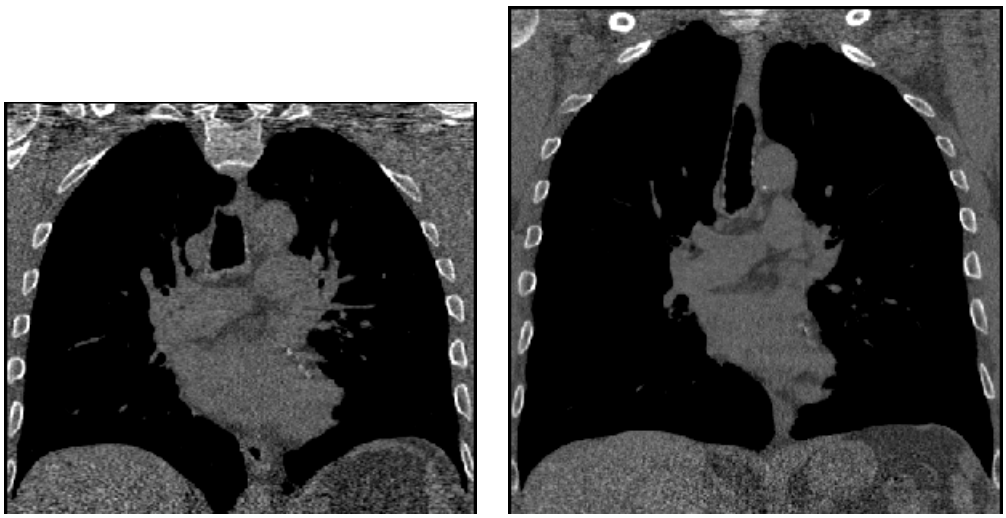

(a) Target Image (b) Source Image

Figure 4.1: Example of a cropped EMPIRE image pair.

registration accuracy or to use in the registration process. Details regarding the segmentation steps are provided in Murphy et al. [74] .

4.2.2 Evaluation Methodology

The evaluation criterion set by the EMPIRE challenge are based on the quantitative assessment of the registration accuracy for the lungs. These criteria are divided into four categories:

4.2.2.1 Alignment of Lung Boundaries

Aligning the lung boundaries is an important criterion for validation of pulmonary CT registration. The lung boundary for the source and the target images is derived from the lung segmentations. The voxels around the lung boundary are divided into two regions:

1. voxels that lie within 2 to 20 mm inside the boundary (Ω^{in})

2. voxels that lie within 2 to 20 mm outside the boundary (Ω^{out}).

These two regions Ω^{in} and Ω^{out} are defined for both the target and the source images, thus resulting in total of four regions Ω_T^{in} , Ω_T^{out} and Ω_S^{in} , Ω_S^{out} . The error in the lung boundary alignment is calculated as the percentage of incorrectly matched voxels that belong to one

region in the target image but are positioned into the opposite region in the transformed source image. The penalties incurred for the errors in the lung boundary alignment are described in more details in Murphy et al. [74]. The challenge does not investigate any other adjacent organ boundaries than the lung.

4.2.2.2 Folding of the Deformation Field

The EMPIRE challenge validation criterion also analyses the quality and the physical plausibility of the deformation field. The determinant of the Jacobian of the deformation field, also referred as the Jacobian, for each point in the lung is calculated. The Jacobian of the deformation field determines the local change in the volume, i.e., whether a local expansion or contraction had taken place. If the Jacobian value is less than 0, then the deformation field is defined to have undergone folding. The percentage of voxels that have undergone folding within the lungs is used to calculate the penalty incurred by the registration method. One problematic aspect with this criteria is that the Jacobian values for voxels outside the lung volume are disregarded. This does not provide a complete qualitative analysis of the deformation field as in many cases there might be large folding occurring outside the lungs.

4.2.2.3 Major Fissure Alignment

Fissures represent plate-like structures that divide the lungs into various lobes. Fissures are difficult to detect and hence register, and therefore present a very challenging task for the registration methods. Evaluating the alignment of the major fissure boundaries provides a complementary validation tool for pulmonary image registration in the EMPIRE challenge study. For the purpose of the study the fissures were segmented in all the images using an automatic algorithm developed by van Rikxoort et al. [108], the results were further inspected to remove any minor fissures manually. The analysis of the registration accuracy of the participating algorithms for the fissures was performed in a similar manner to the lung boundary alignment. Regions of 2-20 mm are defined on both sides of the fissures and the error was calculated based on the incorrectly matched voxels that move towards the opposite

side of the fissure. The error in fissure alignment was calculated as a percentage of checked points for which penalties were incurred. The fissure segmentations are not provided to the challenge participants.

4.2.2.4 Landmark Point Correspondence

The alignment of lung boundaries and major fissures provide an estimate of the registration accuracy for the large structures involving the lungs. To validate the alignment of smaller structures within the lungs, the EMPIRE10 challenge required to match distinctive landmarks between the target and the deformed source images. The third measure of registration accuracy for the EMPIRE challenge thus looks into the correspondence of annotated landmark pairs. For this purpose, a well distributed set of 100 distinctive landmarks were defined in the target and the source image from each scan pair. The procedure for the selection of these 100 landmarks is explained thoroughly in the work by Murphy et al. [109]. Based on the deformation field submitted by the participants, the Euclidean distance between the landmarks in the target and the landmarks in the deformed source image is calculated. For each registration of each scan pair, average distance, minimum distance and the maximum distance are computed. The landmarks have not been provided to the challenge participants.

4.2.2.5 Additional Criteria

The above mentioned EMPIRE evaluation criteria are only concerned with the registration accuracy inside the lung and does not inspect the performance of the registration for other surrounding structures or the chest as a whole. In particular, the assessment of the ribs and the mediastinum are not addressed in the challenge which leads to an incomplete representation of the registration accuracy for the chest CT images. Hence, to present a holistic evaluation of the registration process, we also investigate the rigidity of the ribs and the spine by means of visual inspection of the deformation field on the EMPIRE10 data. We also investigate the folding statistics for the entire image rather than focusing only on the lungs.

4.2.3 Experiments

We have applied two algorithms on the EMPIRE challenge datasets:

1. the classic elastic registration method, and

2. the constrained elastic registration framework

The challenge had been organized during the early period of our research and during this phase we were working only on the elastic registration model. Hence, the classic fluid and the constrained fluid algorithm were not included in the challenge. The constrained elastic framework consists of topology preserving and the rigidity constraint explained in Chapter 3. Registration for either method is carried out using the following steps:

1. Global motion is corrected using rigid body registration in order to initialize the deformation field. The rigid body registration aims at minimizing the SSD between the target and source lung images.

2. As a first approximation to the non-rigid deformations, the binary lung masks are non-rigidly registered in a multiresolution setting. This improves speed and robustness.

3. Finally the whole volumes, including the image areas outside the lungs such as the bones and other tissues are non-rigidly registered. Four levels of resolution are used, 200 iterations are performed for coarser levels while 50 iterations are performed at the finest level. The Lamé constant λ is set to zero while the value of μ ranges between 200 to 500 depending on the magnitude of the deformation.

4. The registrations were performed using a Microsoft Windows workstation of Intel Xeon CPU AT 2.4 GHz with 12 GB main memory and the code is implemented using ITK [110].

The images provided for the EMPIRE challenge were cropped using a bounding box to focus on the lungs and reduce the amount of data. The resultant image has abrupt cuts through organs like the liver and in some cases also through the ribs. To analyse the effect of the

image cropping on the performance of the topology preserving term for the elastic constrained method, we run another experiment using five image volumes (scan pair 1, 7 , 14 ,15 and 18) from the EMPIRE10 challenge datasets. However, for this experiment we provide some extra padding region around the image during registration. The image is padded with zeros for 20 mm around all the three axes. The images are then registered using classic elastic and constrained elastic registration technique. The padding of the image is removed after registration before performing any image data analysis. The results for this experiment are provided in Table 4.3.

4.3 Results and Discussion

The classic elastic and constrained elastic methods were applied on all 30 image pairs in the EMPIRE challenge dataset. Table 4.1 presents the total evaluation scores for the lung boundary scores averaged over both left and the right lung regions. The evaluation scores for both the methods are provided. Lower lung boundary scores indicate better overlap between the lungs and thus imply a better result. The elastic constrained method has performed slightly better than the classic elastic in aligning the lung boundary, as shown in Figure 4.3. The results have been provided by the EMPIRE10 organizers.

The worst performance in terms of lung boundary results was for the registration of scan pair number 21, and the best performance was for scan pair 17, for both methods. The registration of scan pair number 21 is difficult because it needs to recover very large deformations for the lungs and the cropping of the images cuts through many of the organs that causes problems in producing accurate correspondence within the lungs. The average lung boundary score for the classic elastic method was 0.225± 0.332 % while for the average lung boundary score for constrained elastic method is 0.187 ± 0.270 %.[1]

[1]Classic Elastic Registration Results: http://empire10.isi.uu.nl/res_oxfordelastic.php
Constrained Elastic Registration Results: http://empire10.isi.uu.nl/res_oxfordelasticconstraints.php

Scan Pair	Lung boundary score for constrained elastic method (% Error overall)	Lung boundary score for classic elastic method (% Error overall)
01	0.655	0.665
02	0.007	0.093
03	0.039	0.022
04	0.009	0.017
05	0.025	0.016
06	0.004	0
07	0.540	0.490
08	0.055	0.043
09	0.014	0.016
10	0.067	0.147
11	0.073	0.055
12	0.077	0.060
13	0.053	0.004
14	0.410	0.487
15	0.310	1.070
16	0.041	0.151
17	0	0
18	0.265	0.605
19	0.041	0.090
20	0.204	0.353
21	1.810	1.332
22	0.200	0.022
23	0.037	0.011
24	0.005	0.006
25	0.454	0.033
26	0.071	0.028
27	0.097	0.272
28	0.294	0.595
29	0.014	0.009
30	0.067	0.060
Average	**0.187 ± 0.270**	0.225 ± 0.332

Table 4.1: Lung boundary evaluation results.

In terms of the folding of the deformation field scores, the elastic constrained method shows slightly better results than the classic registration method in most of the cases with the exception of scan pair 21 where the constrained method has a score of 4.1% as shown in Table 4.2. The topology preservation term has been ineffective for scan pair 21 due to the cropping of the images. However, the constrained elastic method has reduced the occurrence

of folding within the lungs for most cases in comparison to the classic **elastic** method. The best registration results in this category do not show any folding within the lungs. As a part of our additional evaluation criteria, we also assess the standard deviation of the Jacobian values across the entire image for both the algorithms as shown in Figure 4.2. The standard deviation of the Jacobian values helps to indicate the distribution of the deformations and a low value indicates a more evenly distributed deformation field. As shown in Figure 4.2, the standard deviation of the Jacobian values for the constrained elastic method is lower and has thus been more successful spreading the deformations across the image making the deformation field more physically plausible. This is particularly useful for uniform expansion or compression of the tissues within the chest CT. While the range of extreme Jacobian values for the classic elastic registration method ranged from -20 to +60, for the proposed method it was found to be between -4 to +7.

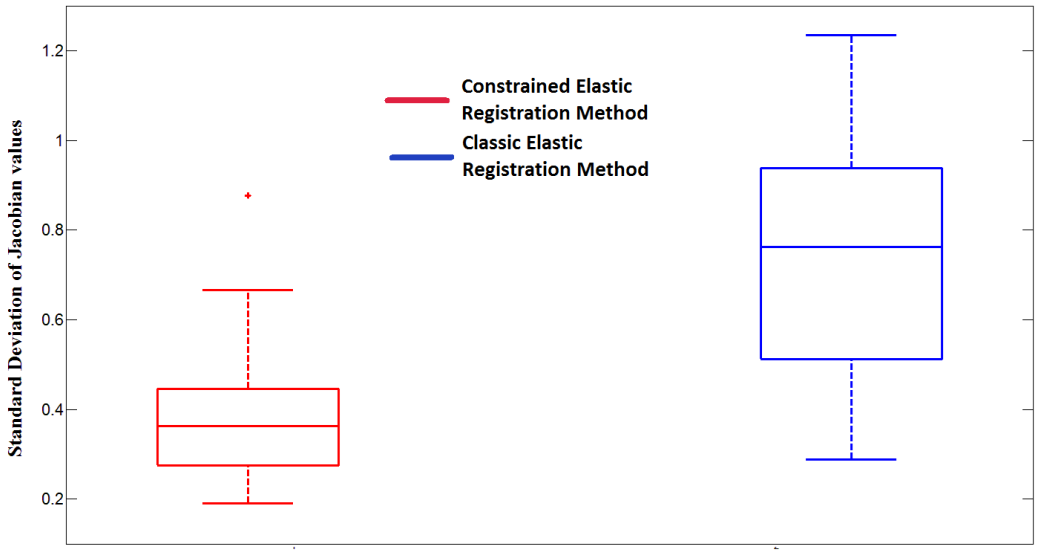

Figure 4.2: Box plot of the standard deviation of the Jacobian values from the two algorithms (for the entire image including the structures outside the lung)

Scan Pair	Folding of deformation field score for constrained elastic method(% Error overall)	Folding of deformation field score for classic elastic method (% Error overall)
01	0.8780	0.8787
02	0	0.0040
03	0.0002	0.0093
04	0.0044	0.0356
05	0.0005	0.0127
06	0	0
07	0.1886	0.4873
08	0.0045	0.0165
09	0.0016	0.0095
10	0.0167	0.0428
11	0.0181	0.0616
12	0.0204	0.0039
13	0	0
14	0.0538	0.1937
15	0.0429	0.0160
16	0.0333	0
17	0.0002	0
18	0.2349	0.2547
19	0.0006	0.0105
20	0.0701	0.1876
21	4.1045	1.2746
22	0.0209	0.0134
23	0.0004	0
24	0.0010	0.0170
25	0.0020	0.0070
26	0.0012	0.0002
27	0.0080	0.0143
28	0.5522	0.3384
29	0.0034	0.0142
30	0.0679	0.0241
Average	0.211± 0.745	0.130 ± 0.282

Table 4.2: Folding of the deformation field scores.

Figure 4.4 presents a comparison of the methods on the landmark and fissure alignment score. The constrained elastic method has an overall better performance than the classic elastic registration in mean alignment of the fissures and the landmarks.

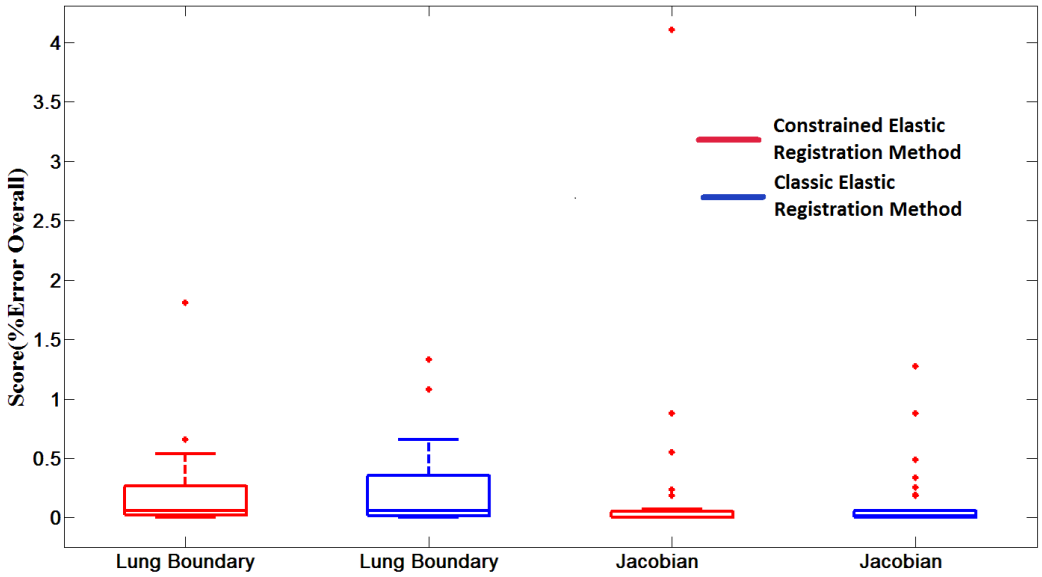

Figure 4.3: Box-plot of score (% Error overall) from the two algorithms for lung boundary and occurrence of negative Jacobian values (just for the lungs).

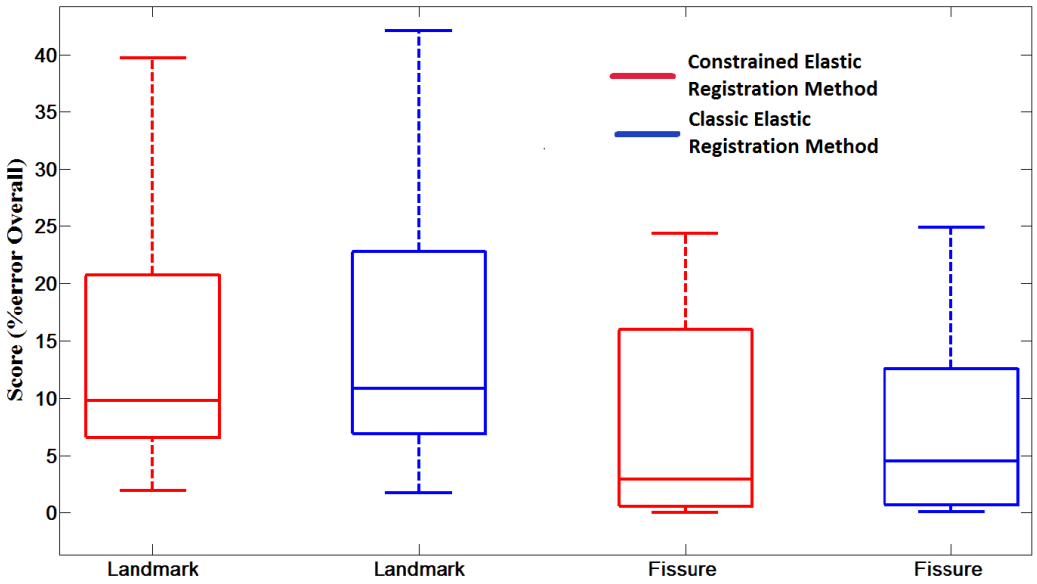

Figure 4.4: Box-plot of score (% Error overall) from the two algorithms for landmark and fissures.

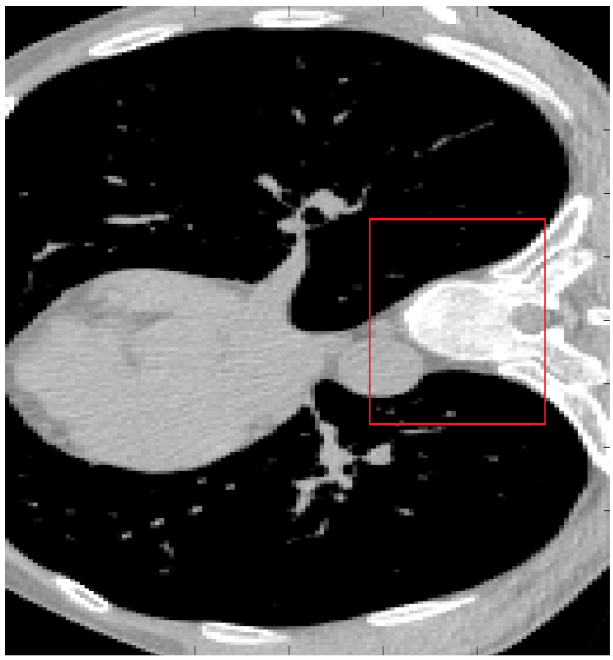

(a)

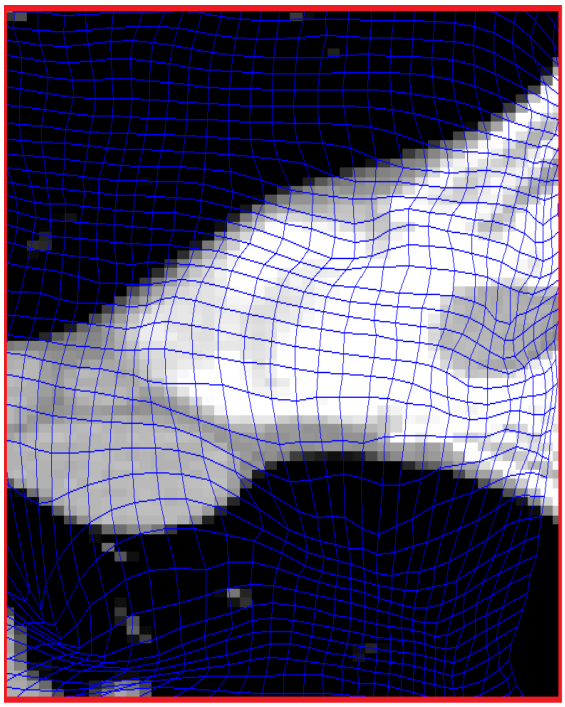

(b)

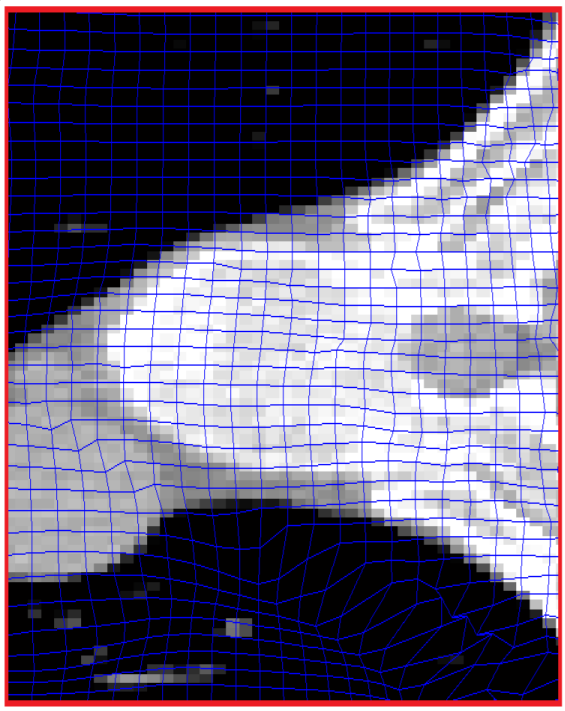

(c)

Figure 4.5: (a) Fixed image and zoomed image of a vertebra (labeled by the red box in the fixed image) with the deformation grid (b) Using elastic registration shows that it has failed in preserving the rigidity of the vertebra, (c) Using our proposed constrained elastic method clearly shows that the bones have not deformed and it has maintained its physical shape.

Figure 4.5(a) shows a single slice of the fixed image. Figure 4.5(b) displays the zoomed version of the deformed image through elastic registration with the overlay of the deformation grid. As seen in the Figure 4.5(b), the classic elastic registration technique has failed to preserve the rigidity of the bones and deforms the spine like a elastic object. This non-linear deformation of the spine does not represent the true rigid nature of the bones that allow only for linear deformation like translation or rotation. However, the constrained elastic method has been successful in maintaining the rigidity of bones in accordance with physical properties of the bones as seen in Figure 4.5(c).

The constrained elastic registration method shows a marginal improvement over the classic elastic registration technique, in terms of lung boundary and major fissure alignment. However, the overall performance of both the methods has been inferior in comparison to other methods that have participated in the challenge. The reason for this is that elastic registration framework has been unsuccessful in handling very large deformations and obtaining good overlap for the lungs. The solution for the elastic framework has not reached the desired deformation because of the internal strain of the elastic continuum. Thus, from these experiments it was observed that the elastic framework would be unsuccessful in registering large deformations, which motivated us to move to another framework to get an improved solution. The results of this study encourage us to try the fluid registration framework which has provided improved overlap for large deformations in experiments as shown in Chapter 3. Our ultimate goal is to register the volumes for the entire chest region including the ribs, spine and the liver and not just the lungs. Hence, limiting our evaluation of the methods for criteria only to the lungs would be unmerited. To achieve this, we also analyse the folding of the deformation outside the lungs and also the rigidity of the bones.

The objective of the additional constraints in the constrained elastic method is to preserve the topology and the rigidity. The rigidity of the bones is successfully preserved as seen in Figure 4.5. The linear movement of the bones promotes an accurate registration with a physically plausible deformation field. Thus, the rigidity constraint has successfully integrated into the elastic registration framework and also has demonstrated a good performance for

Scan Pair	Percentage of folding using classic elastic registration	Percentage of folding using constrained elastic registration	Percentage of folding using classic elastic registration (with extra padding around the image)	Percentage of folding using constrained elastic registration (with extra padding region around the image)
01	0.8787	0.8780	0.7916	**0.189**
07	0.4873	0.1186	0.3940	**0.0038**
14	0.1937	0.0538	0.1327	**0**
15	0.0160	0.0429	0.0012	**0.0016**
18	0.2547	0.2349	0.2340	**0.0051**

Table 4.3: Percentage of negative Jacobian values (within the lungs). Adding an extra padding region around the image reduces the number of negative Jacobian values obtained after registration using the constrained elastic method. The extra padding assists the topology preserving term in spreading the deformations and compensate for cropping of the images.

preserving bone rigidity.

The topology constraint has not performed well in reducing the percentage of negative Jacobians in comparison to its performance for the NCAT images shown in the previous chapter. One of the reasons identified for this limitation is the cropping of the images which causes problems in establishing anatomical correlation between points that might be present in the target image but not in the source image. The bounding box helps to reduce the amount of data but it also cuts through many important organs like the liver, ribs, mediastinum, etc. This reduces the space for the topology preserving term to evenly distribute the deformations.

The problem can be solved by adding a padding region around the image before registration. For periodic boundary condition used for our method, the zero padding increases the topological space of the image. This padding will provide added space for the topology preserving term to distribute the deformations and counter the problems created by the cropping of the images. In Table 4.3 we show the percentage of negative Jacobian values obtained after adding a padding region around the image. The padding is removed after registration during the comparison of the results. The results in Table 4.3 show that introducing an extra padding region around the image provides better results for the topology constraint

and improves its performance.

In conclusion, the EMPIRE 2010 challenge provided a platform to test and measure observe the strengths and the limitations of the constrained elastic framework with respect to the chest CT registration.

Chapter 5

Sliding Motion Modeling

In this chapter, we extend our proposed fluid registration framework to include a new strategy for modeling sliding motion. In section 5.1, we first motivate the need for incorporating sliding motion for lung boundaries. This is followed by a brief description of the overview of the literature in this area in section 5.2. In section 5.3, we introduce our proposed sliding motion model to allow for discontinuous movement along the lung boundaries. Section 5.4 briefly states the materials and methods used to validate the sliding motion model on three different mono-modal datasets. In section 5.5, we present and discuss the results of the experiments on three different sets of image data.

5.1 Introduction

A large number of motion estimation and image registration algorithms incorporate physical models to produce accurate motion fields. However, using these physical models is not sufficient to accurately estimate the complex motion of the lungs due to breathing. Common physical models apply a globally homogenous smoothing to the deformation fields over the entire image domain which can challenge the characteristics of breathing motion. Breathing motion consists of a simultaneous movement of different organs such as the lungs, liver, ribs and the diaphragm. A globally homogenous smoothing would compromise the physiological motion at the organ boundaries that slide along each other. During breathing, the lung and

the diaphragm slide against the rib cage and the atria creating discontinuities in the lung and chest wall motion, a motion which cannot be recovered using homogeneous regularization models. The global smoothing would cause registration errors near the boundary of the lungs and other sliding organs nearby.

The inclusion of a model to account for the breathing motion of the lungs is essential to achieve an accurate registration. Using a physiological model in the registration process would provide greater confidence for the clinician in terms of the registration results and could also be used as a tool for characterizing, evaluating and optimizing the image registration process. However, incorporating sliding motion to the registration framework would also increase its complexity and hence the computation time. A balance needs to be achieved between the complexity of the model and an acceptable error range for the lung motion.

To integrate physiologically motivated breathing motion into a registration algorithm, we need to understand the anatomy and the physiological motion of the lungs in greater detail. The lungs facilitate the exchange of the gases between blood and air. The two lungs are held within the thoracic cavity, separated from each other by the heart and the mediastinum. Lungs are highly elastic, light, porous and spongy organs with a smooth outer surface. The surface of the lungs is in contact with the surrounding structures via liquid filled spaces called the pleurae. The pleura is a delicate serous membrane arranged in form of a sac that surrounds the outer surface the lung. The outer pleura attached to the chest wall is known as the parietal pleura and the inner pleura attached to the lungs and the visceral tissue is known as the visceral pleura. The space between the parietal and visceral pleura is known as the pleural cavity, as shown in Figure 5.1. The pleura dictates the characteristics of the lung boundary motion during breathing.

The inhalation process requires an active participation of the respiration muscles. During inhalation, the diaphragm contracts forcing the abdomen to move inferiorly and anteriorly and to increase the volume of the chest cavity. This increase in volume of the thoracic cavity draws in air from the atmosphere due to the the pressure change. The intercostal muscles adjacent to the ribs also contract during inhalation causing an outward movement of the

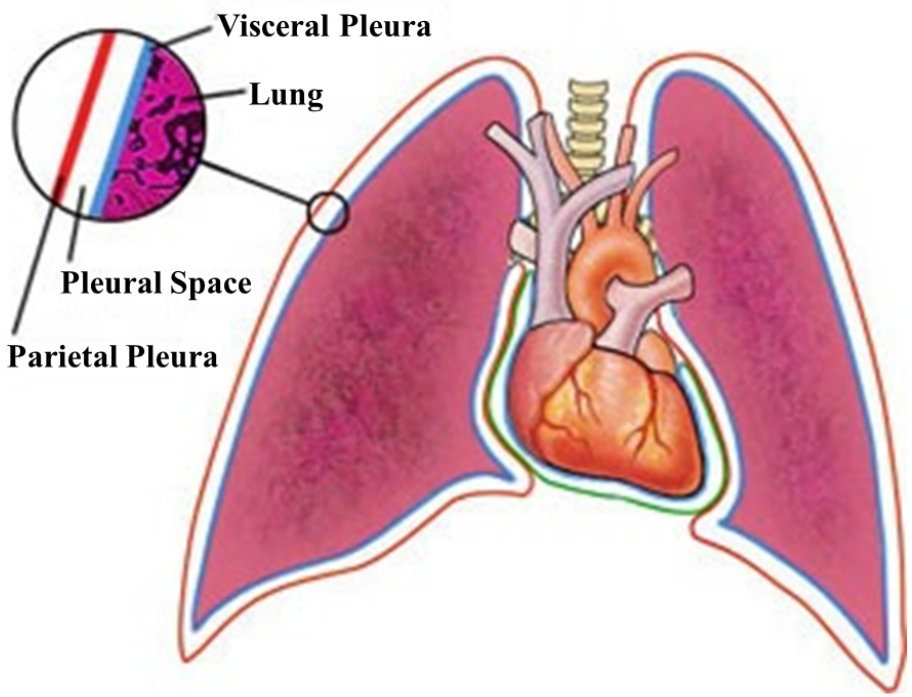

Figure 5.1: Anatomy of the lungs:pleura and the pleural space. Taken from [111]

thoracic cage. The pleural fluid lubricates the pleural surfaces and allows the layers of pleura to slide against each other. Thus, the motion of the lungs with respect to its surrounding organs and the chest wall is a form of sliding motion. Similarly, the lungs also slide against other organs during exhalation. An illustration of the motion vectors for inhalation is shown in Figure 5.2. The pleurae help to couple the movements of the chest wall with the movements of the lung during breathing.

Other organs like the liver also undergo sliding motion. In our study, we focus on the sliding motion of the lungs for two reasons : (a) It is the largest organ within the thorax and (b) modeling the sliding motion for the lungs is linked with the sliding motion of the neighboring organs like the liver and the ribs. Modeling the sliding motion of the lungs will also assist in improved alignment of the structures inside the lung as well.

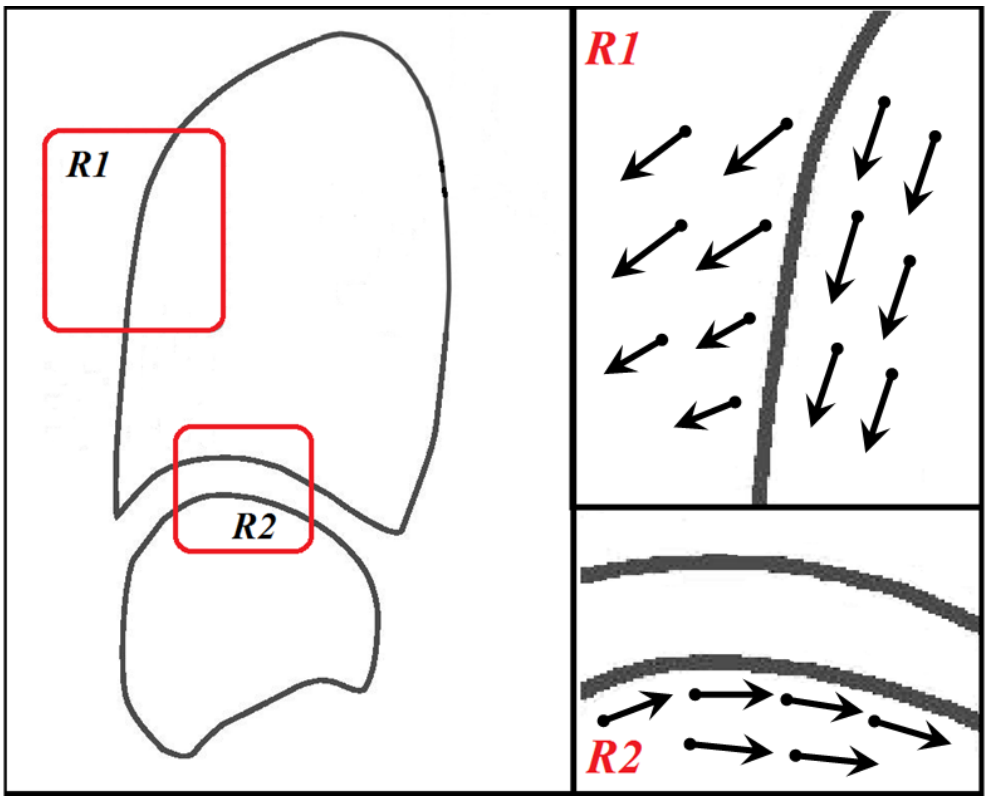

Figure 5.2: On the left hand side, the lung and liver are depicted schematically. A zoomed visual representation of the regions R1 and R2 is depicted with the motion vectors that occur during inhalation.

5.2 Research Background

There are a number of implicit and explicit approaches that have been used to model the sliding motion of the lungs. These efforts at preserving the discontinuity of the deformations between the organs can be classified into three classes. The first class of algorithms implicitly addresses the problem of sliding motion by using joint segmentation and registration. One of the methods proposed by Berg et al. [112] segments the lung to extract its surface information and then registers the iso-surfaces of the lungs. A dense motion field is then interpolated based on the registration of the lung iso-surfaces. Similarly, Vik et al. [113] proposed point based registration methods to implicitly simulate the dynamics of breathing motion. Other algorithms proposed by Al-Mayah et al. [114] and Werner et al. [115] use finite element modeling to obtain sliding motion of the lungs. These approaches however ignore the inner-organ information like the bronchial trees or vessel trees, which results in registration errors

for these structures. Another commonly pursued approach is to mask the background and then register the lungs as independent entities [84, 116]. This prevents the background deformations from affecting the registration of the lungs. If the background deformations are required, the registration algorithm is applied on a second inverted mask for the background and the resulting deformations are then combined. Registering the background and the organs on an individual basis and then combining the deformations may leave the possibility of creating gaps or folding along the boundary.

The second class of algorithms is based on edge-preserving, image restoration techniques. An anisotropic image driven regularizer was first proposed by the Nagel and Ekelmann [117]. This regularizer was designed to smooth the deformation fields along the edges of the defined object, but not across them. Since then, several other authors have tried to generalize the total variation regularizer for vector valued functions [118, 119, 120]. However, these set of algorithms, developed for computer vision with the exception of [120] can create gaps between the sliding objects which violates the preservation of image topology. These algorithms are thus not applicable for medical images where the sliding organs do not overlap each other and also do not produce gaps. Ruan et al. [121] further address this problem using a two-step approach, first by decomposing the vector fields into vector potentials and stream functions using Helmholtz-Hodge decomposition and then preserving the large shear values and penalizing any small ones caused by noise. One of the shortcomings of this method is the application of the slipping motion across the entire image domain rather than limiting it to the boundaries of the organs like the lungs. To fully evaluate the effects of this shortcoming on the deformation fields, a thorough investigation into the algorithm would be required.

The final class of algorithms uses direction dependent regularization. Initially introduced by Schmidt et al. [122] using a diffusion based framework, direction dependent regularization is achieved by decoupling the normal and tangential directed smoothing at the organ boundaries. Delmon et al. [123] proposed a direction dependent decomposition of the motion under a B-spline based registration framework. Pace et al. [124] uses a regularization term based on direction dependent anisotropic diffusion to preserve the discontinuities along the lung

boundaries. Similarly, Risser et al. [125] and Yin et al. [126] have incorporated the principle of direction dependent regularization in their respective transformation models. Later on, Schmidt et al. [127] further expanded on their earlier algorithm to incorporate automatic detection of discontinuities in the motion field and thus eliminate the dependence on a prior segmentation of the organ.

Direction dependent regularisation addresses the problem of sliding motion for the lungs [125, 122, 127] and it is also easily adaptable for the fluid registration framework. Keeping this in consideration, we are inspired by the direction dependent regularization and combine it into our proposed fluid registration framework, as developed in chapter 3 which includes a filter for rigidity preservation of the bones and an external force term for topology preservation. In addition to that, we are incorporating a sliding motion model and providing a comprehensive framework for chest image registration

5.3 Sliding Motion Model

The sliding motion of the lungs can be described as a discontinuous motion of the deformation at the lung boundaries. To achieve this sliding effect, the regularization step should allow homogenous smoothing of the deformations in most image regions, while permitting some discontinuities across the boundaries of the lungs. The direction dependent regularization step should aim to maintain the sliding effect by preserving the large shear along the lung boundaries. It should also avoid the creation of any gaps or folding of the deformation field during the registration process. As mentioned before, the direction dependent regularization scheme proposed by Schmidt et al. [122] decouples the normal and tangential deformations along the lung boundaries and then applies independent smoothing along the surfaces to estimate the sliding motion. In this section, we modify the fluid registration framework of Christensen et al. [56] to accommodate direction dependent regularization. Our work reverts to a similar principle of direction dependent regularization, however it decouples the external forces into normal and tangential force components along the lung boundary surface, *prior to solving*. We divide the image domain Ω into N sub domains based on the number of

sliding objects or organs present during the registration process. The sliding boundaries in these regions are denoted as $\partial\Omega$. The sliding motion conditions are imposed only along these boundary regions.

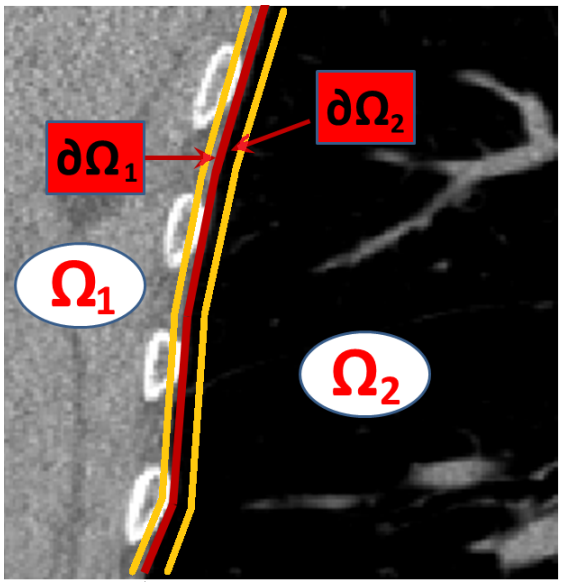

Figure 5.3: Subdivision of the registration domain Ω into Ω_1 (outside the lung) and Ω_2 (inside the lung). $\partial\Omega_1$ and $\partial\Omega_2$ represent the boundary regions of the lung where the sliding motion occurs.

To achieve this division of domains on lung CT images, the first step is to perform a segmentation of the sliding organs, i.e., the lungs on the source and the target images, S and T respectively. The segmented organs will serve as a prior to promote the discontinuous movements. The subdivision of the domains created by the segmentation of the lungs is represented in Figure 5.3. Having completed the segmentation, we generate a Euclidean distance map $D(\boldsymbol{x})$ from the lung boundaries. The distance map $D(\boldsymbol{x})$ serves a dual purpose. First, it is used to calculate the normal and tangential unit vectors with respect to the lung boundaries. Second, the distance maps are also used to select the volume of voxels that form the sliding boundary where the sliding motion model is applied.

The vector map for the normal direction to the lung boundary is obtained by taking the derivative of the Euclidean distance metric, $\boldsymbol{B}(\boldsymbol{x}) = dD/d\boldsymbol{x}$. The normal component for the external forces is calculated as:

$$\boldsymbol{F}_n(\boldsymbol{u}, \boldsymbol{x}, T, S) = \hat{\boldsymbol{B}}(\boldsymbol{x}) \left(\boldsymbol{B}(\boldsymbol{x}) \cdot \boldsymbol{F}(\boldsymbol{u}, \boldsymbol{x}, T, S)\right), \tag{5.1}$$

where $\hat{\boldsymbol{B}}(\boldsymbol{x}) = \boldsymbol{B}(\boldsymbol{x})/||\boldsymbol{B}(\boldsymbol{x})||$ is the unit normal vector in direction of the largest distance change, T and S are the target and source images, and $\boldsymbol{B} \cdot \boldsymbol{F}$ denotes the scalar product between the derivative of the distance map and the external force term. The scalar product projects the external force term $\boldsymbol{F}(\boldsymbol{u}, \boldsymbol{x}, T, S)$ into the direction normal to the boundary of the lungs, hence obtaining the normal component of the external force term $\boldsymbol{F}_n(\boldsymbol{u}, \boldsymbol{x}, T, S)$. The tangential component of the external forces is calculated by subtracting the normal component:

$$\boldsymbol{F}_t(\boldsymbol{u}, \boldsymbol{x}, T, S) = \boldsymbol{F}(\boldsymbol{u}, \boldsymbol{x}, T, S) - \boldsymbol{F}_n(\boldsymbol{u}, \boldsymbol{x}, T, S). \tag{5.2}$$

After obtaining the normal and tangential external force components along the sliding object boundary, we proceed by further splitting the process to be solved into two parts based on whether the location is inside ($\partial\Omega_2$) or outside ($\partial\Omega_1$) the boundary:

1. The normal force component $\boldsymbol{F}_n := \boldsymbol{F}_n(\boldsymbol{u}, \boldsymbol{x}, T, S)$ allows for inter-organ deformation, yielding a Navier-Stokes equation of the following form:

$$\mu\nabla^2\boldsymbol{v}_{n(\partial\Omega_1+\partial\Omega_2)} + (\mu+\lambda)\nabla(\nabla \cdot \boldsymbol{v}_{n(\partial\Omega_1+\partial\Omega_2)}) = \boldsymbol{F}_{n(\partial\Omega_1+\partial\Omega_2)}. \tag{5.3}$$

An example of the normal component $\boldsymbol{F}_n$ is illustrated by Figure 5.4(b) and the resultant normal velocity component $\boldsymbol{v}_n$ is shown in Figure 5.4(e).

2. The tangential force component $\boldsymbol{F}_t := \boldsymbol{F}_t(\boldsymbol{u}, \boldsymbol{x}, T, S)$ requires separate handling within the lungs and outside, i.e., $\partial\Omega_1$ and $\partial\Omega_2$. For this, we further split the domain into two: $\boldsymbol{F}_{t(\partial\Omega_1)}$ and $\boldsymbol{F}_{t(\partial\Omega_2)}$. This leads to two additional Navier-Stokes equations to calculate the velocities:

$$\mu\nabla^2\boldsymbol{v}_{t(\partial\Omega_1)} + (\mu+\lambda)\nabla(\nabla \cdot \boldsymbol{v}_{t(\partial\Omega_1)}) = \boldsymbol{F}_{t(\partial\Omega_1)}, \tag{5.4}$$

$$\mu\nabla^2\boldsymbol{v}_{t(\partial\Omega_2)} + (\mu+\lambda)\nabla(\nabla\cdot\boldsymbol{v}_{t(\partial\Omega_2)}) = \boldsymbol{F}_{t(\partial\Omega_2)}, \tag{5.5}$$

Solving equations (5.4) and (5.5) restricts any inter-organ deformations to be along the tangential directions. The illustration in Figure 5.4 shows the tangential force components $\boldsymbol{F}_{t(\partial\Omega_1)}$ and $\boldsymbol{F}_{t(\partial\Omega_2)}$ in Figure 5.4(c) and (d) and along with their velocity components $\boldsymbol{v}_{t(\partial\Omega_1)}$ and $\boldsymbol{v}_{t(\partial\Omega_2)}$ in Figure 5.4(f) and (g), respectively.

The final velocity fields for the lung boundary region (and corresponding deformations) are found by adding the respective terms, i.e., $\boldsymbol{v}_{(\partial\Omega_1+\partial\Omega_2)} = \boldsymbol{v}_{n(\partial\Omega_1+\partial\Omega_2)} + \boldsymbol{v}_{t(\partial\Omega_1)} + \boldsymbol{v}_{t(\partial\Omega_2)}$ after solving equations (5.3),(5.4) and (5.5) independently. The final velocity field $\boldsymbol{v}_{(\partial\Omega_1+\partial\Omega_2)}$ for the lung boundary region is illustrated in Figure 5.4(h). The sliding conditions are enforced only for a region within a certain width along the lung boundary, i.e., along the width of $\partial\Omega_1$ and $\partial\Omega_2$ combined. For the rest of the image, we do not decouple the velocities into normal or tangential components nor solve them independently. This equation is given as:

$$\mu\nabla^2\boldsymbol{v}_{(\Omega_1+\Omega_2-(\partial\Omega_1+\partial\Omega_2))} + (\mu+\lambda)\nabla(\nabla\cdot\boldsymbol{v}_{(\Omega_1+\Omega_2-(\partial\Omega_1+\partial\Omega_2))}) = \boldsymbol{F}_{(\Omega_1+\Omega_2-(\partial\Omega_1+\partial\Omega_2))}. \tag{5.6}$$

Hence the solution for the complete image domain is obtained as:

$$\boldsymbol{v}_{\Omega} = \boldsymbol{v}_{(\partial\Omega_1+\partial\Omega_2)} + \boldsymbol{v}_{(\Omega_1+\Omega_2-(\partial\Omega_1+\partial\Omega_2))}. \tag{5.7}$$

The remaining steps for the solution are the same as explained in Chapter 3.

5.3.1 Similarity Measure

Our earlier experiments have used sum of squared differences (SSD) as a similarity measure. The sum of squared differences (SSD) is one of the most common, mono-modality similarity measure used in medical imaging. However, SSD has poor performance in case of aligning small features and taking local neighborhood estimates. Other similarity measures commonly used for medical images include mutual information and cross correlation. Cross correlation

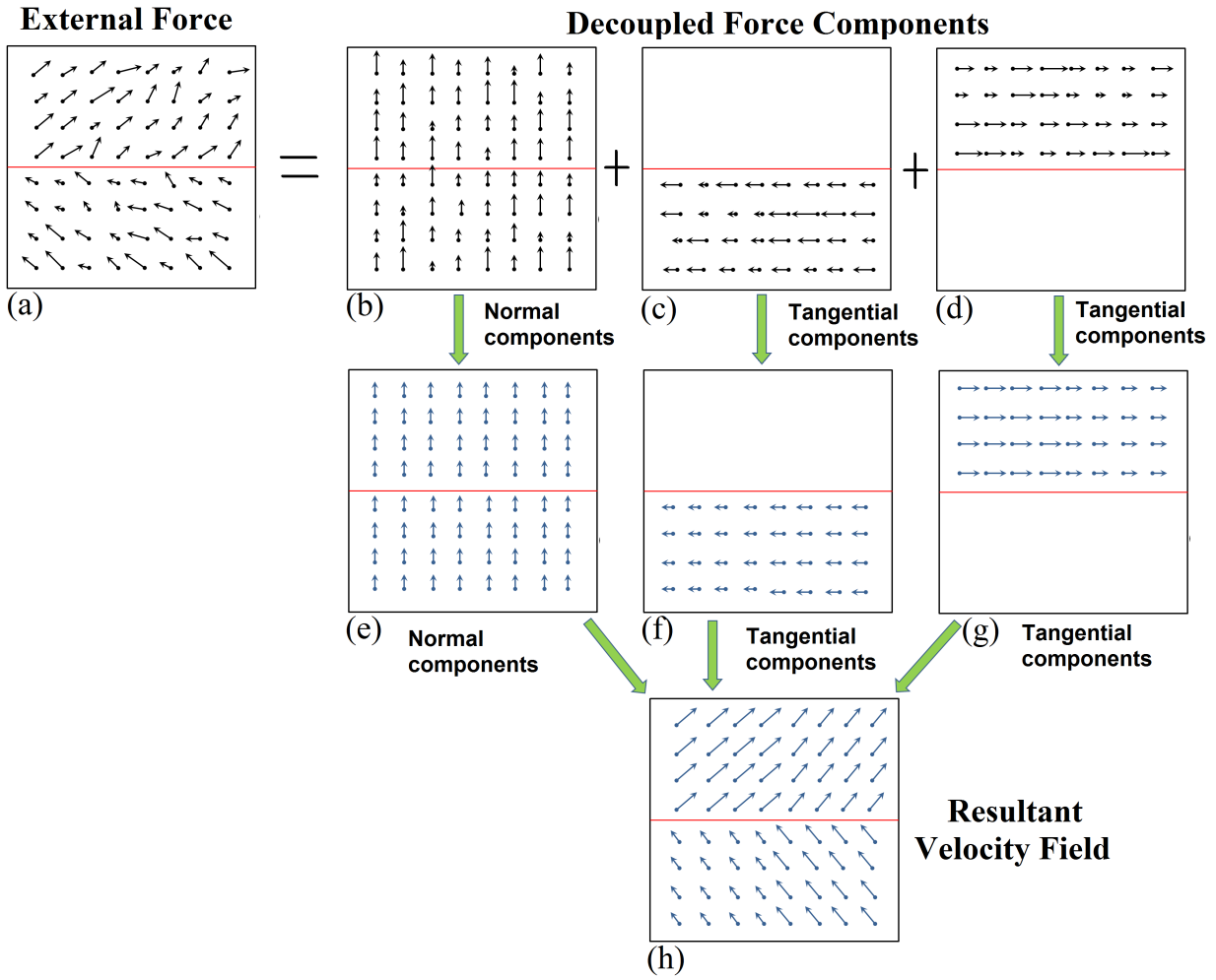

Figure 5.4: Sliding motion modeling: The initial force field is decomposed into tangential and normal force components (black arrow vectors). The forces are then solved individually to provide the respective velocity fields (blue arrow vectors). The final step consists of combining the individual velocities to obtain using superposition, yielding the final velocity field.

is found to be best suited for our problem as it is fast, easy to compute, and is invariant to changes to image intensity magnitude (lighting conditions) if calculated locally. Local cross correlation (LCC) is a measure of local affine dependency between the image intensities. The energy function of the LCC, calculated over a local region of Ω_R is defined as:

$$E_{LCC}(T,S) = \int_{\boldsymbol{x}\in\Omega_R} \frac{< \bar{T}, \bar{S} >^2}{< \bar{T}, \bar{T} >< \bar{S}, \bar{S} >} d\boldsymbol{x}, \tag{5.8}$$

where, $\bar{T} = T(\boldsymbol{x}) - \mu_T(\boldsymbol{x})$ and $\mu_T(\boldsymbol{x})$ is the local mean calculated for the target image using a local window centered at each position $\boldsymbol{x}$. Similarly, $\bar{S} = S(\boldsymbol{x}) - \mu_S(\boldsymbol{x})$ where $\mu_S(\boldsymbol{x})$ is the

local mean calculated for the source image. The operator <> represents the inner product taken over a small local window of the same size. The energy term of the similarity measure as shown in equation (5.8) is maximized using gradient descent to derive the external term. The external forces for LCC are:

$$\boldsymbol{F}_{LCC}(\boldsymbol{u}, \boldsymbol{x}, T, S) = \left(\frac{\sigma_{T,S}(\boldsymbol{u}, \boldsymbol{x})}{\sigma_S(\boldsymbol{u})} \frac{\bar{T}}{\sigma_T(\boldsymbol{x})} + \frac{\sigma_{T,S}(\boldsymbol{u}, \boldsymbol{x})^2}{\sigma_T(\boldsymbol{x})\sigma_S(\boldsymbol{u})} \frac{\bar{S}}{\sigma_S(\boldsymbol{u})} \right) \nabla S(\boldsymbol{u}), \tag{5.9}$$

where, $\sigma_T(\boldsymbol{x}) = T(\boldsymbol{x})^2 - (\mu_T)^2$ and $\sigma_S(\boldsymbol{u}) = S(\boldsymbol{u})^2 - (\mu_S)^2$ represent the individual local intensity variances of the target and transformed source image, respectively. Finally, $\sigma_{T,S}(\boldsymbol{u}, \boldsymbol{x}) = T(\boldsymbol{x})S(\boldsymbol{u}) - \mu_T\mu_S$ denotes the joint local variance of the target and transformed source images. Thus, the definition of the external force equation will depend only on local intensity statistics. As the deformations transform the source image into the target image, the external force term $\boldsymbol{F}_{LCC}$ is minimized when the images are perfectly aligned.

5.4 Materials and Methods

5.4.1 2D synthetic images

Initially, we evaluate our sliding motion strategy on synthetic 2D images. The source image I_S and the target image I_T are shown in Figure 5.6. This synthetic example demonstrates the proof of concept for the sliding motion model. The pair of images consists of two equally sized blocks of varying intensities. To mimic the sliding motion, the top block is translated by 5mm to the left and the bottom block is equally translated by 5mm to the right.

We first registered the images I_S and I_T using the classic fluid registration technique with Lamé parameters $\lambda = 0$ and $\mu = 100$. This selection of parameters, previously optimized in Chapter 3, corresponds to the deformation of a compressible object. The images were registered using a two-level multiresolution technique. The downsampled images are generated from each of the original 2D images. For the optimization step, the maximum number of iterations is set to 500, but the algorithm usually converges before, if there is no significant improvement of the cost between the iterations. The maximum admissible displacement in

one iteration is set to 0.5 times the voxel size. Sum of squared differences (SSD) is used as the cost function for registering the 2D images.

Same Lamé parameters settings and optimization conditions as mentioned in the earlier paragraph are also used for the fluid registration algorithm incorporating the sliding motion model. The image domain Ω of the source image I_S is subdivided into two sub domains Ω_1 and Ω_2. The lower block represents the domain Ω_1 and the upper block as Ω_2. The sliding motion boundary is limited to $2mm$ on both sides of the boundary of Ω_1.

5.4.2 POPI Dataset

In this chapter, we also validate the performance of our proposed fluid registration algorithm including all physiological constraints: sliding movement, and preservation of both rigid structures and topology. The proposed algorithm is validated on real CT datasets, the Point-validated Pixel-based Breathing Thorax (POPI) dataset that is publicly available [128]. The images were acquired on a 16 slice CT scanner. The movement of this belt provides an external signal for synchronization of the CT acquisition to the phase of the breathing cycle. The POPI model consists of ten CT lung volumes acquired at different breathing stages, providing several frames of an actual respiration cycle. Each CT slice has a resolution of $0.98mm \times 0.98mm$ and a thickness of $2mm$. The size of the images is $482 \times 360 \times 141$. Forty-one corresponding landmarks were defined by experts in all the image volumes, and serve as the gold standard for validating the registration accuracy. The masks for the segmented lungs are also provided. An example of the POPI dataset images for breathing stage 1 and 6 is shown in Figure 5.5 along with the difference image.

The proposed method was compared with the classic fluid registration method using LCC as a similarity measure. The external force term for the LCC is described in Section 5.3.1 by equation 5.9. All the breathing stages from 2 to 10 were registered to stage 1. A three level multiresolution approach is adopted to recover large deformations at coarser image resolutions and achieve more detailed alignment at higher resolutions. The Lamé parameters are set to $\lambda = 0$ and $\mu = 500$. The convergence criterion is based on the

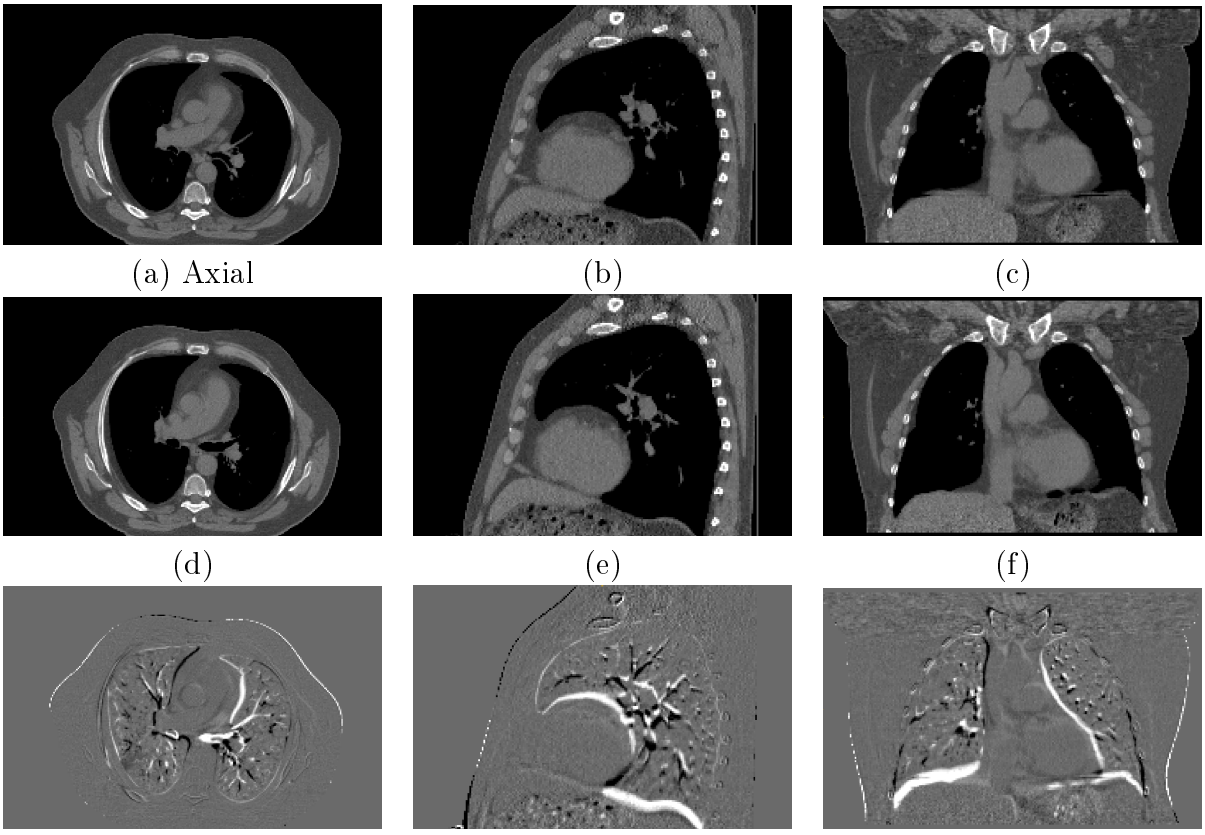

Figure 5.5: POPI dataset example: Three orthogonal views of the source image (stage 6 of breathing) are shown in first row (a-c) and the target image (stage 1 of breathing) is displayed in the second row (d-f) . The third row (g-i) displays the difference image between the source and the target image.

improvement in similarity measure (threshold at 5% improvement) compared to the earlier iteration. The maximum number of iterations was set to 300. For the proposed method the size of the local neighborhood window Ω_R used for both the rigidity constraint, and for LCC computation is chosen as $5mm \times 5mm \times 5mm$. To apply the rigidity constraint, the bones are thresholded between voxel intensities of 110 and 220 Hounsfield Units (HU). The sliding boundary conditions are set to $6mm$ inside and outside the lung boundary, i.e., a total width of $12mm$. LCC is also used as a similarity measure for the classic fluid registration.

5.4.3 EMPIRE10 Dataset

We also register the EMPIRE10 dataset to validate the benefit of our proposed method with sliding motion, rigidity preservation and topology preservation, in comparison to the classic

fluid registration. The EMPIRE dataset has been described in detail in Chapter 4. For this set of experiments, we work on the original uncropped images which contain a larger field of view than the images of the challenge which have been cropped. The uncropped images of the EMPIRE10 challenge have a large size of upto $512 \times 512 \times 500$ voxels. The registration is performed in the target image space with an initial rigid alignment of the images. The rigid alignment is achieved using SSD and the code was implemented using ITK [129]. The resultant deformation fields of the proposed method were also submitted to the EMPIRE challenge for evaluation and the results are included in section 5.5.3.2.

Image Pair no.	Lung overlap ratio (DSC) without registration	μ
1	0.6459	250
2	0.8901	450
3	0.8785	450
4	0.8808	450
5	0.8945	450
6	0.9659	500
7	0.7842	350
8	0.8720	450
9	0.7670	350
10	0.8307	400
11	0.8478	400
12	0.9229	500
13	0.9395	500
14	0.7372	300
15	0.8211	400
16	0.7034	300
17	0.9405	500
18	0.7316	300
19	0.8655	450
20	0.7549	350
21	0.6251	250
22	0.8767	450
23	0.8903	450
24	0.8931	450
25	0.8067	400
26	0.9651	500
27	0.8697	450
28	0.7443	300
29	0.8759	450
30	0.7564	350

Table 5.1: Lamé values used for the EMPIRE10 dataset and the overlap ratios of the lung (DSC) without registration. The overlap ratios are helpful in parameter selection as they provide an approximate estimate on whether the registration step needs to recover larger deformations or smaller ones.

Non-rigid alignment is achieved using LCC as a similarity measure for the classic fluid method as well as for the proposed method. We have used varying values of Lamé parameters for the different image pairs depending on the magnitude of the deformations. Generally a lower value of Lamé parameter μ is selected to recover larger deformations and higher values

of μ are used to get improved stability for smaller deformations. Table 5.1 shows the various values selected for the registration of the 30 image pairs. The value of λ is set to zero for the registration. Four levels of resolution were used, 200 iterations were performed for coarser levels while 50 iterations were performed at the finest level. The code was implemented within MATLAB. Thresholding of the bones is applied to segment the bones from the image with different thresholding values being used for each image pair. The same parameters are used to impose the rigidity constraints and the sliding motion model as the POPI dataset.

5.5 Results

5.5.1 Results on Synthetic 2D Data

For the synthetic example at hand, the overlap of the blocks is 0.9923 for the classic fluid method, and 0.9929 using additional sliding modeling. However, a closer inspection of the magnitude of the estimated horizontal deformation field in Figure 5.6(c) reveals that the classic fluid method has generated higher deformations at the corners and at boundaries of the blocks. The classic fluid transformation model indiscriminately smoothes the tangential motion of the blocks across the boundaries which prevents the recovery of sliding motion. In contrast, the new fluid method, which is explicitly modeling sliding motion has provided a more uniform push along both blocks in the respective directions while preserving the sliding motion at the block boundaries, as can be seen in Figure 5.6(f). We also estimated the mean target registration error (TRE) in the horizontal displacement of all pixels for both blocks. TRE is defined as the distance between corresponding points after registration. For fluid registration, the average TRE is $0.94mm$ while for the fluid method including sliding, the TRE is much lower at $0.32mm$. This clearly demonstrates the improved performance of the proposed fluid method using sliding motion.

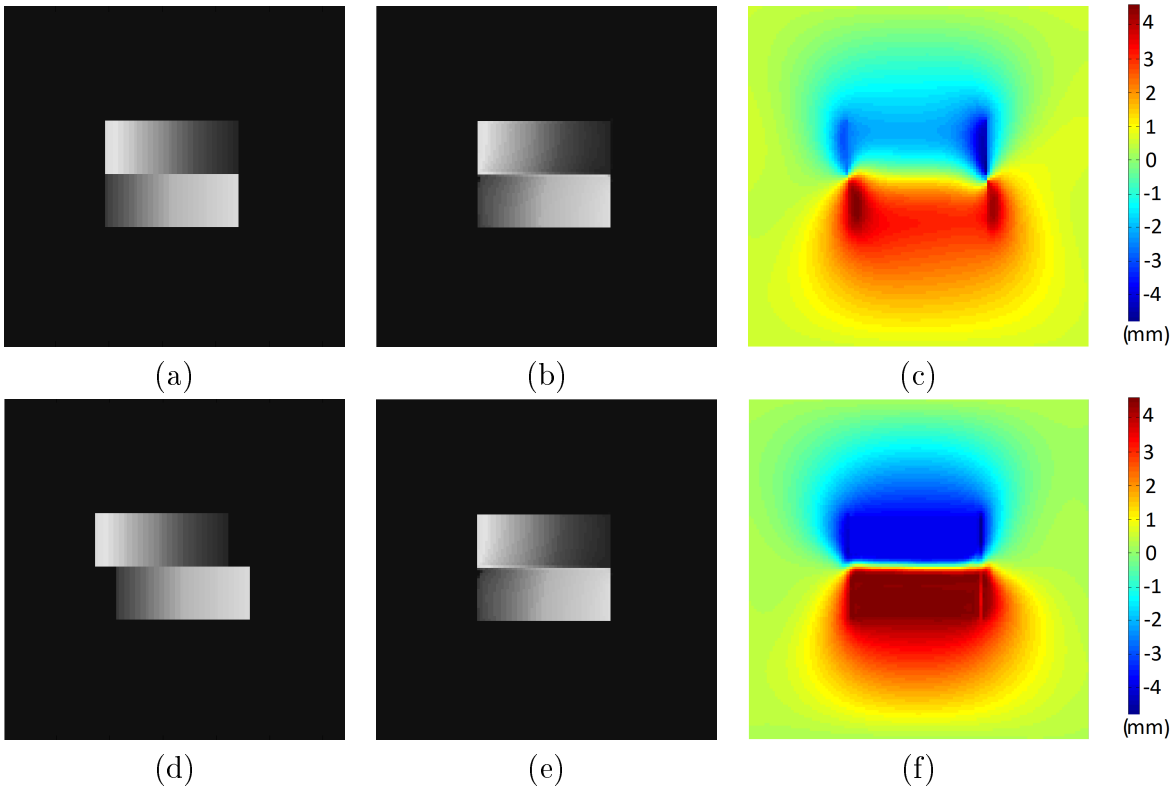

Figure 5.6: 2D synthetic example: (a) Target image. (d) Source image. Deformed source using : (b) the classic fluid method and, (e) the fluid method using sliding motion (proposed method). Horizontal component of the deformation field using: (c) the classic fluid method, and (f) the proposed method.

5.5.2 Results for the POPI Dataset

In Figure 5.7, we show the result of the proposed fluid registration method incorporating sliding motion, rigidity preservation and topology preservation versus the classic fluid registration technique. Since the proposed fluid registration method provides an accurate directional push to the lung boundaries using the physiological constraints, we observe that the proposed method is better able to align the organs even for larger deformations between stage 1 and stage 6 of the breathing cycle. The classic fluid registration technique has failed in the complete alignment of lung boundaries as well as the internal vessel trees.

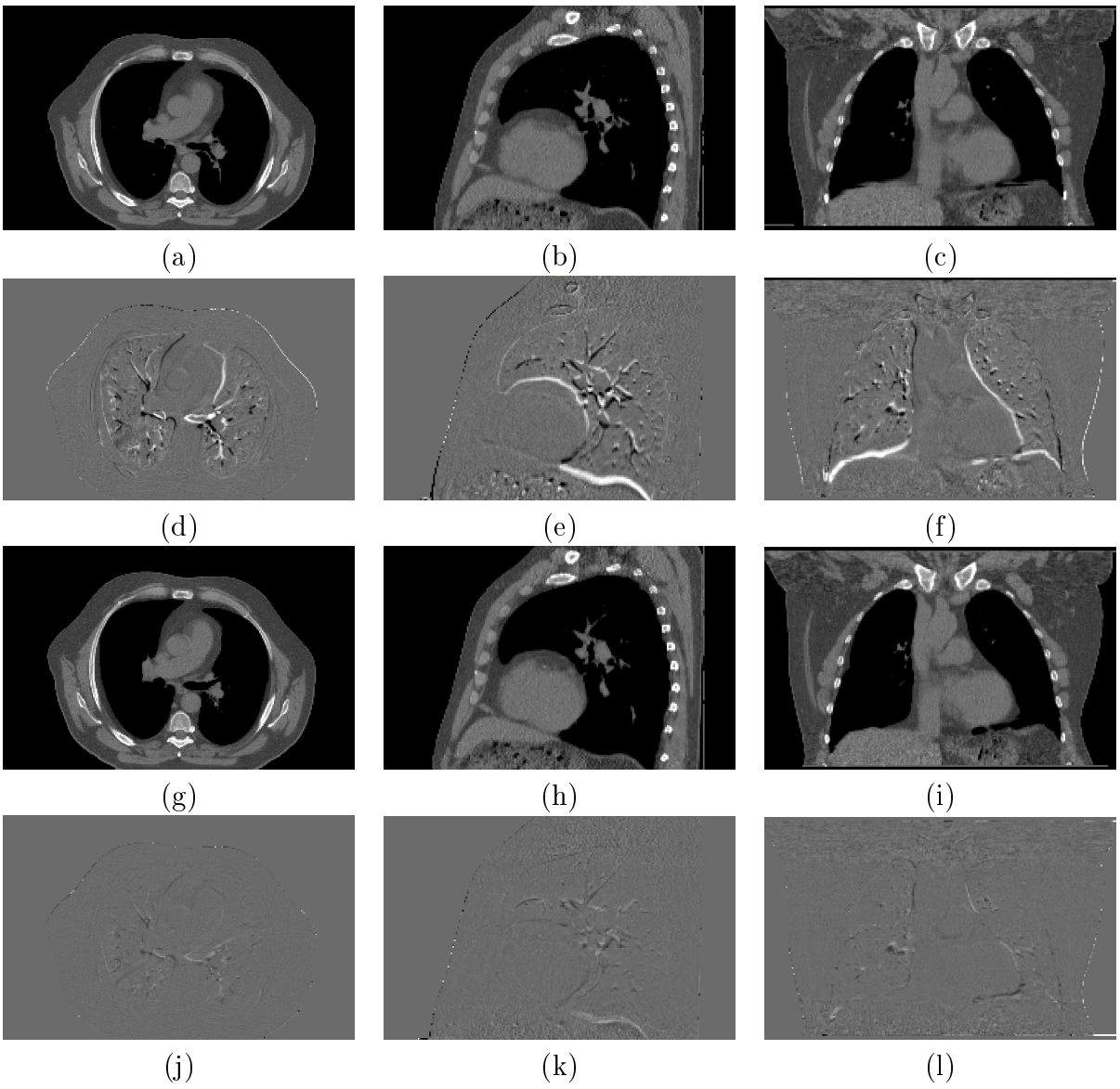

Figure 5.7: Registration results for stage 6 to stage 1 registration. The first row (a-c) shows the three orthogonal views of the deformed images using classic fluid registration technique. The second row (d-f) displaying the difference image highlights that the classic fluid registration has failed to completely and accurately register the images. The third row (g-i) and fourth row (j-l) displays the deformed image and the difference image results using the proposed registration technique, composed of sliding motion model, bone rigidity preservation and topology preservation.

A quantitative validation of the method is performed by calculating the mean TRE for the 41 landmarks, after registering each dataset to the first one. The accuracy of the results is determined to be successful if the TRE after the registration process becomes lower than the voxel size. Figure 5.8 shows that the proposed method has a superior performance compared to the classic fluid registration technique, with an overall lower mean TRE. The TRE for

phase 1-2 and phase 1-10 breathing, show poor performance in image alignment. This is mainly due to the registration being driven by the larger structures like lung boundaries and other soft tissues which also leads to the movement of smaller structures and thus increase the TRE. The classic fluid method has TRE greater than the slice thickness of $2mm$ for breathing phases of 1-5, 1-6 and 1-7. The registration of these breathing phases by the classic fluid method could be considered as a failure as the TRE error is greater than the voxel size (a common measure of registration failure). It is also observed that the mean TRE remains almost constant and has a lower TRE value when using the proposed method (average TRE = $1.37\pm$ $0.11mm$), compared to the classic fluid method, whose accuracy varies depending on the breathing phases that are being registered (average TRE = $1.82 \pm 0.3mm$).

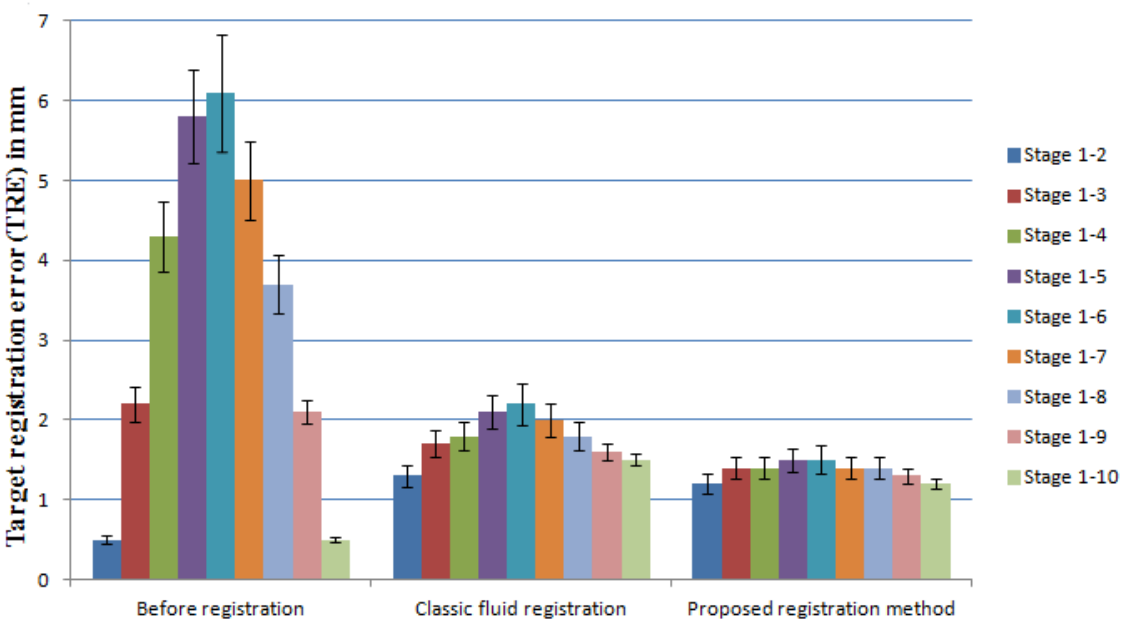

Figure 5.8: Landmark target registration error results for POPI dataset, before registration, after classic fluid registration and after proposed method using sliding motion and preservation of rigid structures and topology.

The lung overlap ratios are shown in Figure 5.9. The proposed method has a better overlap ratio over the entire dataset (with the exception of registration of phase 1-10, where the overlap without registration is already very high) in comparison with the classic fluid registration technique. For the proposed method the average overlap was 0.993 ± 0.002 while for classic fluid registration it was 0.984 ± 0.0086.

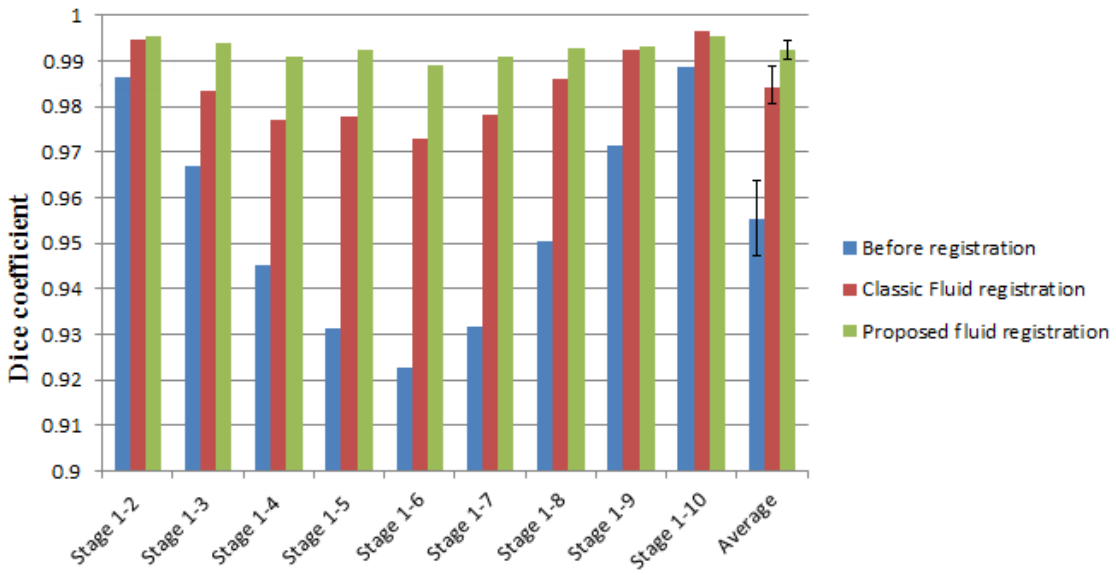

Figure 5.9: Lung overlap ratio for POPI dataset, before registration, after classic fluid registration and after proposed method incorporating sliding motion and preservation of rigid structures and topology.

A qualitative validation of the proposed registration technique is displayed in Figure 5.10. As illustrated in Figure 5.10(b), the deformation vectors for classic fluid registration result are smoothed out along the lung boundary. The discontinuous movement is lost in the process which ultimately leads to an inaccurate registration. The proposed fluid registration technique is able to preserve some of the discontinuous movement of the lungs due to the sliding motion model. Thus, the proposed method provides a physically and physiologically plausible deformation field in response to the breathing motion.

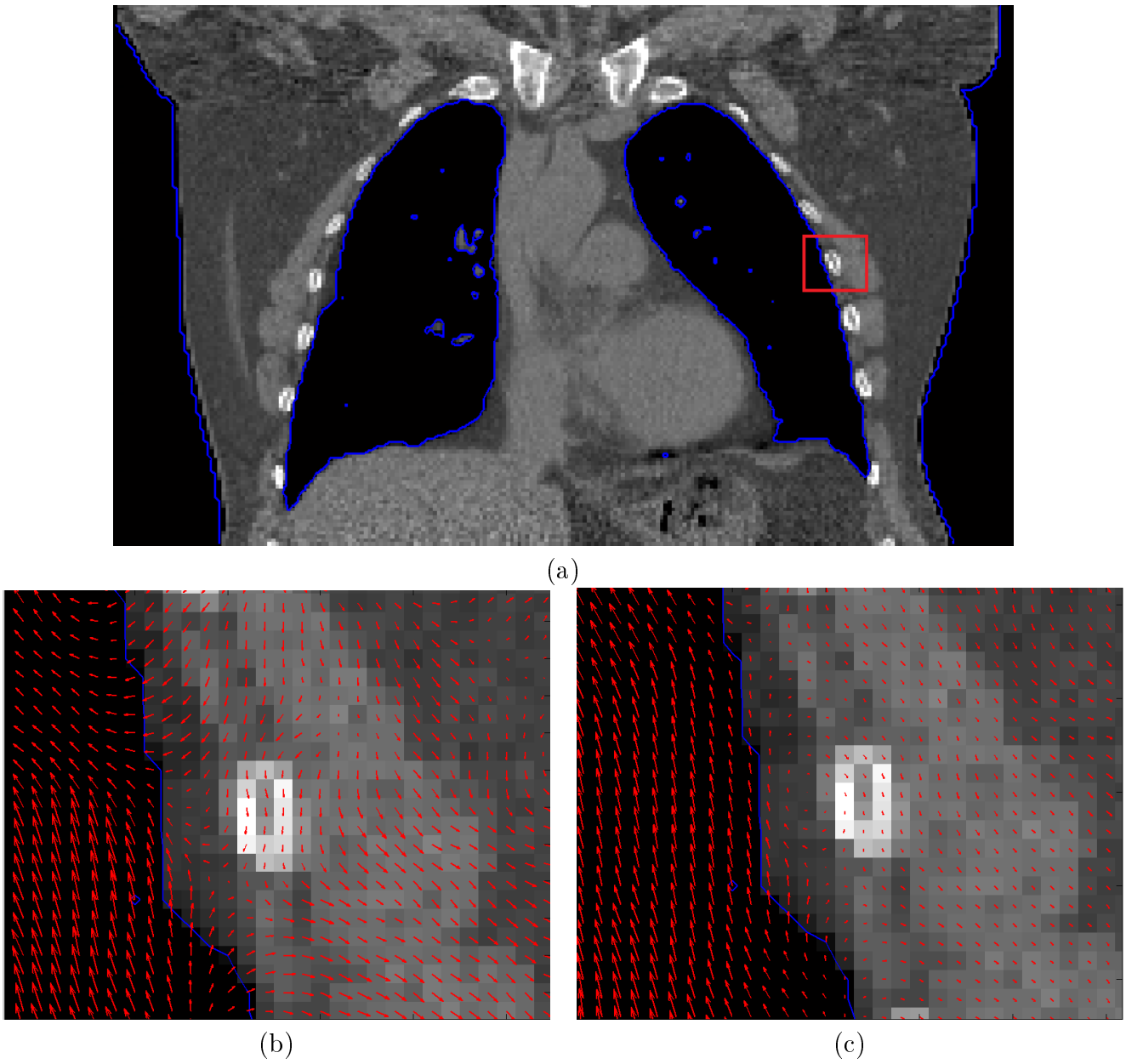

(a)

(b) (c)

Figure 5.10: Registration results for Stage 1-6. Top image (a) Target image with the lung boundaries marked in blue. The red box defines the region for which the deformation vectors are zoomed in. (b) Deformation vectors for results using classic fluid registration (c) Deformation vectors for results using proposed method.

We also assess the rigidity of the bones by investigating the Jacobian values in the bone regions, i.e., we estimate any change in volume of the bones. For classic fluid registration, a large variation in the Jacobian values of the bones is observed. The average Jacobian value of the bones using the classic fluid registration technique is 0.963 ± 0.03. This proves that the classic fluid method allowed a physically implausible shrinking of the bones during

registration and may also cause equally invalid deformations. The proposed method has an average Jacobian value of 0.99 ± 0.01 for the bones which shows that the rigidity preservation term has been successful in preserving the volume of the bones, which is an important condition for preserving their rigidity.

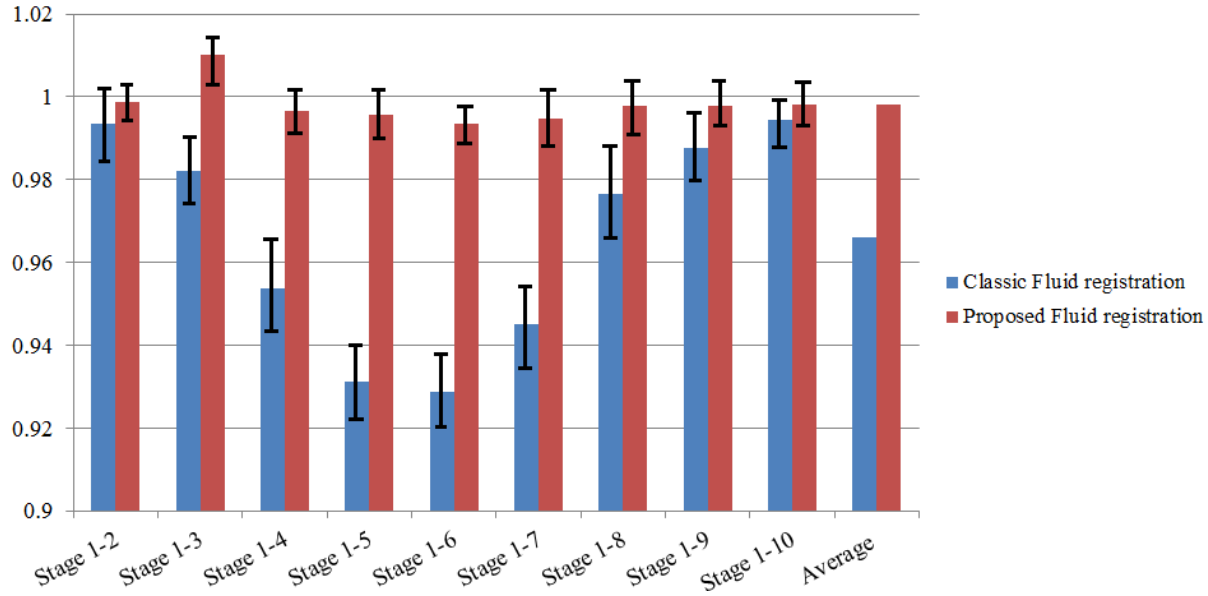

Figure 5.11: Jacobian values of the bones for the POPI dataset, after classic fluid registration and proposed method incorporating sliding motion and preservation of rigid structures and topology. The results show that the proposed method has an improved performance in keeping the Jacobian values of the bones close to 1 .

We calculate the percentage of negative Jacobian values across the image domain to assess the quality of the deformation field. The proposed method has been able to preserve the topology and has very few voxels that undergo folding as shown in Table 5.2. The classic fluid registration without any topology preservation term has been unsuccessful in preserving the topology of the image and has a very high percentage of negative values.

Registration stages of POPI dataset	Classic Fluid registration	Proposed Fluid registration
Stage 1-2	0%	0%
Stage 1-3	0.234%	0%
Stage 1-4	0.511%	0.001%
Stage 1-5	0.798%	0.002%
Stage 1-6	1.134%	0.005%
Stage 1-7	0.876%	0.003%
Stage 1-8	0.525%	0.001%
Stage 1-9	0.139%	0%
Stage 1-10	0.023%	0%

Table 5.2: Percentage of negative Jacobian values for the entire image domain, after classic fluid registration and proposed method incorporating the sliding motion and preservation of rigid structures and topology.

5.5.3 Results on EMPIRE Dataset

5.5.3.1 Comparison with Classic Fluid Registration

To validate the new proposed method for the EMPIRE dataset, we compare the overlap ratios of the lungs using the proposed method with the classic fluid technique. As seen in Figure 5.12, the performance of the proposed technique has shown better overlaps for most image pairs in comparison to the classic fluid technique. The image pair for subjects 7, 23 and 26 were the only examples where the classic fluid technique performed slightly better than the proposed technique. The average overlap ratio of the lungs without registration has been 0.833 ± 0.0734, while after classic fluid registration it has increased to 0.932 ± 0.042. For the proposed fluid method the average overlap ratio is higher at 0.947 ± 0.021.

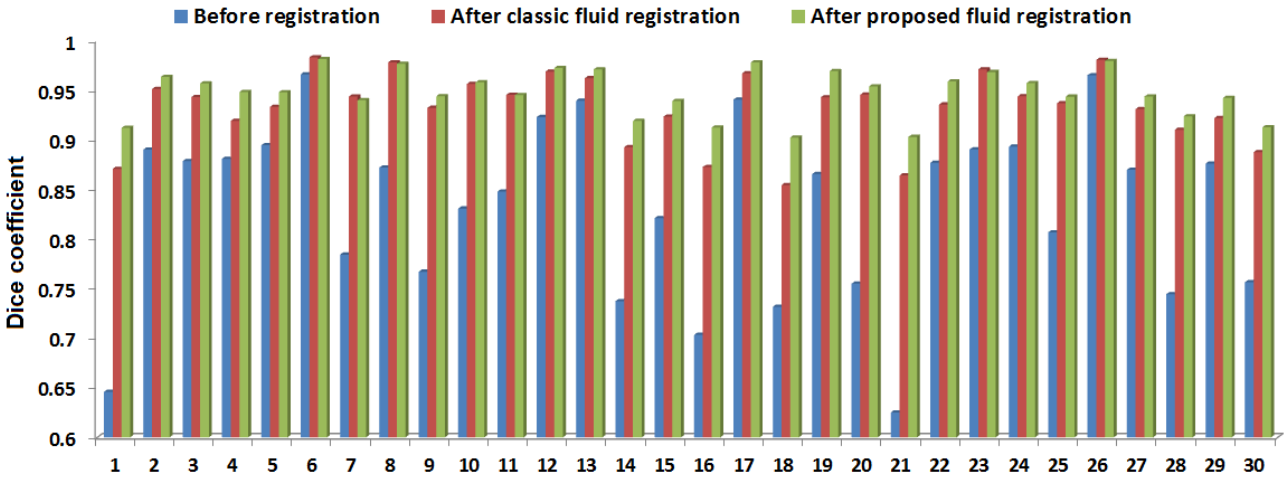

Figure 5.12: Lung overlap ratio for EMPIRE2010 dataset, before registration, after classic fluid registration and proposed method incorporating sliding motion and preservation of rigid structures and topology.

To further qualitatively analyze the deformation field, in Figure 5.13, we show the amplitude map of the deformation field for the classic fluid and the proposed technique. We have selected the example of scan pair number 7 as it requires the recovery of a large deformation. The magnitude map for the proposed method shows that it has been successful in preserving the deformations around the lung boundaries and preserve the discontinuous movement. The classic fluid method has applied a homogeneous smoothing which smoothes out the discontinuous movement.

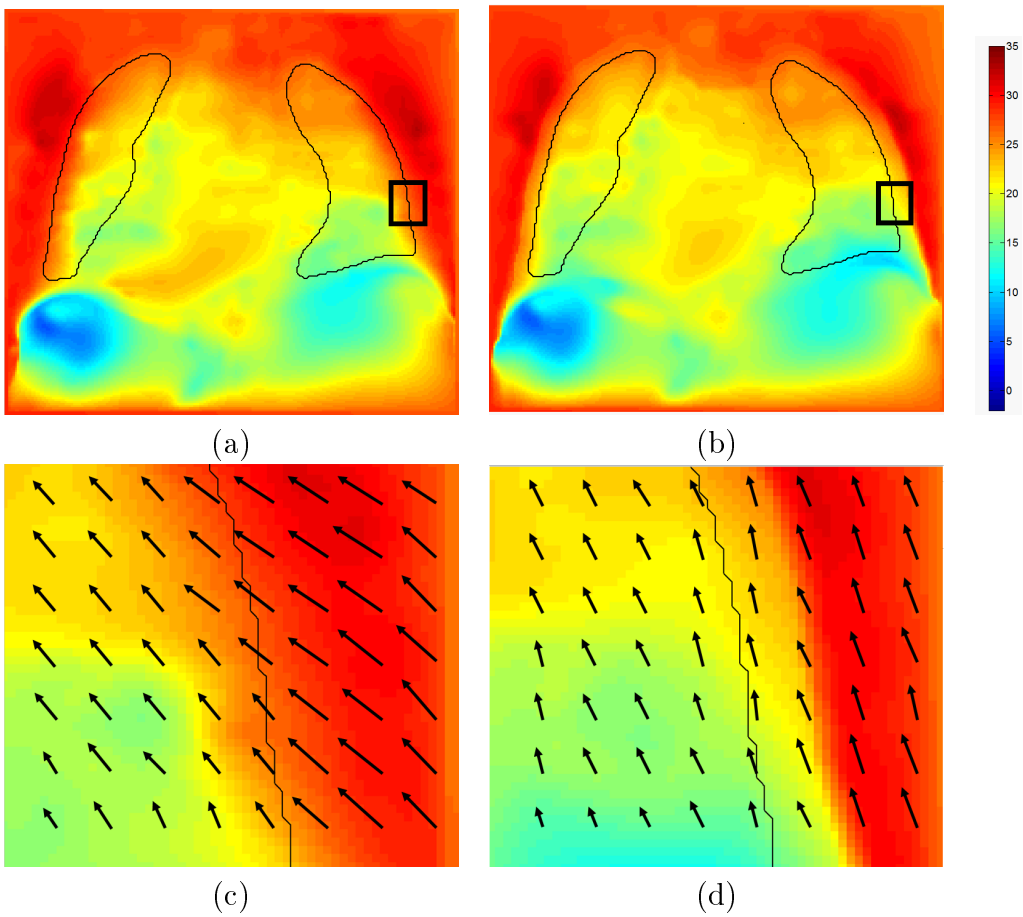

Figure 5.13: Amplitude of deformations estimated on EMPIRE data (patient 7) (a) Classic fluid method (b) Proposed method incorporating sliding motion, rigidity preservation and topology preservation. The black curves represent the lung boundaries and black box highlights the ROI. 2D projection of the ROI with deformation vectors (c) Classic fluid method and (d) Proposed method.

5.5.3.2 EMPIRE10 Challenge Evaluation Results

The deformation fields of the proposed method were submitted to the EMPIRE challenge organizers for evaluation. Our proposed method has ranked 26th out of the 30 methods that have been submitted for the challenge till March 2013.

From the results shown in Table 5.3 one can clearly see that the proposed fluid method is an major improvement over the results of classic elastic registration and constrained elastic method which are presented in Chapter 4. The proposed method performs comparatively well in almost all cases with a small to medium amount of breathing motion. As per the

	Lung Boundaries		Fissures		Landmarks		Singularities	
Scan pair	**Score**	**Rank**	**Score**	**Rank**	**Score**	**Rank**	**Score**	**Rank**
01	0.4613	26	16.8776	28	22.2557	27	0.1698	26
02	0.0005	24	0.0335	26	2.9261	26	0	13
03	0	17	0.7062	27	1.7910	27	0	13
04	0.0119	28	0	14	3.9394	25	0	13
05	0	12	8.9846	28	2.7643	2	0	12
06	0	14	0.0461	27	0.9309	25	0	14
07	0.0668	23	6.8832	26	14.2339	2	0	10
08	0	10	2.9011	23	2.8536	23	0	13
09	0.0006	21	0.0256	24	2.03964	2	0	12
10	0.0216	27	0.0005	26	5.5565	25	0	12
11	0.1708	26	7.8172	27	3.4239	26	0	12
12	0	11	0.0418	26	1.4050	26	0	14
13	0.0011	19	1.8914	28	3.5488	27	0	12
14	0.4905	28	7.6040	23	10.0625	25	0.0003	17
15	0.0012	23	2.2573	26	2.7108	26	0	13
16	0.0942	27	5.8362	28	5.5883	28	0	13
17	0	8	0.1763	29	2.3719	27	0	13
18	0.0254	19	8.6480	26	12.6439	27	0	10
19	0	14	0.2181	28	2.3921	27	0	13
20	0.0008	15	7.4106	26	14.1824	27	0.0408	24
21	0.9760	25	5.7780	24	50.9711	30	1.6195	26
22	0.0038	14	0.5107	26	1.7366	24	0	12
23	0.00348	17	7.966	27	3.5022	26	0	13
24	0.0076	28	0	11	3.1836	27	0	12
25	0	24	0.0008	26	1.1438	27	0	13
26	0	8	0	1	1.2925	25	0	14
27	0	19	0.3096	25	1.4405	26	0	12
28	0.5978	27	17.1052	28	12.0399	27	0	11
29	0.0015	23	0.0003	23	3.8539	27	0	12
30	0	13	0.0011	23	1.1145	26	0	13
Average	0.1690	20	3.6678	24	6.5967	26	0	14

Table 5.3: Results per each scan pair, per category and overall. Rankings and placement are from a total of 30 competing algorithms. Average ranking overall: 26th.

results of the EMPIRE challenge evaluation, the strengths of the proposed method lies in accurate alignment of the lung boundaries (Lung score < 0.1 for most cases) and having the least amount of singularities (Zero negative Jacobians in most cases). This implies that the fluid transformation model is able to recover large deformations of the lungs while the topology preserving constraint is able to prevent the folding of the deformation field in most cases.

The most important drawback of our method still remains the accurate alignment of landmarks and fissures. This error mainly occurs in image pairs 1, 14, 18, 21 and 28. These image pairs show very large differences in the breathing cycle which leads to rather different appearances for smaller vessels in both the images. Some of the vessels also vanish in the exhaled data set due to the limitations in spatial resolution. Therefore, the LCC similarity measure was not able to align these landmarks accurately and caused a drop in our performance. Another factor that has contributed to the underperformance of our proposed method is the low contrast of the structures inside the lung.

5.6 Conclusion

We have presented the proposed fluid method, combining rigidity preservation and topology preservation terms with a novel, physiologically motivated sliding motion model that addresses the problem of discontinuous movements at the boundaries. The proposed method demonstrated on a synthetic data set, and further has been validated on the POPI and EMPIRE datasets. Results show that the proposed registration technique is robust for different types of data with small and large deformations. The proposed technique has also shown to have better overlap ratios than the classic fluid registration technique. In the next chapter we look at the application of the proposed algorithm to register the diagnostic contrast enhanced CT and the whole body CT.

Chapter 6

Registration of Contrast Enhanced Diagnostic CT and PET Images

6.1 Introduction

Lung cancer remains a challenging disease to stage accurately because it manifests itself as a peripheral lung nodule or mass which presents problems for proper diagnosis. Contrast-enhanced diagnostic CT (d-CT) is the most widely used imaging modality for identifying pulmonary abnormalities [130]. The d-CT scans provide good contrast to detect small and large primary tumours for lung cancer, as well as information regarding their shape, size and the exact location. The injected contrast agent also helps to differentiate blood vessels from soft tissues in order to identify any enlarged lymph nodes. The diagnostic value of d-CT for depicting accurate structural anatomy is highly appreciated, but it is less useful for differentiating between benign and malignant tumours.

PET lung scans are generally used for tumour staging. They are often acquired after the d-CT scans to differentiate between any benign and malignant tumours. PET scans are helpful in finding the spread of the cancer to regional lymph nodes and detecting distant metastatic tumours. A non-contrast enhanced attenuation correction CT (AC-CT) is acquired alongside the PET scan to correct for the attenuation of the gamma rays. The attenuation corrected PET image is then fused with the AC-CT image to provide metabolic

and anatomical information jointly in one image as shown in Figure 6.1(a). The PET and AC-CT images are intrinsically spatially registered, eliminating the need for registration.

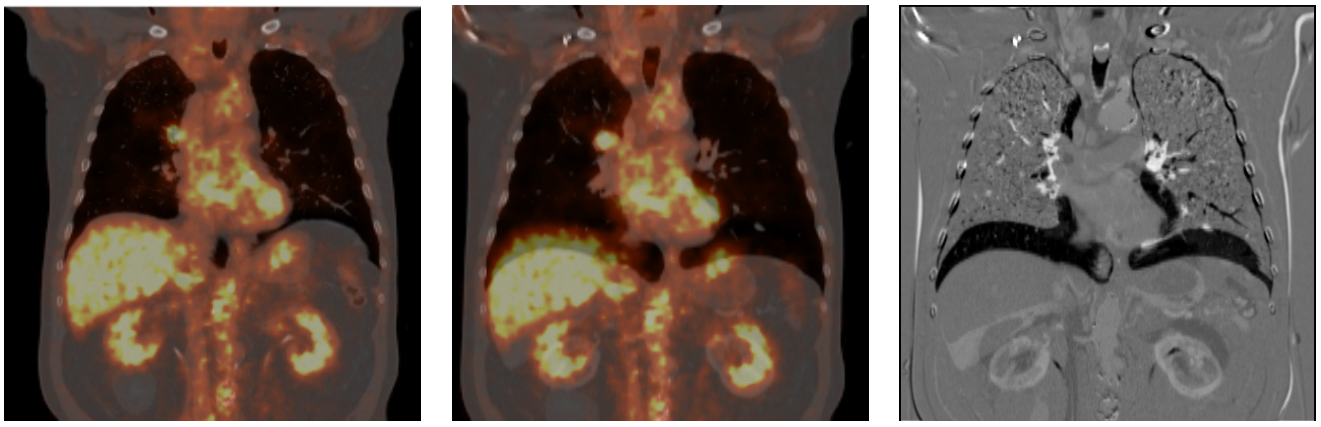

(a) (b) (c)

Figure 6.1: (a) Fused PET/ AC-CT image (b) Fused PET/Diagnostic CT (contrast-enhanced) image without registration (c) Difference image between AC-CT and Diagnostic CT.

Fusing the d-CT and the attenuation corrected PET image may provide better aid in accurate disease staging. However, the PET and the d-CT image cannot be fused directly as they are not spatially aligned, and a direct fusion will lead to erroneous results as shown in Figure 6.1(b). Before the advent of combined PET/CT scanners a great deal of research was pursued in the registration of non-contrast CT and PET volumes. One of the first attempts of direct PET to CT image registration was made by Tai et al. [131] using an elastic registration framework with cross correlation as the similarity measure. Later on, Shekar et al. [132] also used the elastic registration framework but with normalized mutual information as the similarity criterion. A different solution was provided by Mattes et al. [133] which aimed at registering the PET data with CT using free form deformations. Camara et al. [134] tried to register the images using a two step approach: The first step non-linearly registered the segmented lungs from the PET and CT images and then used them as prior knowledge for the next step. The second step applied intensity based registration to align the non-segmented regions. Non-rigid deformations were modeled in both the registration stages using free-form deformations. A landmark based approach was also introduced by Chambon et al. [135] to produce plausible deformations, but lacked thorough validation. Morena et al. [136] provided

a novel method of combining a breathing model with image registration. However, their method requires lung segmentation on the PET images, which is done manually and prone to human error. A thin plate splines approach with mutual information was also proposed by Slomka et al. [137]. Most of the methods listed above have been validated only qualitatively, making it difficult to judge the registration performance. For some methods, landmarks were selected on the PET image to validate the registration method quantitatively[133]. These landmarks on PET image are however unreliable as they are not derived from anatomical information. The success of these direct PET-CT registration approaches has also been constrained by the use of an appropriate cost function, the breathing protocol used during image acquisition, respiratory gating and the resolution of the PET image. Morever, these methods have been defined and validated for registration of PET volumes with non-contrast enhanced CT images. The same algorithms might not be able to establish an accurate spatial relationship if the non-contrast CT is replaced with a contrast-enhanced CT image such as the d-CT. The primary reason for this shortcoming is that establishing a direct similarity relationship between d-CT and PET image is a difficult task. As mentioned in Chapter 1, registering the PET and d-CT images directly can be misleading as they do not belong to the same modality and they are acquired at different phases of breathing.

A solution which we propose to this problem is to register the AC-CT with the d-CT and then use the deformations to warp the PET image so that it can be fused with d-CT. The work-flow to fuse the PET and d-CT is shown in Figure 6.2. Fusion is defined as the process of combining information from two or more images. In medical imaging, image fusion is achieved by overlaying the images over each other and controlling transparency of the images. There is no published literature on work that studies the registration of contrast enhanced thoracic d-CT with non-contrast enhanced AC-CT. There is some work on the registration of contrast enhanced CT for perfusion studies of liver [138, 139, 140, 141]. Similarly, there are algorithms designed for registering the perfusion cardiac images [142, 143] but none of them relate to the problems faced during the registration of thoracic CT images.

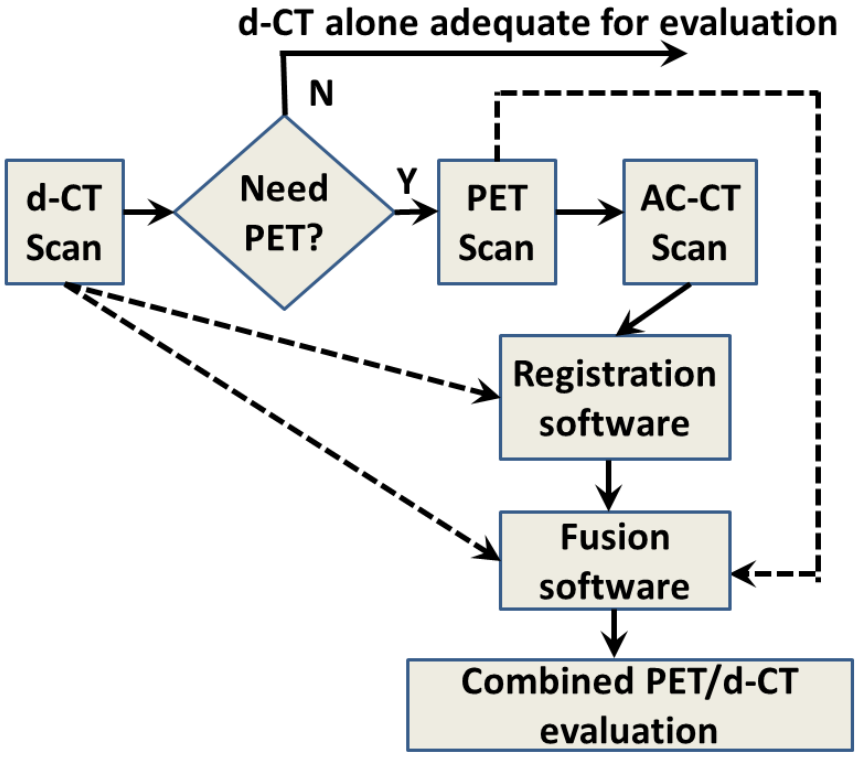

Figure 6.2: Scheme for fusing PET with d-CT.

6.2 Materials and Methods

We demonstrate our proposed the PET/d-CT fusion scheme using our previously presented registration method that comprises sliding motion, rigidity and topology preservation, on clinical patient datasets. The results of the proposed registration technique are compared with classic fluid registration.

Diagnostic CT volumes of ten patients were acquired during full inspiration after an intravenous injection of iodinated contrast agent, while the whole body PET/CT volumes were acquired during normal breathing.The PET and the AC-CT images were acquired on the same scanner. The slice thickness of the diagnostic CT scan is $3mm$, and $2mm$ for the AC-CT scan, with an in-plane resolution between $0.6mm \times 0.6mm$ and $0.8mm \times 0.8mm$ for both scans. All the CT scans have dimensions of 512×512 voxels inplane, and $130-180$ slices. Some of the cases show a clearly visible cancer mass in the CT scans. The typical image size for the PET image was $256 \times 256 \times 102$-$178$ voxels with a voxel size of $2.65mm \times 2.65mm \times 5mm$.

We have used the d-CT volumes as the target images, and cropped the AC-CT volumes to match the d-CT image as the source images. The final deformations of the registration step are then used to warp the PET images to align them with the d-CT. Warping of the images is performed using tri-linear interpolation of the intensities.

The segmentation of the lungs is needed to localize the lung boundaries where sliding motion might occur. Lung segmentation for d-CT and AC-CT volumes was performed using a semi-automatic procedure, consisting of an initial level set segmentation using ITK-SNAP [144] followed by a slice-wise manual correction of the boundaries. The lung segmentations are also used to validate our registration method by measuring the lung volume overlap before and after registration. As shown in Figure 6.1, the d-CT has a larger lung volume than the AC-CT, as the lungs are fully expanded (at maximum inspiration). There is also a visible contrast agent in the heart of the diagnostic CT that assists the visualization of the vascular structures. Before applying the fluid and the proposed registration methods, a rigid alignment was performed between the diagnostic and AC-CT volumes using a six parameter rigid body transformation with cross correlation as a similarity measure.

The rigid alignment is followed by the classic fluid registration, and our proposed physiologically motivated registration method, incorporating sliding motion, and also preservation of rigid structures and topology. The similarity measures used for the classic fluid registration and the proposed methods is LCC, described previously in Chapter 5.3.1. A multiresolution scheme was used with three levels of resolution. The maximum number of iterations was around 100 at the coarser levels, and 50 iterations at the highest resolution. The convergence criteria were similar to the criteria designed for the POPI dataset, i.e., if there is no effective change in similarity, the algorithms move on to the next higher resolution. For our proposed method, we choose the size of the window Ω_R as $5mm \times 5mm \times 5mm$. The spatially varying rigidity filter is applied after every two iterations, this has been found to be the optimal choice based on our work in Chapter 3. The average execution time for the entire registration process is 40 minutes. The CT images have been down sampled in-plane to 256×256 voxels to reduce the computational complexity.

We evaluate the accuracy of the d-CT and AC-CT registration by comparing the alignment of ten anatomical landmarks (3D locations within the images) as predicted by the algorithm against a reference. The reference landmarks on the d-CT and AC-CT have been selected by experts using anatomical references (such as the Carina or the topmost point of the lung). The ten anatomical references used for landmark selection are:

1. Top of the aortic arch
2. Bottom of the aortic arch
3. Carina of the trachea
4. Bifurcation of the pulmonary arteries
5. Apex of the heart
6. Centre of the left ventricle
7. Top of right lung
8. Top of left lung
9. Top of the liver
10. Centre of a vertebrae

Figure 6.3 shows the distribution of the landmark on the d-CT image. Figure 6.4 and 6.5 display each of the landmarks in more detail.

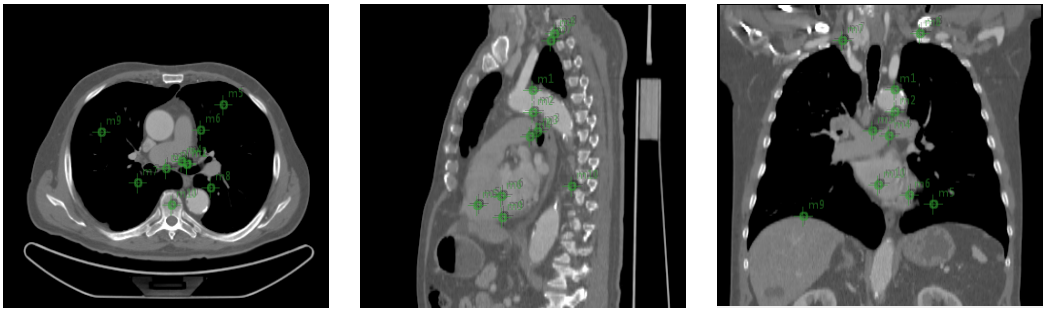

(a) (b) (c)

Figure 6.3: A diagnostic CT image showing distribution of the ten anatomical reference landmarks.

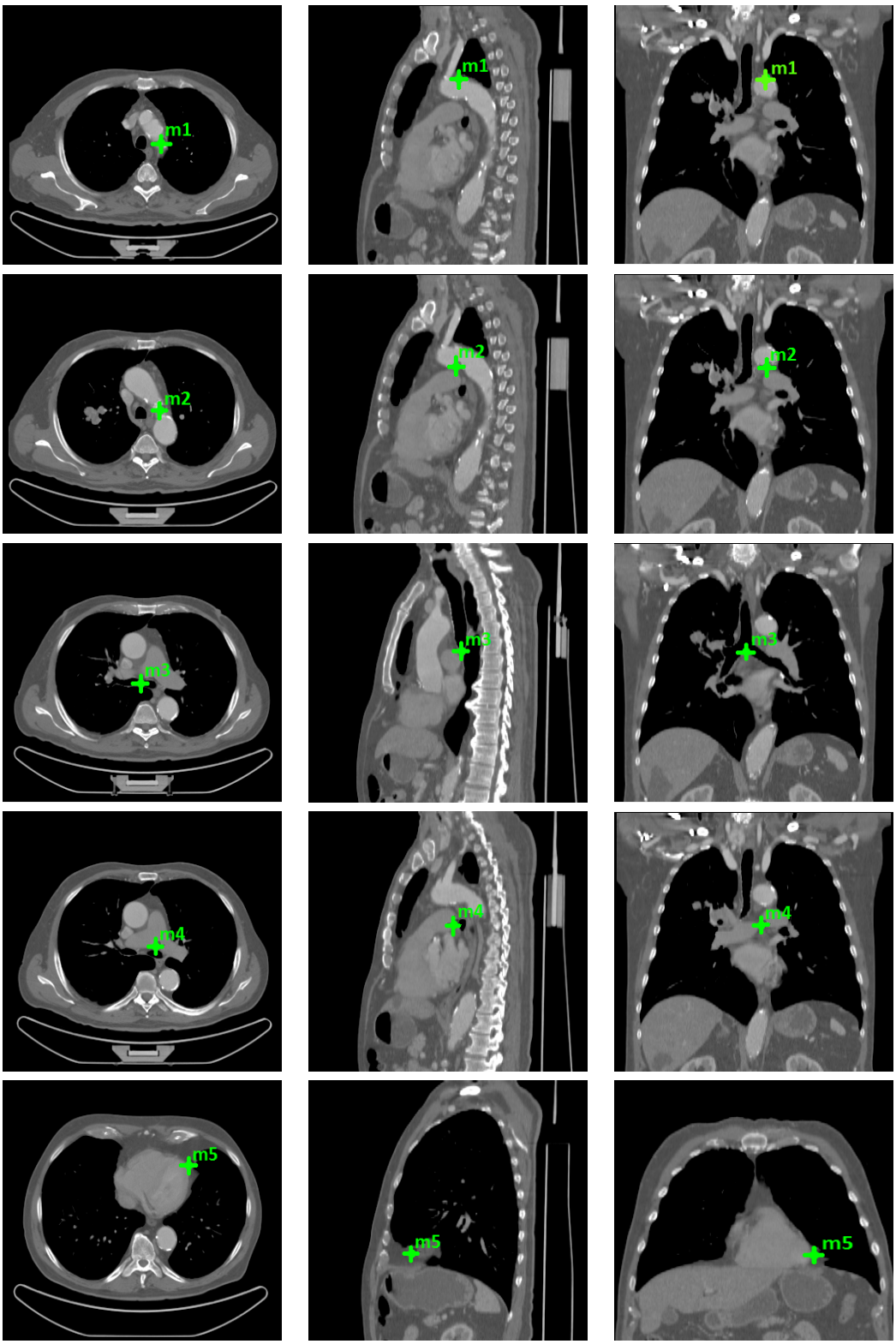

Figure 6.4: Landmarks 1 to 5 (row 1 to 5). The landmarks are selected based on anatomical reference points.

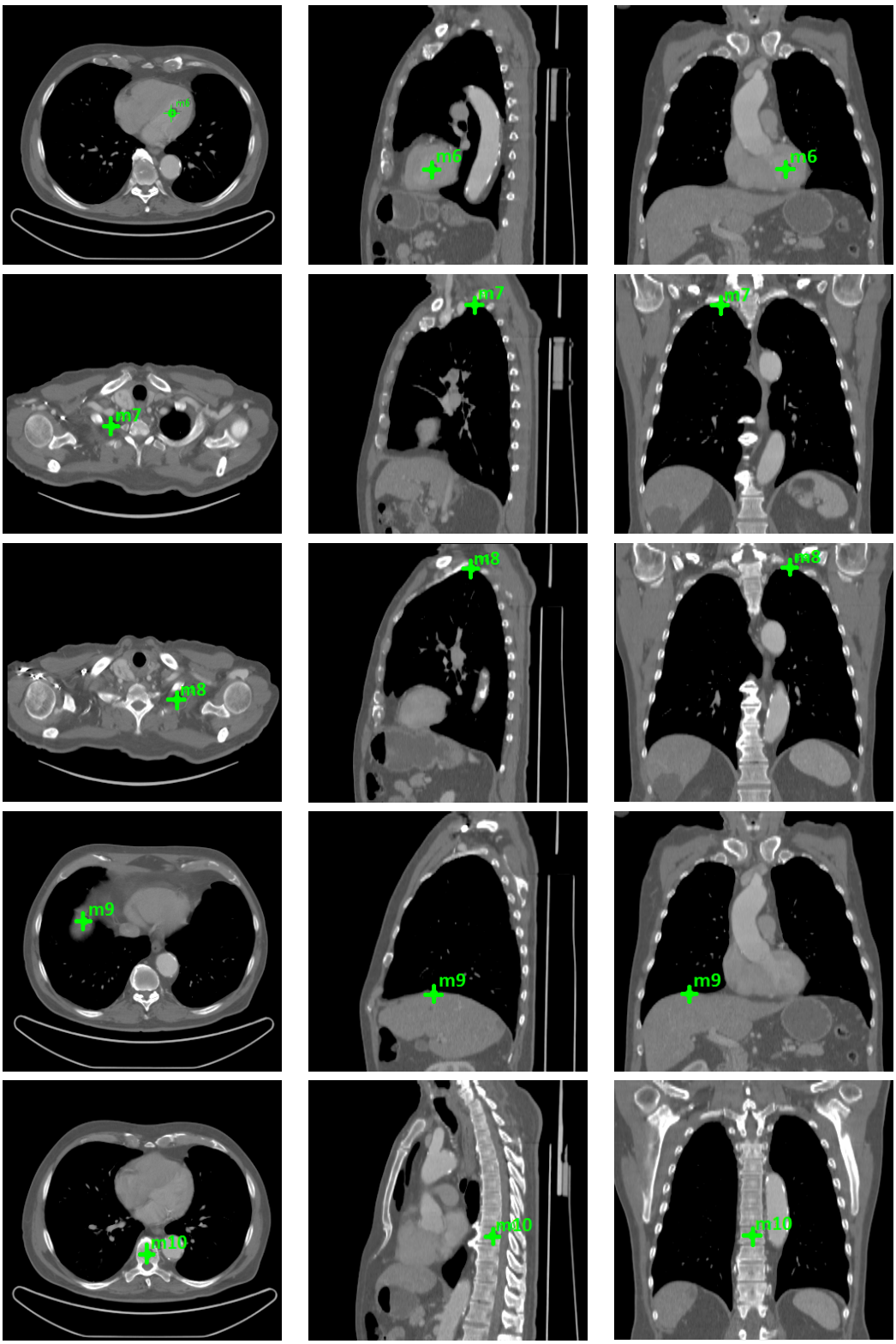

Figure 6.5: Landmarks 6 to 10 (row 1 to 5). The landmarks are selected based on anatomical reference points.

The registration algorithms are also compared on the basis of lung segmentation overlap.

We qualitatively assess the success of the algorithm by analyzing the deformed AC-CT images and fused images of d-CT/PET. The qualitative assessment looked at the alignment and shape of the ribs, internal structures of the lungs such as air vessels, spine and also the overlap of the large tumours.

6.3 Results and Discussion

The resulting lung volume overlaps are shown in Figure 6.6. Our proposed method has better overlap ratios with an average DSC of 0.95 ± 0.0103 compared with the classic fluid method that showed DSC of 0.91 ± 0.0149). A paired, non-parametric, two-sided Wilcoxon rank sum test was used to assess the median differences of the overlap measures between the classic fluid registration and the proposed method. The Wilcoxon rank sum test is generally used when the population cannot be assumed to be normally distributed. The Wilcoxon rank sum test was performed on the lung overlap measures, in order to confirm that the results were significantly different at 5% significance level (p=0.000246).

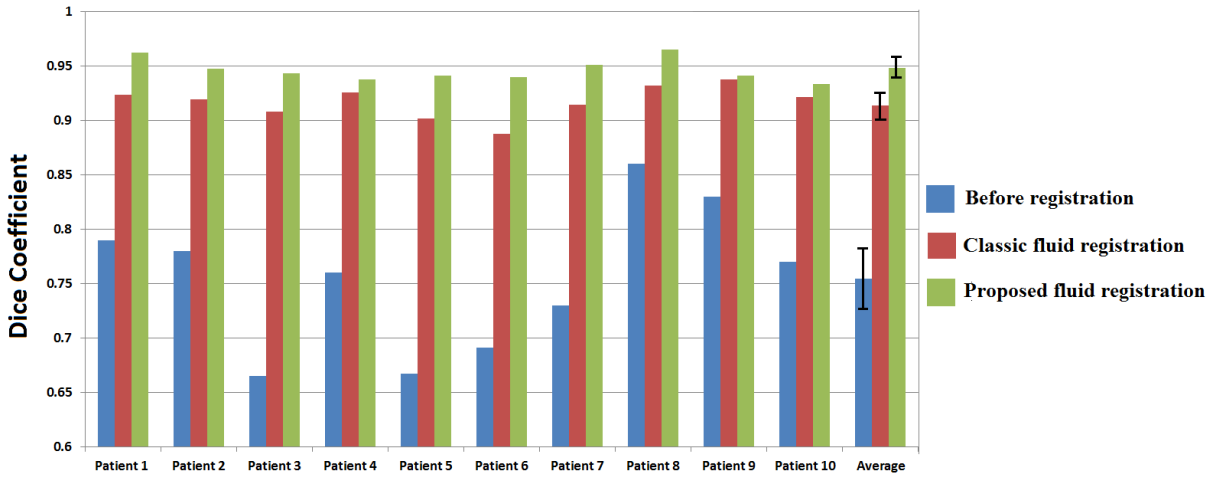

Figure 6.6: Lung overlap ratios for the diagnostic CT - PET/CT datasets, before registration, and after classic fluid registration, as well as our proposed method.

The results of the landmark target registration error (TRE) are shown in Figure 6.7. The classic fluid image registration has a comparatively poor performance with respect to our proposed registration technique. The maximum TRE before registration for one of the

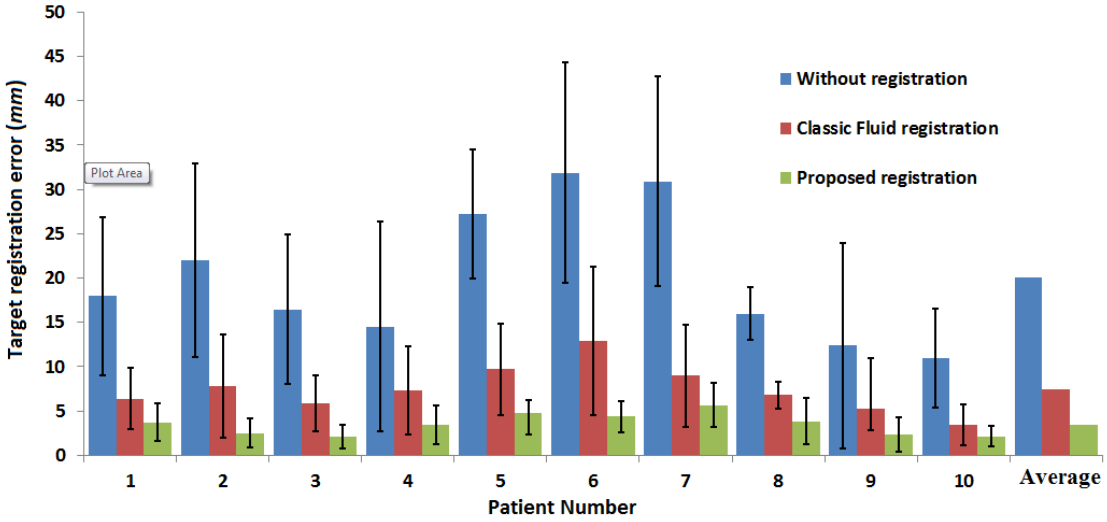

Figure 6.7: Landmark target registration error results for d-CT and AC-CT dataset, before registration, after classic fluid registration and proposed method using sliding motion and preservation of rigid structures as well as topology.

landmarks in patient 7 was found to be $53mm$. The mean TRE of the classic fluid registration is greater than $6mm$ for most cases with the exception of patient 9 and patient 10. Our proposed technique has highest TRE in the registration of patient 8 where the mean TRE for 10 landmark points is $5.67mm$. In case of the selected landmarks, there is a scope of human error especially in case of landmarks that represent different physical locations on the two images but the same anatomical point on both images. The average TRE for classic fluid registration is $7.46mm \pm 2.49mm$ and the average TRE for the proposed method is $3.49mm \pm 1.15mm$. Figure6.8 provides a detailed chart of the TRE for each landmark for the 10 patients using the proposed fluid registration method. The average TRE for the top of left and right lung landmark provides the best results throughout the 10 images. The average TRE for the top of the liver and the centre of the left ventricle are slightly higher than other landmarks. Accurate matching selection of these two landmarks for different phases of breathing is complex and prone to human error. This could be the cause of comparatively higher TRE's for these two specific landmarks across all the images.

Figure 6.9 depicts an example result for the registration using the classic fluid registration technique and our proposed method. Our proposed method has aligned many of the internal structures including the small lung airways and the blood vessels, as pointed out by the red

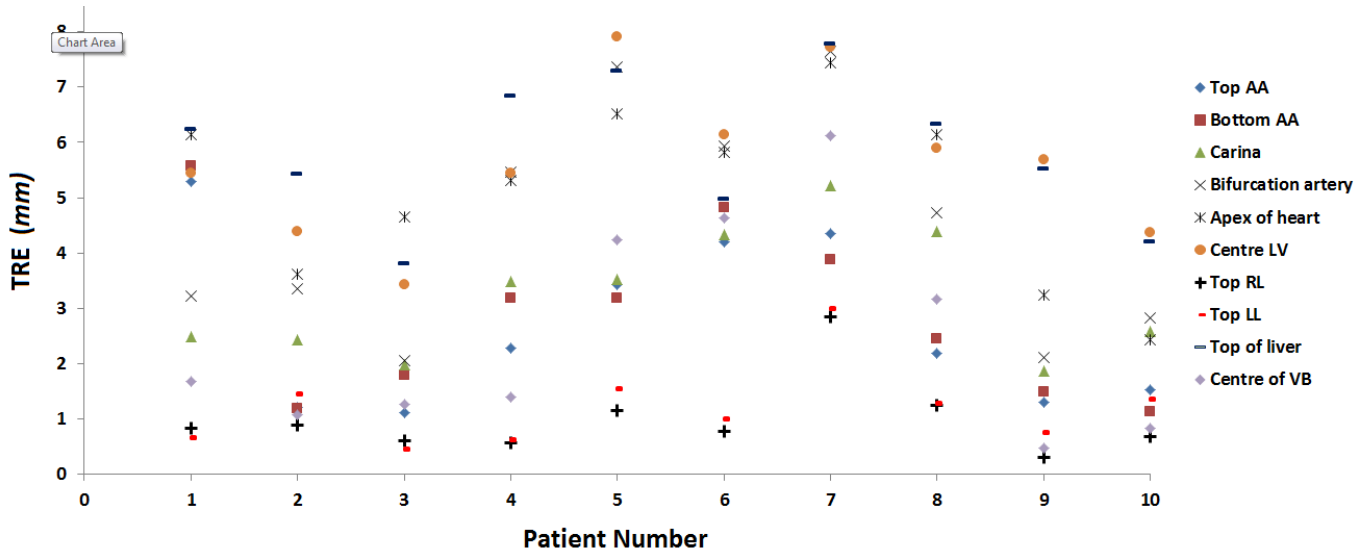

Figure 6.8: TRE for each landmark (for 10 patients) using proposed fluid registration technique. The top of left and right lung landmarks provide the lowest average TRE results.

arrows, while the classic fluid registration has been unsuccessful in properly aligning small structures. As shown in the Figure 6.9 (e) and (f), the classic fluid registration also leads to bending or non-rigid deformations of the bones while our proposed method has maintained the shape and the rigidity of the bones. The average Jacobian values for the bones is shown in Table 6.1. A Jacobian value close to 1 indicates that the volume has been preserved which helps maintain the rigidity of the bones. The best results of the proposed method are obtained for patient 9.

Patient no.	1	2	3	4	5	6	7	8	9	10
Classic fluid registration	1.13	1.15	1.20	1.12	1.21	1.18	1.18	1.07	1.14	1.13
Proposed registration	**1.04**	**1.03**	**1.04**	**1.02**	**1.05**	**1.04**	**1.03**	**1.02**	**1.01**	**1.05**

Table 6.1: Jacobian values for the bones (spine and ribs).

Figure 6.10 shows a fusion results for a diagnostic CT with the PET volume and the difference images for the same are shown in Figure 6.11 . As pointed out by the white arrows, the classic fluid registration method has been able to recover most of the motion, but it shows a large misregistration of the tumour. In contrast, the proposed method has more accurately aligned the tumour in most cases, which could provide an improved localization of the tumour necessary for diagnosis and therapy. The diagnostic CT/PET fusion provides

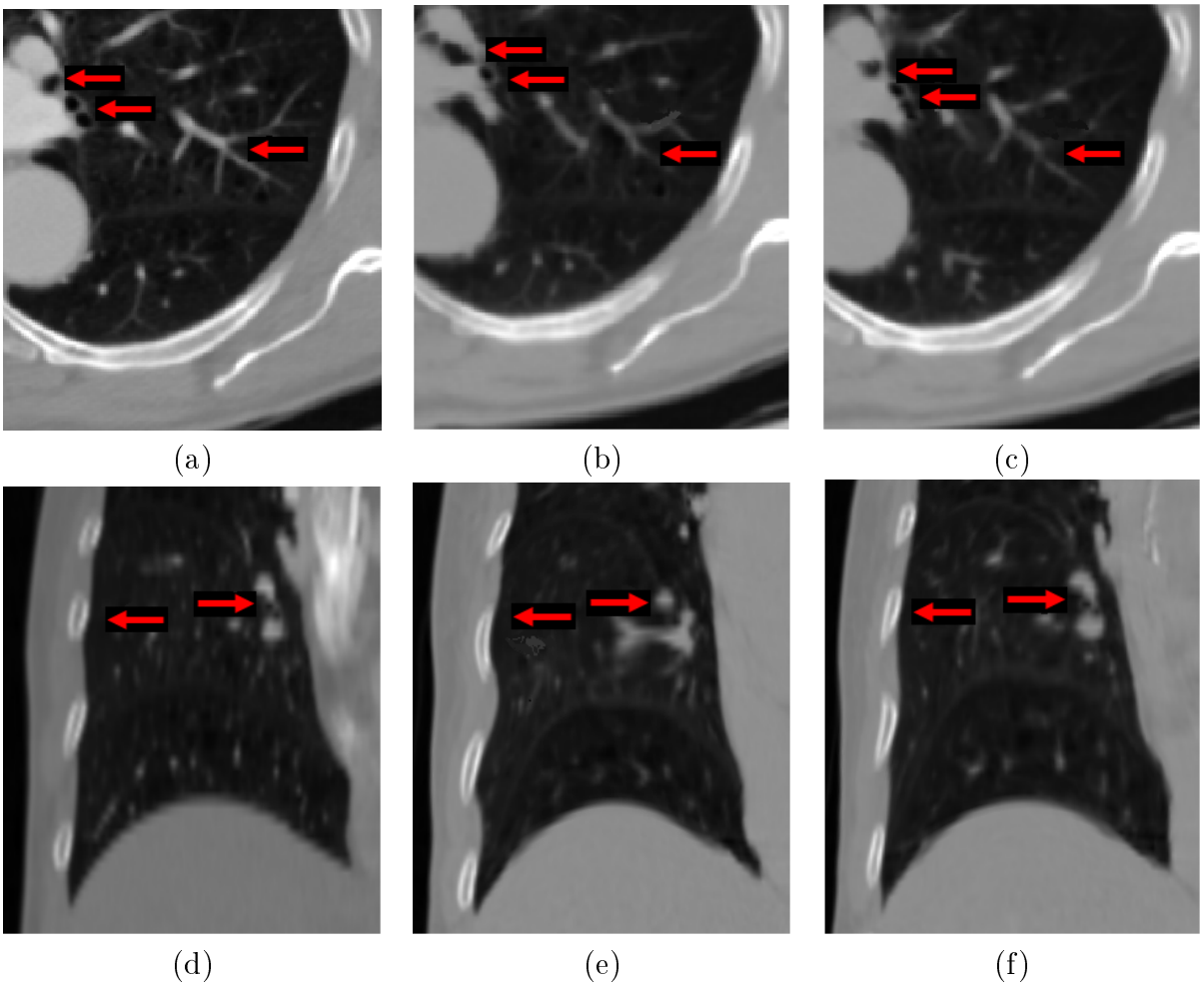

Figure 6.9: Region of interest (ROI) :(a) and (d) target image, (b) and (e) deformed source image using classic fluid registration, (c) and (f) deformed source image using proposed registration technique.

greater information with the vascular structures delineated in the diagnostic CT to avoid any misdiagnosis. The worst case performance for the proposed registration is shown in Figure 6.12 where it has been partially unsuccessful in aligning the tumour. However, as seen from the figure, the proposed registration has still performed better than the classic fluid method. The difference images for the worst case are provided in Figure 6.13.

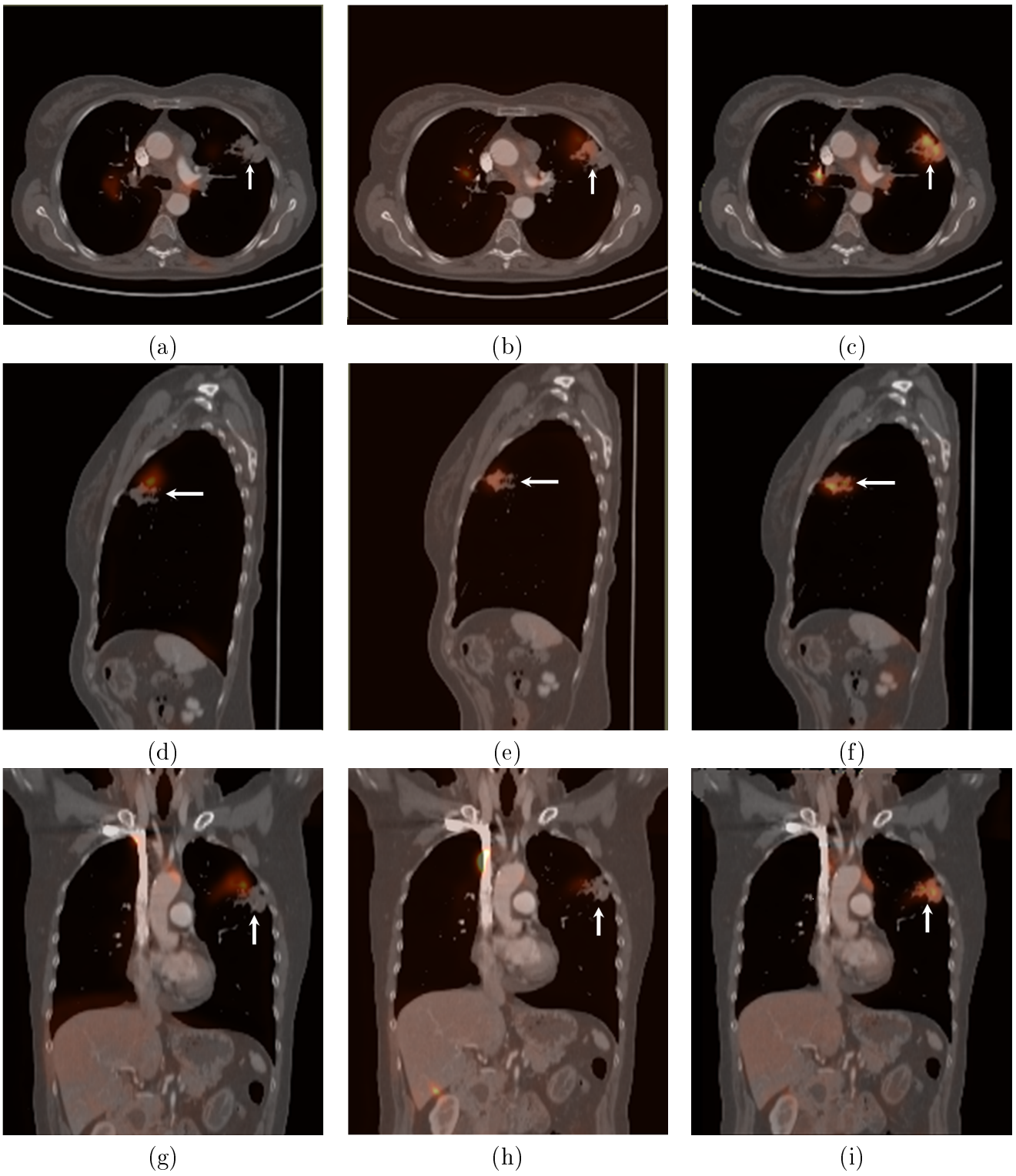

Figure 6.10: Three orthogonal views of fused diagnostic CT and PET images (Patient 1): First column (a), (d) and (e) without registration. Second column (b), (e) and (h) results using classic fluid registration. Third column (c), (f) and (i) results using our proposed method. The white arrows in the image volumes clearly show that the proposed method has been successful in an improved alignment of the PET image and the diagnostic CT.

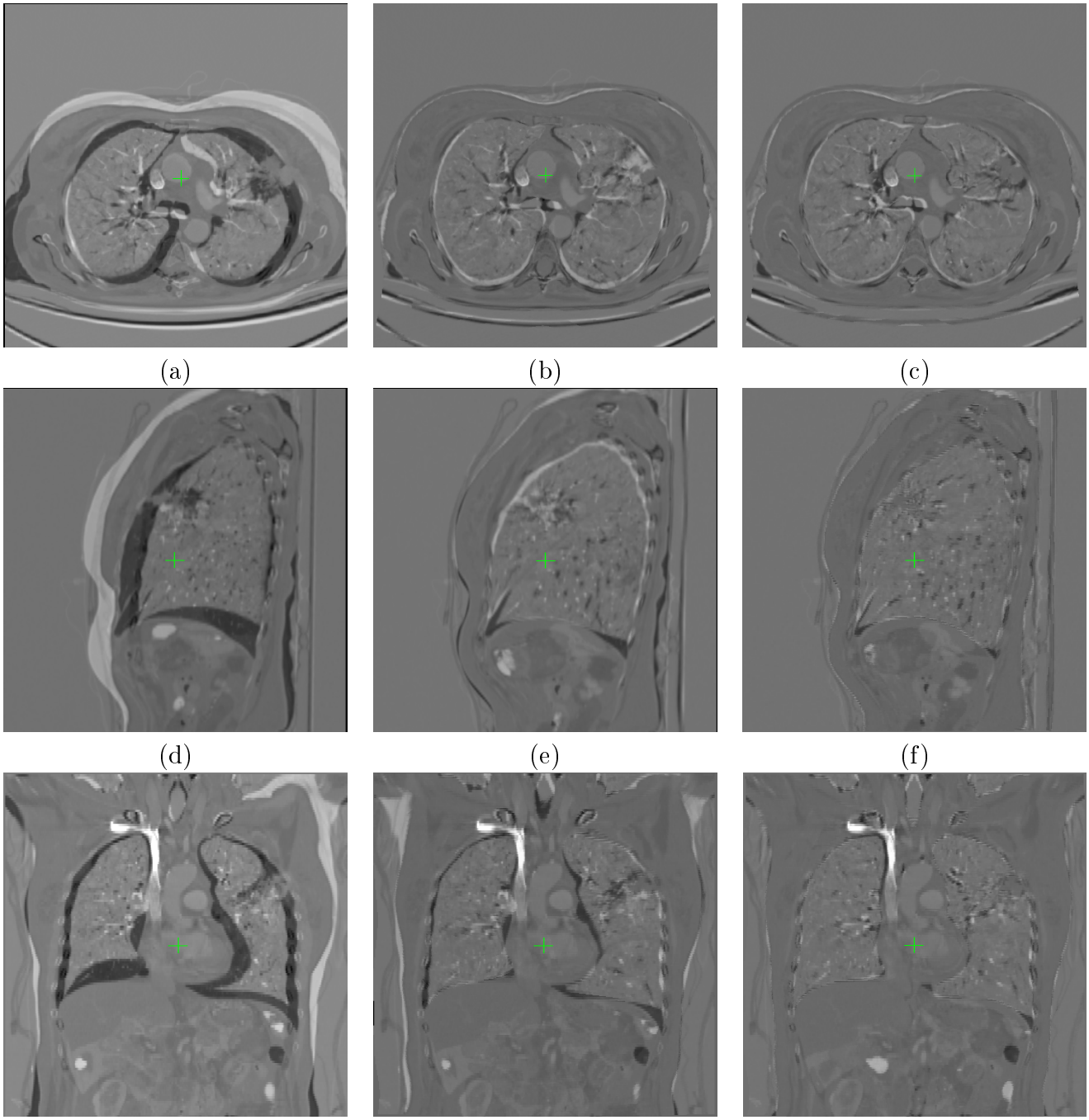

Figure 6.11: Three orthogonal views of difference images between diagnostic CT and AC-CT images (Patient 1): First column (a), (d) and (e) without registration. Second column (b), (e) and (h) results using classic fluid registration. Third column (c), (f) and (i) results using our proposed method.

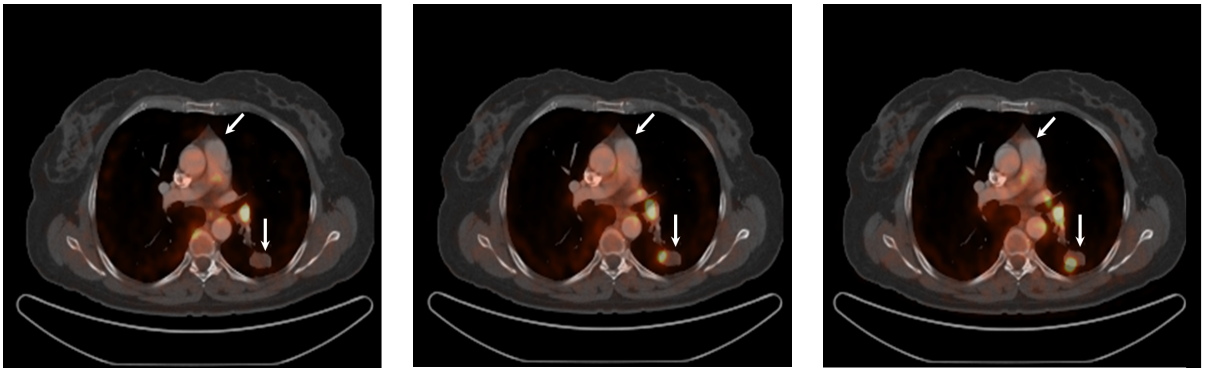

(a) (b) (c)

Figure 6.12: Fused diagnostic CT and PET images (Patient 6). (a) without registration (b) with classic fluid registration (c) with our proposed registration technique. The white arrows point towards the tumour. The proposed registration has been unsuccessful in complete alignment of the tumour.

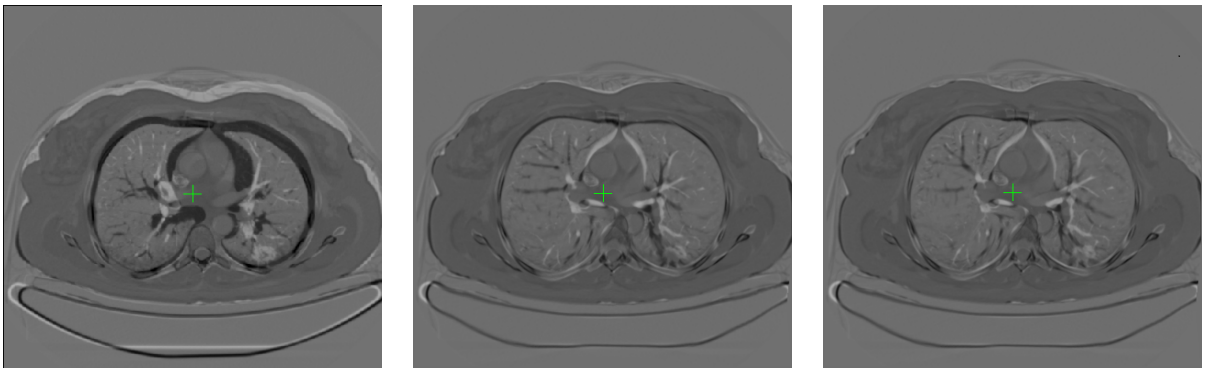

(a) (b) (c)

Figure 6.13: Difference image between diagnostic CT and AC-CT images (Patient 6). (a) without registration (b) with classic fluid registration (c) with our proposed registration technique.

To analyze the registration of the tumours, we manually segment the tumour structures in the diagnostic and AC-CT and then compare the overlap ratios after non-rigid registration. The tumours were segmented in image volumes where they were significantly large and clearly visible. The results of the overlap ratio are shown in 6.2. The proposed registration method with an average tumour overlap ratio of 0.9215 has a better performance in comparison to the classic fluid method with average tumour overlap ratio of 0.9014. However, the proposed method has not been able to improve its performance for the registration of the tumour for patient 6.

Patient Number/Overlap ratios	After rigid registration	Using classic fluid method	Using proposed method
Patient 1	0.7659	0.9463	0.9541
Patient 4	0.6982	0.8953	0.9126
Patient 6	0.6783	0.8424	0.8579
Patient 7	0.7346	0.9173	0.9390
Patient 8	0.8389	0.9147	0.9401
Patient 10	0.6198	0.8923	0.9252
Average	0.7226	0.9014	0.9215

Table 6.2: Tumour overlap ratios for the diagnostic CT - PET/CT datasets.

6.4 Conclusions

We have presented a new retrospective non-linear registration algorithm for fusing d-CT with PET image volumes. Our proposed registration algorithm was shown to be able to remove the non-linear mismatch of the d-CT and the AC-CT images. We have quantitatively assessed the image pairs using 10 anatomical landmark points and the overlap ratios. We also assessed the images qualitatively by looking at the air vessel trees and the alignment of the tumour on the fused d-CT/PET image, showing superior qualitative alignment compared to the classic fluid registration method.

Our conclusions for the current chapter are as follows:

- Our proposed registration technique is able to achieve better overlap measures compared to the classic fluid registration technique.
- Even though our technique has performed poorly in one of the cases with respect to landmark TRE but it still shows much better performance in all other cases against the classic fluid registration technique.
- The ribs and the spine also do not undergo deformation during registration for our technique, as visible from the warped images and the Jacobian values of the bones.
- The fusion of the d-CT and PET has also shown superior results using our proposed registration technique.

Chapter 7

Summary and Future Work

7.1 Summary

The goal of this thesis was to accurately fuse thoracic d-CT with whole body PET image volumes. Such fusion is required to improve the visualization and the analysis of the medical images for lung cancer staging. In order to achieve an accurate fusion of the d-CT with PET, we first register the d-CT with the AC-CT and then use the deformations from this registration step to align the d-CT with the PET image. Thus, our primary task has focused on developing a registration framework for accurate anatomical alignment of the d-CT with AC-CT.

To register the d-CT and AC-CT, we started with conventional physics based transformation models, i.e., elastic and fluid transformation models. Although the methods achieve satisfactory results for a range of applications, these standard approaches show three major disadvantages when applied to medical images: Firstly, the image regions that correspond to different anatomical structures such as bones or soft tissue, are all treated in the same way. Secondly, both these methods fail in preserving the topology of the images. Lastly, these methods also smooth the naturally occurring sliding motion at the lung boundaries. Since these registration techniques do not consider the physical properties of the various structures within the image, the final transformation is not guaranteed to provide a physically and physiologically plausible solution. The final transformation might even exhibit physically

implausible deformations of rigid structures like ribs or folding of the deformation field.

To preserve the rigidity of the bones, we adopt a spatially varying filter that calculates the average amount of deformation around local regions of voxels, which is then assigned to be the deformation at that particular voxel using a stiffness coefficient. Based on visual inspection of the data and the Jacobian values of the deformation at the bones in Chapters 3, 4 and 5, we conclude that adaptive filtering of the deformation field is able to improve registration results by successfully preserving the rigidity of the bones without affecting the overlap of the bones or lungs.

Folding of the deformation field during registration violates the topology of the deformation field. To preserve the topology, we introduce a topology preserving force term in the elastic and fluid registration framework. This force term uses the Jacobian values to penalize the similarity forces that push the deformation towards folding. As shown in Chapter 3, the topology preserving term has performed very well in reducing the folding of the deformation field for the NCAT images. However, it was also found that the topology preserving term is not successful in reducing the folding if the images are cropped as shown in Chapter 4 with the EMPIRE 2010 challenge dataset. Cropped images provided by the EMPIRE 2010 challenge cuts through many important organs which could otherwise drive the registration process outside the lungs. In later experiments (shown in Chapter 4), it was found that artificially expanding the cropped image helps to improve the performance of the topology preservation term.

Based on our work in Chapters 3 and 4, we also conclude that the elastic registration framework is not suitable for our application because it is not able to recover large deformations. This prompted us to shift our focus from elastic to fluid registration. Thus, we use the fluid transformation model as the base transformation model. The sliding motion model developed in chapter 5 gave us the opportunity to model the discontinuous motion of the lungs along the boundary which is similar to the physical motion of the lungs during breathing. The proposed fluid method with topology constraints, rigidity constraints and the sliding motion model has been validated on the POPI and EMPIRE datasets (uncropped field of

view images). The proposed method has performed better than the classic fluid method both quantitatively and qualitatively.

In Chapter 6, we show the results of fusing the d-CT and PET when using our registration framework. We validated our proposed method with sliding motion, topology preservation and rigidity preservation on 10 clinical datasets. The proposed method has outperformed the classic fluid approach with respect to the TRE of the landmarks and the lung overlap ratios. Visual inspection of the fused d-CT and AC-CT images has also proved that our proposed method has provided a better alignment of the tumours and other structures.

7.2 Future work

The work presented in this dissertation can be extended in several directions. In this section, we describe a couple of these extensions, along with some suggestions that might be applicable in addressing these problems.

7.2.1 Effects of Low Pass Filtering in Multiresolution Techniques

For future work, we suggest to further investigate the effects of low pass filtering in multiresolution techniques. Multiresolution techniques are used in image registration to reduce computational time and avoid the solution from falling into local minima. The coarser level solution serves as initial data for solving the problem at a finer scale. These techniques help to recover large deformations at coarser resolutions, thus reducing the number of iterations required at finer resolutions. Solving the registration at a coarser resolution prevents the algorithm from getting trapped into physically irrelevant local minima. However, there are also some disadvantages associated with the multiresolution approach. In multiresolution image registration, the Gaussian filtering or low pass filtering is generally used before downsampling the image for coarser resolution. Gaussian smoothing applied before downsampling of the image to the next coarser level smoothes the edges. This indiscriminate smoothing tends to blur and dislocate the edges when the images are downsampled from a finer resolu-

tion to a coarser resolution. Thus the edges that are identified at a coarse scale may not be at the correct location [145, 146, 147]. They have to be located at the finer (original) scale image. The blurring and dislocation of the edges and other features also depends on intensity distributions of the smoothed image. However, it is essential to preserve the sharp contrast boundaries of the structures such as the bones throughout the different resolution levels. If the edges are dislocated or blurred out, this will inevitably lead to inaccurate registration.

This problem can be addressed in various ways. One of the earliest attempts to solve this problem was made by Bergholm [148]. Bergholm introduced the idea of edge focusing whereby edges are tracked from coarse to fine resolution. Goshtasby [146] further optimized the edge focusing algorithm to improve the edge tracking when some edges split into two, or two edges merge into one while varying the resolution.

Another approach to address this problem is to use non-linear diffusion methods for smoothing the images. Such methods smooth the homogeneous regions while preserving the edges. Non-linear diffusion methods are normally used for image denoising and image restoration, and have the property of preserving the edges. One of the common non-linear diffusion techniques used in image processing is the Perona-Malik diffusion method [149]. The method is mostly used to prevent blurring problems of Gaussian smoothing. The Perona-Malik model implements an inhomogeneous process by applying a weak smoothing term at the edges while using a strong smoothing term within the homogenous regions. The Perona-Malik method reduces the diffusivity at those locations that have a higher likelihood to be edges. This likelihood is determined by the gradient of the image (∇I). Over the years, a variety of other non-linear diffusion models have been applied for use on medical images [150, 151, 152]. A detailed review of the various non-linear diffusion methods can be found in [153].

A natural question that arises: How will these new techniques influence the registration process? A thorough analysis and comparison of the various methods is required to study the effect on the registration results. For our registration framework, we also need to study the effect of the alternate smoothing techniques on our rigidity filter and the sliding motion

model. Eliminating the edge blurring and dislocation will probably help to preserve of bony structures even at the coarsest resolution. This might assist the rigidity filter in improving the alignment of the bones.

7.2.2 Incorporating Anatomical Information

As mentioned in Chapter 5, using anatomical information in the registration process helps in obtaining physiologically plausible deformations. Our registration framework uses bone thresholding to provide stiffness maps for the rigidity filter and the segmentation of the lungs delineates the surface where sliding motion occurs. Vessel trees of the lung parenchyma form an additional source of information that can help improve the alignment of the inner details of the lung. Some initial work has already been conducted in this research arena. One of the participating algorithms in the EMPIRE challenge proposed a non-rigid registration algorithm that uses the vessel tree segmentation of the lung parenchyma as a cost function to match the vessel shape and location during registration [81]. Another algorithm by Loeckx et al. [77] extends the B-spline registration method by adding 3D registration of the vessel tree to supplement the registration process. Both these methods extract the vessel tree in the lung parenchyma using thresholding followed by a few preprocessing steps to remove noise. However, with regards to our application, automatic segmentation of the vessel tree is complicated by the presence of a contrast agent in the diagnostic CT image, and the lack of any contrast agent in the AC-CT. Though some initial work has been established for semi-automatic extraction of the vessel tree from contrast enhanced images [154, 155], it still requires a large degree of human intervention. If the segmentation of the vessel tree can be automated for the contrast enhanced images, this information could potentially be incorporated into our registration framework by using additional forces based on the lung vasculature location and related image features.

7.3 Conclusions

This thesis has explored key components of lung CT image registration: namely, topology preservation, rigidity preservation and sliding motion of the lungs. The proposed fluid regularization framework reflects our understanding of the physical properties of the image structures that need to be preserved during chest CT image registration. The inclusion of these physical conditions directs the ill-posed problem of registration towards a physically plausible solution.

To conclude, our three main contributions made in this thesis are:

- Design of a registration method that incorporates topology preservation and rigidity preservation in a single framework
- Development of sliding motion model that was validated on a large amount of data
- Fusion of d-CT and PET using the above developed registration framework for aligning d-CT and AC-CT.

We have investigated several questions on image registration during the course of the D.Phil. However, many other questions still remain to be answered. With the increasing focus of the research community towards lung CT registration, more definite solutions will be discovered in the near future.

Appendix A

Formulation of Linear Elasticity operator

An elastic medium offers a resistance to the deformation applied by the external forces which are acting on and between the image elements/pixels. The forces generated by this resistance helps to ensure the continuity of the medium ensuring that the medium does not tear or fold due to the external forces.

Strain is defined as the deformation of a volume element of the elastic material. There are two types of strain : Extensional and shear. The extensional strain is the stretching or compression of the material due to tensile forces applied normal to a surface of a volume element. Shear strain are deformation within the plane of the surface of the element at the point of application of forces. To generalise the concept of strain introduced we consider the deformation of a small line segment joining two neighbouring particles with initial positions $\boldsymbol{X}$ and $\boldsymbol{X} + \boldsymbol{\delta X}$. After some time, the solid is deformed such that the particles are displaced to $\boldsymbol{x} = \boldsymbol{X} + \boldsymbol{u}(\boldsymbol{X})$ and $\boldsymbol{x} + \boldsymbol{\delta x} = \boldsymbol{X} + \boldsymbol{\delta x} + \boldsymbol{u}(\boldsymbol{X} + \boldsymbol{\delta x})$ respectively. Using Taylor's theorem the line element $\boldsymbol{\delta x}$ is transformed to:

$$\boldsymbol{\delta x} = \boldsymbol{\delta X} + \boldsymbol{u}(\boldsymbol{X} + \boldsymbol{\delta X}, t) - \boldsymbol{u}(\boldsymbol{X}, t) = \boldsymbol{\delta X} + (\boldsymbol{\delta X} \cdot \nabla)\boldsymbol{u}(\boldsymbol{X}, t) + O(|\boldsymbol{\delta X}|^2), \tag{7.1}$$

$$\boldsymbol{\delta X} \cdot \nabla = \left(\delta X_1 \frac{\partial}{\partial X_1} + \delta X_2 \frac{\partial}{\partial X_2} + \delta X_3 \frac{\partial}{\partial X_3}\right) = \boldsymbol{\delta X_k} \frac{\boldsymbol{\partial}}{\boldsymbol{\partial X_k}} \tag{7.2}$$

Now let $L = |\boldsymbol{\delta X}|$ and $l = |\boldsymbol{\delta x}|$ denote the initial and the current lengths respectively of the line segment. Then $l^2 = |\boldsymbol{\delta X} + (\boldsymbol{\delta X}.\nabla)\boldsymbol{u}(\boldsymbol{X}, t)|^2$. The change in the length of the line

element can thus be written in the form:

$$l^2 - L^2 = 2\varepsilon_{ij}\delta X_i \delta X_j, \tag{7.3}$$

$$\varepsilon_{ij} = \frac{1}{2}\left(\frac{\partial u_i}{\partial X_j} + \frac{\partial u_j}{\partial X_i} + \frac{\partial u_k}{\partial X_i} + \frac{\partial u_k}{\partial X_j}\right). \tag{7.4}$$

It is clear from the above equation that the stretch of a line element is measured by the dimensionless quantity ε_{ij}. Considering materials that undergo small deformations only, it can be assumed that $\frac{\partial u_i}{\partial X_j}$ is very small and we can neglect the third term (non-linear term) in the above equation 7.4. In addition, we note that the chain rule relating differentiation with respect to the Eulerian and Lagrangian variables can be expressed as:

$$\frac{\partial}{\partial X_i} = \frac{\partial x_k}{\partial X_i}\frac{\partial}{\partial X_k} = \frac{\partial}{\partial x_i} + \frac{\partial u_k}{\partial X_i}\frac{\partial}{\partial x_k}. \tag{7.5}$$

Hence we can write the linearised strain as:

$$\varepsilon_{ij} \sim \frac{1}{2}\left(\frac{\partial u_i}{\partial X_j} + \frac{\partial u_j}{\partial X_i}\right) \sim \frac{1}{2}\left(\frac{\partial u_i}{\partial x_j} + \frac{\partial u_j}{\partial x_i}\right). \tag{7.6}$$

Stress σ is the cohesive force per unit area and is defined by:

$$\sigma = \lim_{\partial A \to 0} \frac{\partial F}{\partial A} = \frac{dF}{dA}. \tag{7.7}$$

The force balancing the equation is given by:

$$\frac{\partial \sigma_{1i}}{\partial x_1} + \frac{\partial \sigma_{2i}}{\partial x_2} + \frac{\partial \sigma_{3i}}{\partial x_3} + F_i = 0, \qquad i = 1, 2, \, and \, 3, \tag{7.8}$$

$$i.e. \quad \nabla.\sigma + \boldsymbol{F} = 0. \tag{7.9}$$

For an isotropic material, elasticity theory gives the stress strain relationship by the linear constitutive relation (Piola-Kirchhoff stress tensor) given by:

$$\sigma_{ij} = 2\mu\varepsilon_{ij} + \lambda(\varepsilon_{kk})\delta_{ij} \tag{7.10}$$

where λ and μ are the Lamé elasticity constants. μ is also called the shear modulus. To obtain the equations in Cartesian coordinates (x, y, z), the displacement components are denoted by $\boldsymbol{u} = (u_x, u_y, u_z)^T$. Substituting the co-ordinates in the linear constitutive equation 7.10 we get:

$$\begin{aligned}
\sigma_{xx} &= (\lambda + 2\mu)\varepsilon_{xx} + \lambda(\varepsilon_{yy}) + \lambda(\varepsilon_{zz}) \qquad & \sigma_{xy} &= 2\mu\varepsilon_{xy} \\
\sigma_{yy} &= (\lambda + 2\mu)\varepsilon_{yy} + \lambda(\varepsilon_{xx}) + \lambda(\varepsilon_{zz}) \qquad & \sigma_{xy} &= 2\mu\varepsilon_{xz} \\
\sigma_{zz} &= (\lambda + 2\mu)\varepsilon_{zz} + \lambda(\varepsilon_{xx}) + \lambda(\varepsilon_{yy}) \qquad & \sigma_{xy} &= 2\mu\varepsilon_{yz},
\end{aligned} \tag{7.11}$$

where

$$\begin{aligned}
\varepsilon_{xx} &= \frac{\partial u_x}{\partial x} \qquad & 2\varepsilon_{xy} &= \frac{\partial u_x}{\partial y} + \frac{\partial u_y}{\partial x} \\
\varepsilon_{yy} &= \frac{\partial u_y}{\partial y} \qquad & 2\varepsilon_{yz} &= \frac{\partial u_y}{\partial z} + \frac{\partial u_z}{\partial y} \\
\varepsilon_{zz} &= \frac{\partial u_z}{\partial z} \qquad & 2\varepsilon_{xz} &= \frac{\partial u_x}{\partial z} + \frac{\partial u_z}{\partial x}
\end{aligned} \tag{7.12}$$

And the three components of the force balancing equation are:

$$\begin{aligned}
\frac{\partial \sigma_{xx}}{\partial x} + \frac{\partial \sigma_{xy}}{\partial y} + \frac{\partial \sigma_{xz}}{\partial z} + F_x = 0 \\
\frac{\partial \sigma_{xy}}{\partial x} + \frac{\partial \sigma_{yy}}{\partial y} + \frac{\partial \sigma_{yz}}{\partial z} + F_y = 0 \\
\frac{\partial \sigma_{xz}}{\partial x} + \frac{\partial \sigma_{yz}}{\partial y} + \frac{\partial \sigma_{zz}}{\partial z} + F_z = 0
\end{aligned} \tag{7.13}$$

And substituting 7.11 in the above three components and assuming that λ and μ are constant, we get the Navier Lamé equations :

$$\begin{aligned}
\mu\nabla^2 u_x + (\lambda + \mu)\frac{\partial}{\partial x}(\nabla.\boldsymbol{u}) + F_x = 0 \\
\mu\nabla^2 u_y + (\lambda + \mu)\frac{\partial}{\partial y}(\nabla.\boldsymbol{u}) + F_x = 0 \\
\mu\nabla^2 u_z + (\lambda + \mu)\frac{\partial}{\partial z}(\nabla.\boldsymbol{u}) + F_x = 0
\end{aligned} \tag{7.14}$$

For further details the reader is referred to any good text on elasticity theory or continuous media such as Timoshenko and Goodier (1970) or Gurtin (1981).

Appendix B

Formulation of 3D Topology Preservation Force Term

In this Appendix, we derive the explicit expression for $\partial_{\boldsymbol{u}} \boldsymbol{E}_2(\boldsymbol{u})$ in equation 3.19 when $\Omega \subset R^3$. The components of the vector $\boldsymbol{x}$ are denoted as (x_1, x_2, x_3) and the components of vector $\boldsymbol{u}$ are denoted as (u_1, u_2, u_3) . Jacobian J is a function of $\partial_j u_i$, for i,$j = 1, 2, 3$ and is given by:

$$J(\partial_1 u_1, \partial_2 u_1, \partial_3 u_1, \partial_1 u_2, \partial_2 u_2, \partial_3 u_2, \partial_1 u_3, \partial_2 u_3, \partial_3 u_3)$$
$$= (1 - \partial_1 u_1)(1 - \partial_2 u_2)(1 - \partial_3 u_3) - \partial_1 u_2 \partial_2 u_3 \partial_3 u_1 - \partial_2 u_1 \partial_3 u_2 \partial_1 u_3$$
$$- \partial_3 u_1 (1 - \partial_2 u_2)\partial_1 u_3 - \partial_2 u_1 \partial_1 u_2 (1 - \partial_3 u_3) - \partial_3 u_2 \partial_2 u_3 (1 - \partial_1 u_1).$$

To obtain the 3D external force term for topology preservation, we would like to minimize the functional $\boldsymbol{E}_2(\boldsymbol{u})$:

$$\boldsymbol{E}_2(\boldsymbol{u}) = \int_\Omega (J(Id + \boldsymbol{u}(\boldsymbol{x})) - 1) log |J(Id + \boldsymbol{u}(\boldsymbol{x}))| d\boldsymbol{x},$$
$$= \int_\Omega (L(J(\partial_j u_i) dx, \qquad 1 \leq i,\, j \leq 3.$$

where $L(J) = (J - 1) log J$. Minimizing the energy $\boldsymbol{E}_2(\boldsymbol{u})$ with respect to u_1, for fixed u_2 and u_3, yields the first topology preservation force component of $\partial_{\boldsymbol{u}} \boldsymbol{E}_2(\boldsymbol{u})$:

$$\partial_{u_1} \boldsymbol{E}_2(\boldsymbol{u}) = \frac{\partial}{\partial x_1}(((1 - \partial_2 u_2)(1 - \partial_3 u_3) - \partial_3 u_2 \partial_2 u_3) L'$$
$$+ \frac{\partial}{\partial x_2}(((\partial_3 u_2 \partial_1 u_3 + \partial_1 u_2 (1 - \partial_3 u_3)) L')$$
$$+ \frac{\partial}{\partial x_3}(\partial_1 u_2 \partial_1 u_3 + \partial_2 u_3 (1 - \partial_1 u_1)) L'),$$

Similarly, the other two components of $\partial_{\boldsymbol{u}}\boldsymbol{E}_2(\boldsymbol{u})$ can be found to be :

$$\partial_{u_2}\boldsymbol{E}_2(\boldsymbol{u}) = \frac{\partial}{\partial x_1}((\partial_2 u_3\partial_3 u_1 + \partial_2 u_1(1-\partial_3 u_3))L') + \frac{\partial}{\partial x_2}(((1-\partial_1 u_1)(1-\partial_3 u_3) - \partial_3 u_1\partial_1 u_3)L') + \frac{\partial}{\partial x_3}(\partial_2 u_1\partial_1 u_3 + \partial_2 u_3(1-\partial_1 u_1))L'),$$

and

$$\partial_{u_3}\boldsymbol{E}_2(\boldsymbol{u}) = \frac{\partial}{\partial x_1}((\partial_2 u_1\partial_3 u_2 + \partial_3 u_1(1-\partial_2 u_2))L') + \frac{\partial}{\partial x_2}((\partial_1 u_2\partial_3 u_1 + \partial_3 u_2(1-\partial_2 u_2))L') + \frac{\partial}{\partial x_3}(((1-\partial_1 u_1)(1-\partial_2 u_2) - \partial_2 u_1\partial_1 u_2)L').$$

The 3D topology preservation force term $\boldsymbol{F}_2$ is given as:

$$\boldsymbol{F}_2 = \partial_{u_1}\boldsymbol{E}_2(\boldsymbol{u}) + \partial_{u_2}\boldsymbol{E}_2(\boldsymbol{u}) + \partial_{u_3}\boldsymbol{E}_2(\boldsymbol{u}).$$

Appendix C

Choice of Lamé constants (λ and μ)

In linear elasticity, the Lamé constants represent the properties related to the elastic behaviour of the material. The first Lamé parameter λ, is related to the bulk modulus of the material. A higher value of λ would inhibit any change in volume for the material when under compression from all sides. λ can be negative, in principle; however, for most real world materials it is positive. μ is the second Lamé parameter or also known as the shear modulus. It quantifies the stiffness of the material. A higher value of μ would lead to a higher stiffness for the material. It is quantified as the ratio of shear stress to the shear strain and is always positive.

During elastic and fluid image registration the choice of values for the Lamé constants controls the stability of the solution and also affects the performance of the algorithm. In this section, we investigate the effect of different values of μ and λ on the registration process.

(a) Target Image **(b) Source Image**

Figure 7.1: Target and source images for evaluation of μ.

We start by evaluating the role of μ (shear modulus) on a pair of synthetic images. The target image and the source image are depicted in Figure 7.1. The target image is $'C'$ while the source image is a circle. The images are registered with each other using classic elastic registration keeping λ at a constant value of zero while varying the value of μ=10, 100, 1000 and 5000. The algorithm is run for 100 iterations during the registration process without any stopping criteria. The results for the different values of μ are shown in Figure 7.2. As observed from the results on increasing μ the body becomes stiffer and does not allow the registration algorithm to reach the full deformation within 100 iterations. For extremely high values of $\mu = 1000$ and 5000 the algorithm is able to recover very small deformation during the 100 iterations.

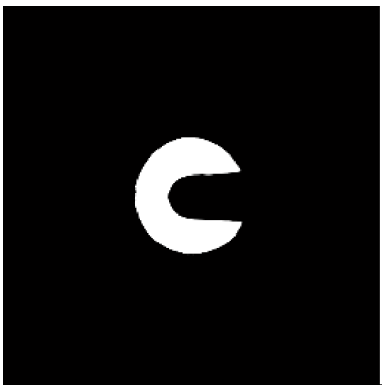

(a) Transformed image ($\mu = 10$)

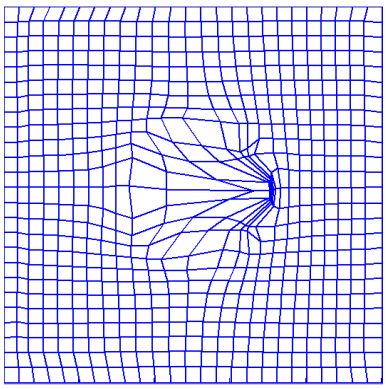

(b) Deformed grid ($\mu = 10$)

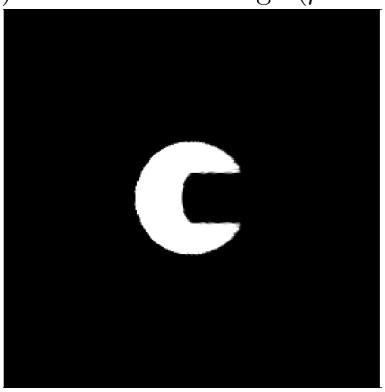

(c)Transformed image ($\mu = 100$)

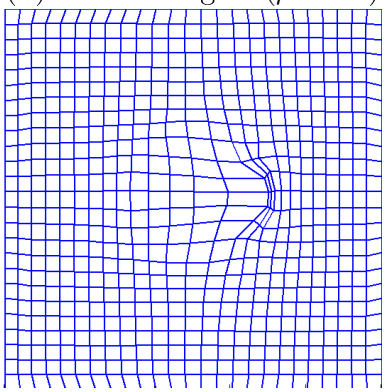

(d) Deformed grid ($\mu = 100$)

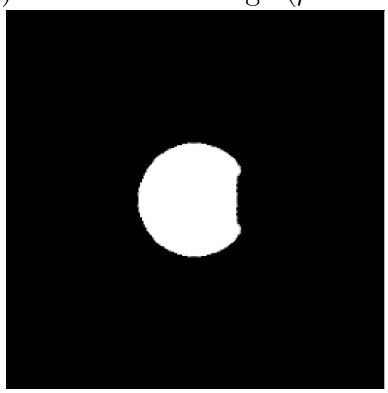

(e) Transformed image ($\mu = 1000$)

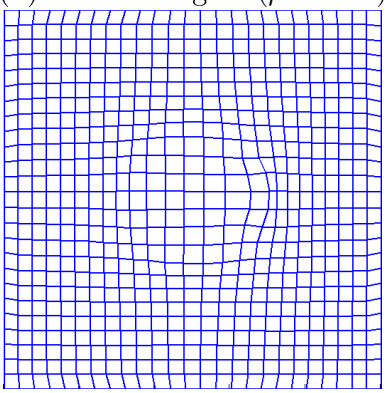

(f) Deformed grid ($\mu = 1000$)

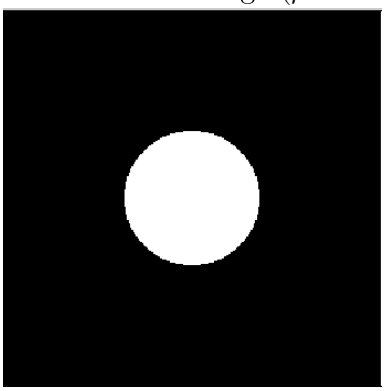

(g) Transformed image 5000)

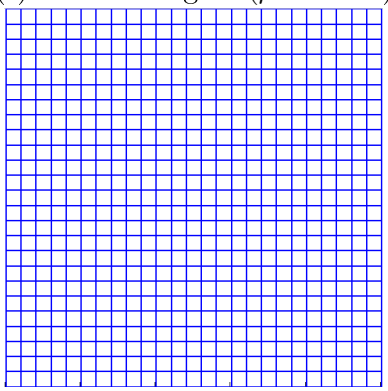

(h) Deformed grid ($\mu = 5000$)

Figure 7.2: Results with various values of μ keeping the value of λconstant at zero. The body becomes stiff as the value of μ increases and for lower values of μ the deformation field shows signs of folding.

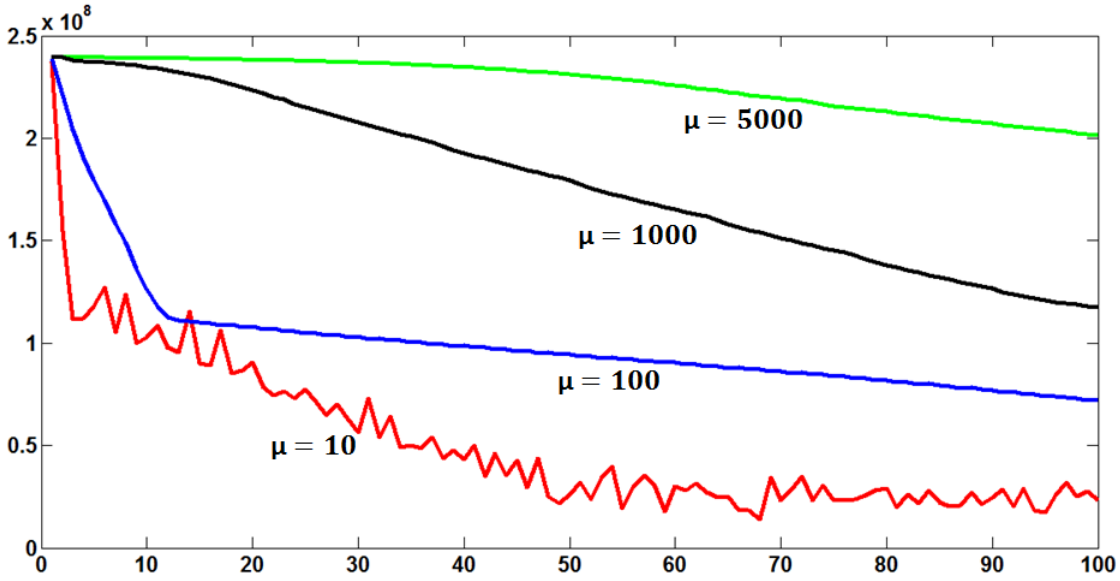

Figure 7.3: SSD with $\mu = 10, 100, 1000$ and 5000 with λ constant at 0.

At the same time if we keep μ very low, like $\mu = 10$, the solution becomes unstable. This instability is visible in Figure 7.2 (b) and Figure 7.3. For $\mu = 10$ the solution shows folding of the deformation field and the solution is mostly controlled by the external forces. Therefore while selecting μ, we should select numerical values that would keep the solution stable but also allow full deformation of the body to reduce registration error. For the given example, $\mu = 100$ presents that balance, where it is able to recover most of the deformation but at the same time provide a stable solution.

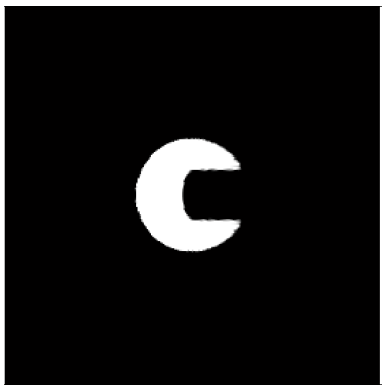

(a) Transformed image ($\lambda = 0$)

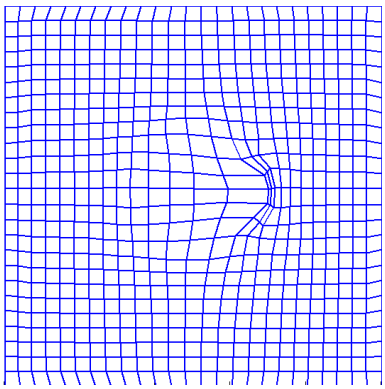

(b) Deformed grid ($\lambda = 0$)

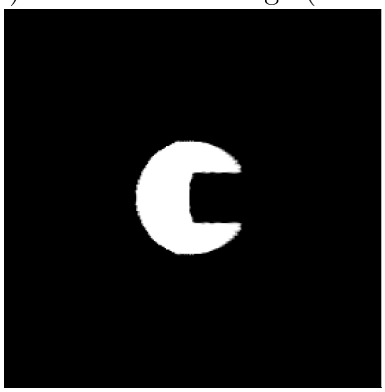

(a) Transformed image ($\lambda = 10$)

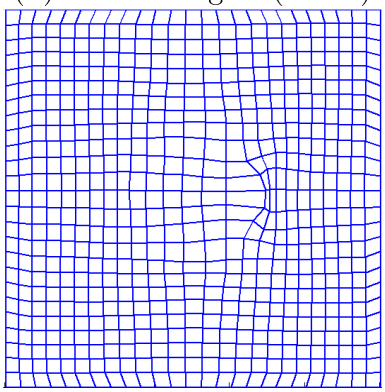

(b) Deformed grid ($\lambda = 10$)

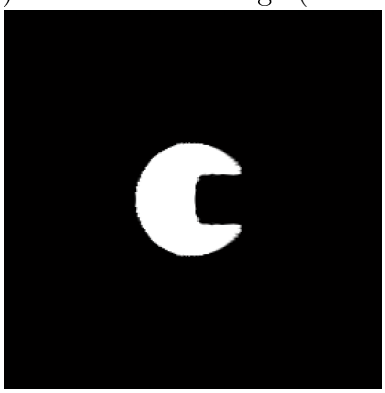

(a) Transformed image ($\lambda = 100$)

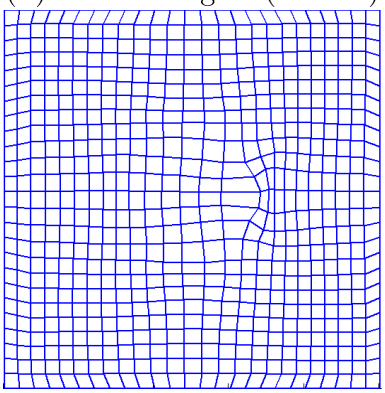

(b) Deformed grid ($\lambda = 100$)

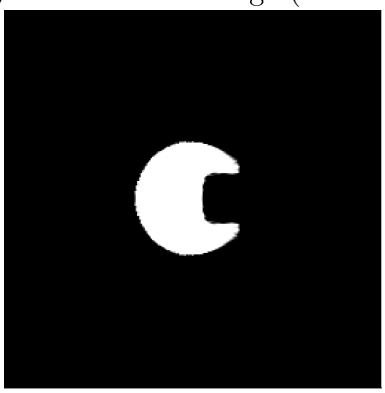

(a) Transformed image ($\lambda = 1000$)

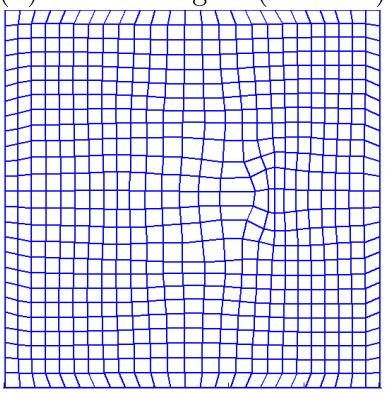

(b) Deformed grid ($\lambda = 1000$)

Figure 7.4: Results with various values of λ keeping the value of $\mu = 100$.

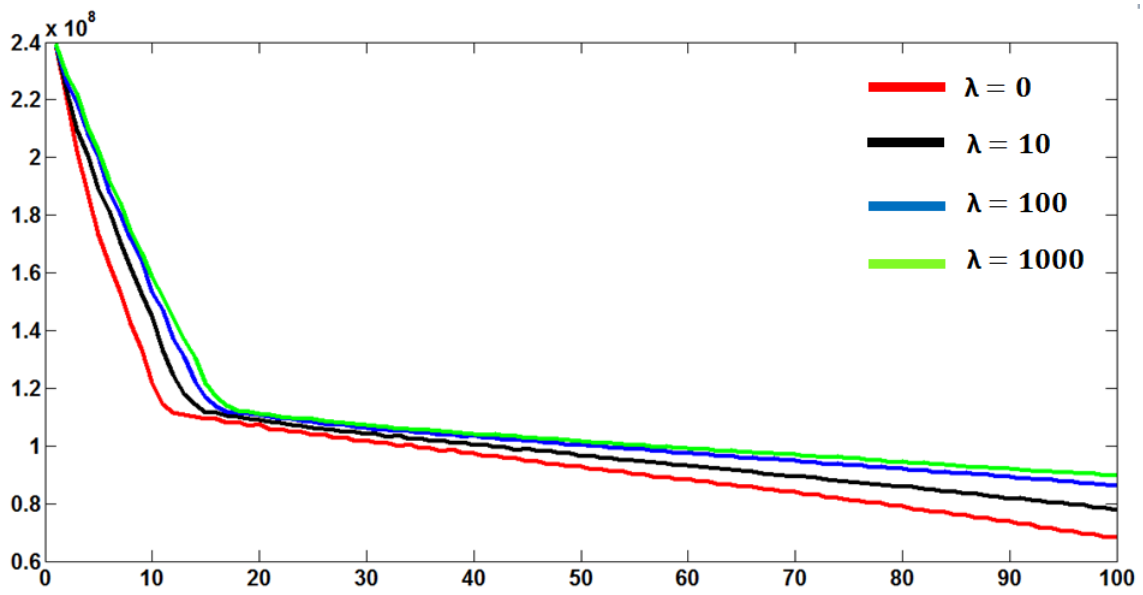

Figure 7.5: SSD versus number of iterations with $\lambda = 0, 10, 100$ and 1000. The value of μ is kept constant at 100.

After investigating the role of μ, we study the effect of λ on the registration process. The source and the target image are kept the same. The images are registered with each other using classic elastic registration keeping μ at a constant value of 100 while varying the value of λ=0, 10, 100 and 1000. The algorithm is run for 100 iterations during the registration process without any stopping criteria. For a fixed value of μ, the Young's modulus and the Poisson ratio, both are montonically increasing functions of λ. We can see from Figure 7.4 that as the value of λ increases, the body becomes more rigid. Figure 7.5 shows that the solution remains stable, irrespective of the choice of λ. Even if λ is kept at zero, the external forces do not take control of the solution as long as the value of μ is moderately large. Hence in our elastic and fluid registration model, we keep $\lambda = 0$. Keeping $\lambda = 0$ ensures that a tensile stress produces only a stretch without a lateral shrink during registration.

The different values of μ and λ has a similar effect on the fluid registration process as the Navier-Stoke equations are also based on the principle of linear elasticity.

Appendix D

Quantifying the Effects of Topology and Rigidity Preservation

In this Appendix, we present the experiments that were conducted to quantify the effects of the individual physical constraints on the elastic registration algorithm. We use the following versions of the elastic registration method:

1. Elastic with rigidity constraint
2. Elastic with topology constraint
3. Classic elastic alone (results carried forward from earlier section)

The algorithms were tested on a set of five 3D NCAT images generated at different breathing stages, starting from full expiration to full inspiration. The generated images have a resolution of 192×192×192 with an isotropic voxel size of 0.48 mm. Gaussian noise with zero mean and a variance of 0.05 has been added to the images. All the images are registered to the first frame. The Lamé parameters are set as $\lambda = 0$ and $\mu = 100$. The filter for rigidity preservation is applied every two iterations and the topology preserving constraint weighing factor (γ) is set as 0.25.

Evaluation and Results

The effect of the individual physical constriants is evaluated in terms of:

1. Percentage of negative Jacobians
2. Average Overlap of the various organs after registration

3. Jacobian values of the bones after registration

These evaluations provide a thorough analysis of the effects of individual physical constraints.

Method \ Organ	Lungs	Ribs	Spine	Liver	Average
Before registration	0.8339	0.7797	0.9355	0.7342	0.8208
Classic elastic	0.9820	0.9021	0.9214	0.9211	0.9316
Elastic (topology)	0.9834	0.9121	0.9235	0.9317	0.9376
Elastic (rigidity)	0.9765	0.9653	0.9547	0.9551	0.9630

Table 7.1: Average overlap (Dice coefficient) of the individual organs for the NCAT phantom experiment.

Pairs of registered images	Elasticity with rigidity	Elastic with topology	Classic Elastic
2nd to 1st frame	0.39%	0.0005%	0.39%
3rd to 1st frame	1.2%	0.00082%	1.1%
4th to 1st frame	2.2%	0.002%	1.8%
5th to 1st frame	3.9%	0.0089%	3.1%

Table 7.2: Percentage of negative Jacobian values

Pairs of registered images	Elasticity with rigidity	Elastic with topology	Classic Elastic
2nd to 1st frame	1.01	1.11	1.10
3rd to 1st frame	1.02	1.13	1.14
4th to 1st frame	1.04	1.19	1.16
5th to 1st frame	1.05	1.25	1.21

Table 7.3: Jacobian values for the bones after registration.

Effects of topology preserving constraint

The topology preserving constraint starts playing an important role in the force component only after the deformation experiences a large local volume change. In Table 7.1 we see that

the average overlaps for the classic elastic and elastic with topology preserving constraint are not very different (Average overlap for classic elastic=0.9316 and for elastic with topology preserving constraint=0.9376). Hence, it can be confirmed that the topology preserving constraint does not the affect the ability of the elastic transformation model to deform.

In terms of the negative Jacobians values, the topology preserving constraint reduces the percentage of negative Jacobian values in comparison to the other two methods. For all the registrations the percentage of negative Jacobians is close to zero as shown in Table 7.2. For the Jacobian values of the bones, the elastic with topology preserving constraint has a similar effect as the classic elastic method. The bones undergo deformation and have an average Jacobian value of 1.17.

Effects of rigidity preserving constraint

The rigidity preservation term has an important effect on the average overlap measures. The elastic with rigidity preserving constraint method has an average overlap of 0.9630 which is higher than the average overlaps for classic elastic and elastic with topology preserving term. The reason for this improvement in the average overlap is the better alignment of the rigid structures of the ribs and the spine which helps to boost the overall average overlap as shown in Table 7.1. The rigidity constraint has performed well in preventing any deformation in the bones as seen from the Jacobian values of Table 7.3.

But there is a drawback generated due to the introduction of the rigidity preserving constraint to the elastic method. The folding of the deformation field is slightly increased in comparison to the classic elastic method as seen in Table 7.2. This increase in negative Jacobians is a result of the filtering effect of the rigidity preserving constraint at the boundaries of the bones. This effect can only be countered by combining the topology preserving constraint with the rigidity preserving constraint.

Bibliography

[1] A. Jemal, R. Siegel, E. Ward, Y. Hao, J. Xu, T. Murray, and M. Thun, "Cancer statistics, 2008," *CA: A Cancer Journal for Clinicians*, vol. 58, no. 2, pp. 71–96, 2008.

[2] B. F. F. D. M. C. Ferlay J, Shin HR and P. DM. (2011, Sep.) Cancer incidence and mortality worldwide: Iarc cancerbase no. 10 @ONLINE. [Online]. Available: http://globocan.iarc.fr

[3] R. for International Tobacco Control, *WHO report on the global tobacco epidemic, 2008*. World Health Organization, 2008.

[4] R. Twombly, "Tobacco use a leading global cancer risk, report says," *Journal of the National Cancer Institute*, vol. 95, no. 1, pp. 11–12, 2003.

[5] D. Parkin, F. Bray, J. Ferlay, and P. Pisani, "Global cancer statistics, 2002," *CA: a cancer journal for clinicians*, vol. 55, no. 2, pp. 74–108, 2005.

[6] C. Toh and W. Lim, "Lung cancer in never-smokers," *Journal of Clinical Pathology*, vol. 60, no. 4, pp. 337–340, 2007.

[7] L. Collins, C. Haines, R. Perkel, R. Enck *et al.*, "Lung cancer: diagnosis and management." *American Family Physician*, vol. 75, no. 1, p. 56, 2007.

[8] R. Siegel, D. Naishadham, and A. Jemal, "Cancer statistics, 2012," *CA: A Cancer Journal for Clinicians*, 2012.

[9] R. Merrill, D. Henson, and M. Barnes, "Conditional survival among patients with carcinoma of the lung," *Chest*, vol. 116, no. 3, p. 697, 1999.

[10] C. R. UK. (2011, Sep.) Lung cancer and smoking : Cancer research uk @ONLINE. [Online]. Available: http://info.cancerresearchuk.org/cancerstats/types/lung/

[11] U. N. C. Institute. (2011, Sep.) Lung cancer trial results show mortality benefit with low-dose ct @ONLINE. [Online]. Available: http://www.cancer.gov/newscenter/pressreleases/2010/NLSTresultsRelease

[12] J. Croswell, S. Baker, P. Marcus, J. Clapp, and B. Kramer, "Cumulative incidence of false-positive test results in lung cancer screening," *Annals of Internal Medicine*, vol. 152, no. 8, pp. 505–512, 2010.

[13] G. Bastarrika, M. Garcia-Velloso, M. Lozano, U. Montes, W. Torre, N. Spiteri, A. Campo, L. Seijo, A. Alcaide, J. Pueyo *et al.*, "Early lung cancer detection using spiral computed tomography and positron emission tomography," *American journal of Respiratory and Critical Care Medicine*, vol. 171, no. 12, pp. 1378–1383, 2005.

[14] B. Fischer, U. Lassen, J. Mortensen, S. Larsen, A. Loft, A. Bertelsen, J. Ravn, P. Clementsen, A. Høgholm, K. Larsen *et al.*, "Preoperative staging of lung cancer with combined PET–CT," *New England Journal of Medicine*, vol. 361, no. 1, pp. 32–39, 2009.

[15] G. Schmidt, M. Reiser, and A. Baur-Melnyk, "Whole-body MRI for the staging and follow-up of patients with metastasis," *European Journal of Radiology*, vol. 70, no. 3, pp. 393–400, 2009.

[16] W. De Wever, S. Stroobants, J. Coolen, and J. Verschakelen, "Integrated PET/CT in the staging of nonsmall cell lung cancer: technical aspects and clinical integration," *European Respiratory Journal*, vol. 33, no. 1, pp. 201–212, 2009.

[17] L. W. Goldman, "Principles of ct and ct technology," *Journal of nuclear medicine technology*, vol. 35, no. 3, pp. 115–128, 2007.

[18] J. Hsieh, *Computed tomography: principles, design, artifacts, and recent advances*. Society of Photo Optical, 2003, vol. 114.

[19] W. Hu, Y. Chen, and S. Tian, "The value of high-resolution ct in diagnosis of small peripheral lung cancer," *Yixue Yingxiangxue Zazhi(Journal of Medical Imaging)*, vol. 18, no. 2, pp. 129–131, 2008.

[20] T. Suwatanapongched and D. Gierada, "CT of thoracic lymph nodes. part I: anatomy and drainage," *British Journal of Radiology*, vol. 79, no. 947, pp. 922–928, 2006.

[21] P. Garrett, S. Meshkov, and G. Perlmutter, "Oral contrast agents in CT of the abdomen." *Radiology*, vol. 153, no. 2, pp. 545–546, 1984.

[22] M. Steiner, "PET–The history behind the technology," *Senior Thesis Projects, 1993-2002*, p. 107, 2002.

[23] M. Wernick and J. Aarsvold, *Emission tomography: the fundamentals of PET and SPECT*. Academic Press, 2004.

[24] H. van Tinteren, O. Hoekstra, E. Smit, J. van den Bergh, A. Schreurs, R. Stallaert, P. van Velthoven, E. Comans, F. Diepenhorst, P. Verboom *et al.*, "Effectiveness of positron emission tomography in the preoperative assessment of patients with suspected non-small-cell lung cancer: the plus multicentre randomised trial," *The Lancet*, vol. 359, no. 9315, pp. 1388–1392, 2002.

[25] E. Weng, L. Tran, S. Rege, A. Safa, A. Sadeghi, G. Juillard, R. Mark, S. Santiago, C. Brown, and M. Mandelkern, "Accuracy and clinical impact of mediastinal lymph node staging with fdg-pet imaging in potentially resectable lung cancer," *American Journal of Clinical Oncology*, vol. 23, no. 1, p. 47, 2000.

[26] D. J. Brenner and E. J. Hall, "Computed tomography an increasing source of radiation exposure," *New England Journal of Medicine*, vol. 357, no. 22, pp. 2277–2284, 2007.

[27] F. A. Mettler, W. Huda, T. T. Yoshizumi, and M. Mahesh, "Effective doses in radiology and diagnostic nuclear medicine: a catalog1," *Radiology*, vol. 248, no. 1, pp. 254–263, 2008.

[28] K. Mah, C. Caldwell, Y. Ung, C. Danjoux, J. Balogh, S. Ganguli, L. Ehrlich, and R. Tirona, "The impact of FDG-PET on target and critical organs in CT-based treatment planning of patients with poorly defined non-small-cell lung carcinoma: a prospective study," *International Journal of Radiation Oncology, Biology and Physics*, vol. 52, no. 2, pp. 339–350, 2002.

[29] C. Greco, K. Rosenzweig, G. Cascini, and O. Tamburrini, "Current status of PET/CT for tumour volume definition in radiotherapy treatment planning for non-small cell lung cancer (NSCLC)," *Lung Cancer*, vol. 57, no. 2, pp. 125–134, 2007.

[30] K. Wu, Y. Ung, J. Hornby, M. Freeman, D. Hwang, M. Tsao, M. Dahele, G. Darling, D. Maziak, R. Tirona *et al.*, "PET CT thresholds for radiotherapy target definition in non-small-cell lung cancer: how close are we to the pathologic findings?" *International Journal of Radiation Oncology,Biology and Physics*, vol. 77, no. 3, pp. 699–706, 2010.

[31] C. Hargrave, "Image acquisition and manipulation protocols for CT-PET fusion to improve the accuracy of gross tumour volume localisation for 3d conformal radiotherapy for lung cancer," *Master of research thesis, University of Queensland*, 2010.

[32] T. Nishioka, T. Shiga, H. Shirato, E. Tsukamoto, K. Tsuchiya MD, T. Kato, K. Ohmori, A. Yamazaki, H. Aoyama, S. Hashimoto *et al.*, "Image fusion between FDG-PET and MRI/CT for radiotherapy planning of oropharyngeal and nasopharyngeal carcinomas," *International Journal of Radiation Oncology, Biology and Physics*, vol. 53, no. 4, pp. 1051–1057, 2002.

[33] M. MacManus, U. Nestle, K. Rosenzweig, I. Carrio, C. Messa, O. Belohlavek, M. Danna, T. Inoue, E. Deniaud-Alexandre, S. Schipani *et al.*, "Use of PET and PET/CT for radiation therapy planning: IAEA expert report 2006–2007," *Radiotherapy and Oncology*, vol. 91, no. 1, pp. 85–94, 2009.

[34] A. Pfannenberg, P. Aschoff, K. Brechtel, M. Müller, M. Klein, R. Bares, C. Claussen, and S. Eschmann, "Value of contrast-enhanced multiphase CT in combined PET/CT

protocols for oncological imaging," *British Journal of Radiology*, vol. 80, no. 954, pp. 437–445, 2007.

[35] A. Pfannenberg, P. Aschoff, K. Brechtel, M. Müller, R. Bares, F. Paulsen, J. Scheiderbauer, G. Friedel, C. Claussen, and S. Eschmann, "Low dose non-enhanced CT versus standard dose contrast-enhanced CT in combined PET/CT protocols for staging and therapy planning in non-small cell lung cancer," *European journal of nuclear medicine and molecular imaging*, vol. 34, no. 1, pp. 36–44, 2007.

[36] O. Mawlawi, J. Erasmus, R. Munden, T. Pan, A. Knight, H. Macapinlac, D. Podoloff, and M. Chasen, "Quantifying the effect of IV contrast media on integrated PET/CT: clinical evaluation," *American Journal of Roentgenology*, vol. 186, no. 2, pp. 308–319, 2006.

[37] J. Fox, R. Rengan, W. O'Meara, E. Yorke, Y. Erdi, S. Nehmeh, S. Leibel, and K. Rosenzweig, "Does registration of PET and planning CT images decrease interobserver and intraobserver variation in delineating tumor volumes for non-small-cell lung cancer?" *International Journal of Radiation Oncology, Biology and Physics*, vol. 62, no. 1, pp. 70–75, 2005.

[38] R. Steenbakkers, J. Duppen, I. Fitton, K. Deurloo, L. Zijp, E. Comans, A. Uitterhoeve, P. Rodrigus, G. Kramer, J. Bussink *et al.*, "Reduction of observer variation using matched ct-pet for lung cancer delineation: a three-dimensional analysis," *International Journal of Radiation Oncology, Biology and Physics*, vol. 64, no. 2, pp. 435–448, 2006.

[39] L. Brown, "A survey of image registration techniques," *ACM computing surveys (CSUR)*, vol. 24, no. 4, pp. 325–376, 1992.

[40] J. Maintz and M. Viergever, "A survey of medical image registration," *Medical Image Analysis*, vol. 2, no. 1, pp. 1–36, 1998.

[41] A. El-Baz, G. Gimel'farb, R. Falk, E. Abo *et al.*, "Automatic analysis of 3D low dose CT images for early diagnosis of lung cancer," *Pattern Recognition*, vol. 42, no. 6, pp. 1041–1051, 2009.

[42] V. Gorbunova, P. Lo, H. Ashraf, A. Dirksen, M. Nielsen, and M. de Bruijne, "Weight preserving image registration for monitoring disease progression in lung CT," *Medical Image Computing and Computer-Assisted Intervention–MICCAI 2008*, pp. 863–870, 2008.

[43] F. Bookstein, "Principal warps: Thin-plate splines and the decomposition of deformations," *Pattern Analysis and Machine Intelligence, IEEE Transactions on*, vol. 11, no. 6, pp. 567–585, 1989.

[44] D. Rueckert, L. Sonoda, C. Hayes, D. Hill, M. Leach, and D. Hawkes, "Nonrigid registration using free-form deformations: application to breast MR images," *IEEE Transactions on Medical Imaging*, vol. 18, no. 8, pp. 712–721, 1999.

[45] W. Grimson, "A computational theory of visual surface interpolation," *Philosophical Transactions of the Royal Society of London. B, Biological Sciences*, vol. 298, no. 1092, pp. 395–427, 1982.

[46] R. Wiemker, K. Rohr, L. Binder, R. Sprengel, and H. Stiehl, "Application of elastic registration to imagery from airborne scanners," *International Archives of Photogrammetry and Remote Sensing*, vol. 31, pp. 949–954, 1996.

[47] A. Klein, J. Andersson, B. Ardekani, J. Ashburner, B. Avants, M. Chiang, G. Christensen, D. Collins, J. Gee, P. Hellier *et al.*, "Evaluation of 14 nonlinear deformation algorithms applied to human brain MRI registration," *Neuroimage*, vol. 46, no. 3, pp. 786–802, 2009.

[48] K. Rohr, M. Fornefett, and H. Stiehl, "Spline-based elastic image registration: integration of landmark errors and orientation attributes," *Computer Vision and Image Understanding*, vol. 90, no. 2, pp. 153–168, 2003.

[49] M. Fornefett, K. Rohr, and H. Stiehl, "Radial basis functions with compact support for elastic registration of medical images," *Image and Vision Computing*, vol. 19, no. 1, pp. 87–96, 2001.

[50] Y. Amit, "A nonlinear variational problem for image matching," *SIAM Journal on Scientific Computing*, vol. 15, no. 1, pp. 207–224, 1994.

[51] M. Holden, "A review of geometric transformations for nonrigid body registration," *IEEE Transactions on Medical Imaging*, vol. 27, no. 1, pp. 111–128, 2008.

[52] B. Li, G. E. Christensen, E. A. Hoffman, G. McLennan, and J. M. Reinhardt, "Pulmonary ct image registration and warping for tracking tissue deformation during the respiratory cycle through 3d consistent image registration," *Medical physics*, vol. 35, no. 12, p. 5575, 2008.

[53] J. Ehrhardt, R. Werner, A. Schmidt-Richberg, and H. Handels, "Automatic landmark detection and non-linear landmark-and surface-based registration of lung ct images," *Medical Image Analysis for the Clinic-A Grand Challenge, MICCAI 2010*, pp. 165–174, 2010.

[54] C. Broit, "Optimal registration of deformed images," *Electrical Engineering PhD. Dissertation,University of Pennsylvania*, 1981.

[55] R. Bajcsy and S. Kovacic, "Multiresolution elastic matching," *Computer Vision, Graphics, and Image Processing*, vol. 46, no. 1, pp. 1–21, 1989.

[56] G. Christensen, "Deformable shape models for anatomy," Ph.D. dissertation, Washington University, 1994.

[57] B. Horn and B. Schunck, "Determining optical flow," *Artificial Intelligence*, vol. 17, no. 1-3, pp. 185–203, 1981.

[58] J. Modersitzki, *Numerical methods for image registration*. Oxford University Press, USA, 2004.

[59] B. Fischer and J. Modersitzki, "A unified approach to fast image registration and a new curvature based registration technique," *Linear Algebra and its applications*, vol. 380, pp. 107–124, 2004.

[60] B. Zitova and J. Flusser, "Image registration methods: a survey," *Image and Vision Computing*, vol. 21, no. 11, pp. 977–1000, 2003.

[61] M. Holden, D. Hill, E. Denton, J. Jarosz, T. Cox, T. Rohlfing, J. Goodey, and D. Hawkes, "Voxel similarity measures for 3-D serial MR brain image registration," *IEEE Transactions on Medical Imaging*, vol. 19, no. 2, pp. 94–102, 2000.

[62] A. Collignon, F. Maes, D. Delaere, D. Vandermeulen, P. Suetens, and G. Marchal, "Automated multi-modality image registration based on information theory," in *Information Processing in Medical Imaging*, vol. 14, no. 6. Dordrecht, The Netherlands: Kluwer, 1995, p. 263.

[63] W. Wells III, P. Viola, H. Atsumi, S. Nakajima, and R. Kikinis, "Multi-modal volume registration by maximization of mutual information," *Medical Image Analysis*, vol. 1, no. 1, pp. 35–51, 1996.

[64] C. Studholme, D. Hill, and D. Hawkes, "An overlap invariant entropy measure of 3D medical image alignment," *Pattern Recognition*, vol. 32, no. 1, pp. 71–86, 1999.

[65] D. Rueckert, A. Frangi, and J. Schnabel, "Automatic construction of 3-D statistical deformation models of the brain using nonrigid registration," *Medical Imaging, IEEE Transactions on*, vol. 22, no. 8, pp. 1014–1025, 2003.

[66] Z. Knops, J. Maintz, M. Viergever, and J. Pluim, "Normalized mutual information based registration using k–means clustering and shading correction," *Medical Image Analysis*, vol. 10, no. 3, pp. 432–439, 2006.

[67] Z. Gao, B. Gu, and J. Lin, "Monomodal image registration using mutual information based methods," *Image and Vision Computing*, vol. 26, no. 2, pp. 164–173, 2008.

[68] A. Andronache, M. Von Siebenthal, G. Székely, and P. Cattin, "Non-rigid registration of multi-modal images using both mutual information and cross-correlation," *Medical Image Analysis*, vol. 12, no. 1, pp. 3–15, 2008.

[69] A. Collignon, D. Vandermeulen, P. Suetens, and G. Marchal, "3D multi-modality medical image registration using feature space clustering," in *Computer Vision, Virtual Reality and Robotics in Medicine*. Springer, 1995, pp. 193–204.

[70] X. Huang, N. Hill, J. Ren, and T. Peters, "Rapid registration of multimodal images using a reduced number of voxels," in *Proceedings of the SPIE: The International Society for Optical Engineering*, vol. 6141, 2006, p. 614116.

[71] K. Ding, "Regional lung function and mechanics using image registration," Ph.D. dissertation, 2010.

[72] S. Schafer, A. Uneri, D. Mirota, S. Nithiananthan, J. Stayman, W. Zbijewski, G. Kleinszig, C. Schmidgunst, M. Sussman, and J. Siewerdsen, "Mo-d-brc-02: Image guidance in video-assisted thoracoscopic surgery (vats) using a mobile c-arm for cone-beam ct: Image quality, dose, and first experience in visualizing the fully deflated lung," *Medical Physics*, vol. 38, p. 3712, 2011.

[73] R. Sweeney, B. Seubert, S. Stark, V. Homann, G. Müller, M. Flentje, and M. Guckenberger, "Accuracy and inter-observer variability of 3d versus 4d cone-beam ct based image-guidance in sbrt for lung tumors," *Radiation Oncology*, vol. 7, no. 1, p. 81, 2012.

[74] K. Murphy, B. Van Ginneken, J. Reinhardt, S. Kabus, K. Ding, X. Deng, K. Cao, K. Du, G. Christensen, V. Garcia *et al.*, "Evaluation of Registration Methods on Thoracic CT: The EMPIRE10 Challenge." *IEEE transactions on Medical Imaging*, vol. 30, no. 11, p. 1901, 2011.

[75] G. Song, N. Tustison, B. Avants, and J. Gee, "Lung CT image registration using diffeomorphic transformation models," *Medical Image Analysis for the Clinic: A Grand Challenge*, pp. 23–32, 2010.

[76] B. Avants, N. Tustison, G. Song, P. Cook, A. Klein, and J. Gee, "A reproducible evaluation of ANTs similarity metric performance in brain image registration," *Neuroimage*, vol. 54, no. 3, pp. 2033–2044, 2011.

[77] D. Loeckx, D. Smeets, J. Keustermans, J. Hermans, F. Maes, D. Vandermeulen, and P. Suetens, "3d lung registration using splinemirit and robust tree registration (rtr)," *Medical Image Analysis for the Clinic: A Grand Challenge*, pp. 109–117, 2010.

[78] S. Kabus and C. Lorenz, "Fast elastic image registration," *Medical Image Analysis for the Clinic: A Grand Challenge*, pp. 81–89, 2010.

[79] M. Heinrich, C. Jenkinson, M. Brady, and J. Schnabel, "Discontinuity preserving regularisation for variational optical flow registration using the modified Lp norm," *Medical Image Analysis for the Clinic: A Grand Challenge*, 2010.

[80] X. Han, "Feature-constrained nonlinear registration of lung CT images," *Medical Image Analysis for the Clinic: A Grand Challenge*, pp. 63–72, 2010.

[81] K. Cao, K. Du, K. Ding, J. Reinhardt, and G. Christensen, "Regularized nonrigid registration of lung ct images by preserving tissue volume and vesselness measure," *Medical Image Analysis for the Clinic: A Grand Challenge*, pp. 43–54, 2010.

[82] J. Ehrhardt, R. Werner, A. Schmidt-Richberg, and H. Handels, "Statistical modeling of 4D respiratory lung motion using diffeomorphic image registration," *IEEE Transactions on Medical Imaging*, vol. 30, no. 2, pp. 251–265, 2011.

[83] M. Urschler, M. Werlberger, E. Scheurer, and H. Bischof, "Robust optical flow based deformable registration of thoracic CT images," *Medical Image Analysis for the Clinic: A Grand Challenge*, pp. 195–204, 2010.

[84] Z. Wu, E. Rietzel, V. Boldea, D. Sarrut, and G. Sharp, "Evaluation of deformable registration of patient lung 4dct with subanatomical region segmentations," *Medical physics*, vol. 35, p. 775, 2008.

[85] M. Staring, S. Klein, and J. Pluim, "Nonrigid registration with adaptive content-based filtering of the deformation field," in *Proc. SPIE*, vol. 5747, 2005, pp. 212–221.

[86] C. Davatzikos, M. Vaillant, S. Resnick, J. Prince, S. Letovsky, and R. Bryan, "A computerized approach for morphological analysis of the corpus callosum," *Journal of Computer Assisted Tomography*, vol. 20, no. 1, p. 88, 1996.

[87] J. Gee, M. Reivich, and R. Bajcsy, "Elastically deforming a three-dimensional atlas to match anatomical brain images," *Technical report, University of Pennsylvania*, 1993.

[88] R. LAMBERT and T. Wilson, "A model for the elastic properties of the lung and their effect on expiratory flow," *Journal of Applied Physiology*, vol. 34, pp. 34–48, 1973.

[89] M. Bro-Nielsen and C. Gramkow, "Fast fluid registration of medical images," in *Visualization in Biomedical Computing*. Springer, 1996, pp. 265–276.

[90] G. Wollny and F. Kruggel, "Computational cost of nonrigid registration algorithms based on fluid dynamics [MRI time series application]," *IEEE Transactions on Medical Imaging*, vol. 21, no. 8, pp. 946–952, 2002.

[91] B. Fischer and J. Modersitzki, "Fast inversion of matrices arising in image processing," *Numerical Algorithms*, vol. 22, no. 1, pp. 1–11, 1999.

[92] R. Gonzalez, R. Woods, and S. Eddins, "Digital image processing using matlab. 2004," *Publishing House of Electronics Industry*.

[93] S. Joshi and M. Miller, "Landmark matching via large deformation diffeomorphisms," *IEEE Transactions on Image Processing*, vol. 9, no. 8, pp. 1357–1370, 2000.

[94] C. Twining and S. Marsland, "Constructing diffeomorphic representations of non-rigid registrations of medical images," in *Information Processing in Medical Imaging*. Springer, 2003, pp. 413–425.

[95] G. Christensen and H. Johnson, "Consistent image registration," *IEEE Transactions on Medical Imaging*, vol. 20, no. 7, pp. 568–582, 2001.

[96] D. Rueckert, P. Aljabar, R. Heckemann, J. Hajnal, and A. Hammers, "Diffeomorphic registration using B-splines," *Medical Image Computing and Computer-Assisted Intervention–MICCAI 2006*, pp. 702–709, 2006.

[97] S. Chun and J. Fessler, "Regularized methods for topology-preserving smooth non-rigid image registration using B-spline basis," in *5th IEEE International Symposium on Biomedical Imaging: From Nano to Macro, 2008. ISBI 2008.* IEEE, 2008, pp. 1099–1102.

[98] T. Vercauteren, X. Pennec, A. Perchant, and N. Ayache, "Diffeomorphic demons: Efficient non-parametric image registration," *NeuroImage*, vol. 45, no. 1, pp. S61–S72, 2009.

[99] I. Yanovsky, P. Thompson, S. Osher, and A. Leow, "Topology preserving log-unbiased nonlinear image registration: Theory and implementation," in *IEEE Conference on Computer Vision and Pattern Recognition, 2007. CVPR'07.* IEEE, 2007, pp. 1–8.

[100] J. Little, D. Hill, and D. Hawkes, "Deformations incorporating rigid structures [medical imaging]," in *Proceedings of the Workshop on Mathematical Methods in Biomedical Image Analysis, 1996.* IEEE, 1996, pp. 104–113.

[101] P. Edwards, D. Hill, J. Little, and D. Hawkes, "A three-component deformation model for image-guided surgery," *Medical Image Analysis*, vol. 2, no. 4, pp. 355–367, 1998.

[102] M. Ferrant, A. Nabavi, B. Macq, F. Jolesz, R. Kikinis, and S. Warfield, "Registration of 3-D intraoperative MR images of the brain using a finite-element biomechanical model," *IEEE Transactions on Medical Imaging*, vol. 20, no. 12, pp. 1384–1397, 2001.

[103] H. Lester, S. Arridge, K. Jansons, L. Lemieux, J. Hajnal, and A. Oatridge, "Non-linear registration with the variable viscosity fluid algorithm," in *Information Processing in Medical Imaging.* Springer, 1999, pp. 238–251.

[104] C. Tanner, J. Schnabel, D. Chung, M. Clarkson, D. Rueckert, D. Hill, and D. Hawkes, "Volume and shape preservation of enhancing lesions when applying non-rigid regis-

tration to a time series of contrast enhancing MR breast images," in *Medical Image Computing and Computer-Assisted Intervention–MICCAI 2000*. Springer, 2000.

[105] J. Miller, G. Gopalakrishnan, M. Datar, P. Mendonça, and R. Mullick, "Deformable registration with spatially varying degrees of freedom constraints," in *5th IEEE International Symposium on Biomedical Imaging: From Nano to Macro, 2008. ISBI 2008.* IEEE, 2008, pp. 1163–1166.

[106] W. Segars, "Development and application of the new dynamic NURBS– based cardio–torso (NCAT) phantom." *Heart*, 2001.

[107] E. van Rikxoort, B. de Hoop, M. Viergever, M. Prokop, and B. van Ginneken, "Automatic lung segmentation from thoracic computed tomography scans using a hybrid approach with error detection," *Medical Physics*, vol. 36, p. 2934, 2009.

[108] E. van Rikxoort, B. van Ginneken, M. Klik, and M. Prokop, "Supervised enhancement filters: application to fissure detection in chest CT scans," *IEEE Transactions on Medical Imaging*, vol. 27, no. 1, pp. 1–10, 2008.

[109] K. Murphy, B. van Ginneken, J. Pluim, S. Klein, and M. Staring, "Semi-automatic reference standard construction for quantitative evaluation of lung CT registration," *Medical Image Computing and Computer-Assisted Intervention–MICCAI 2008*, pp. 1006–1013, 2008.

[110] R. Doe. (2009, Jun.) This is a test entry of type @ONLINE. [Online]. Available: http://www.test.org/doe/

[111] V. M. Centre. (2012, Jun.) Pleural effusion @ONLINE. [Online]. Available: http://www.virtualmedicalcentre.com/diseases/pleural-effusion/25/

[112] J. von Berg, H. Barschdorf, T. Blaffert, S. Kabus, and C. Lorenz, "Surface based cardiac and respiratory motion extraction for pulmonary structures from multi-phase CT," in *Proceedings of SPIE*, vol. 6511, 2007, p. 65110Y.

[113] T. Vik, S. Kabus, J. von Berg, K. Ens, S. Dries, T. Klinder, and C. Lorenz, "Validation and comparison of registration methods for free–breathing 4D lung–CT," in *Proc. of SPIE Medical Imaging*, vol. 6914, 2008, pp. 69 142P1–10.

[114] A. Al-Mayah, J. Moseley, and K. Brock, "Contact surface and material nonlinearity modeling of human lungs," *Physics in Medicine and Biology*, vol. 53, p. 305, 2008.

[115] R. Werner, J. Ehrhardt, R. Schmidt, and H. Handels, "Patient-specific finite element modeling of respiratory lung motion using 4D CT image data," *Medical physics*, vol. 36, p. 1500, 2009.

[116] Y. Xie, M. Chao, and L. Xing, "Tissue feature-based and segmented deformable image registration for improved modeling of shear movement of lungs," *International Journal of Radiation Oncology* Biology* Physics*, vol. 74, no. 4, pp. 1256–1265, 2009.

[117] H. Nagel and W. Enkelmann, "An investigation of smoothness constraints for the estimation of displacement vector fields from image sequences," *IEEE Transactions on-Pattern Analysis and Machine Intelligence,*, no. 5, pp. 565–593, 1986.

[118] D. Sun, S. Roth, J. Lewis, and M. Black, "Learning optical flow," *Computer Vision–ECCV 2008*, pp. 83–97, 2008.

[119] H. Zimmer, A. Bruhn, J. Weickert, L. Valgaerts, A. Salgado, B. Rosenhahn, and H. Seidel, "Complementary optic flow," in *Energy minimization methods in computer vision and pattern recognition*. Springer, 2009, pp. 207–220.

[120] M. Heinrich, M. Jenkinson, M. Brady, and J. Schnabel, "Discontinuity preserving regularisation for variational optical-flow registration using the modified Lp norm," *Medical Image Analysis for the Clinic: A Grand Challenge*, pp. 185–194, 2010.

[121] D. Ruan, S. Esedoglu, and J. Fessler, "Discriminative sliding preserving regularization in medical image registration," in *IEEE International Symposium on Biomedical Imaging: From Nano to Macro, 2009. ISBI'09.* IEEE, 2009, pp. 430–433.

[122] A. Schmidt-Richberg, J. Ehrhardt, R. Werner, and H. Handels, "Slipping objects in image registration: Improved motion field estimation with direction-dependent regularization," *Medical Image Computing and Computer-Assisted Intervention–MICCAI 2009*, pp. 755–762, 2009.

[123] V. Delmon, S. Rit, R. Pinho, and D. Sarrut, "Direction dependent B-splines decomposition for the registration of sliding objects," *Fourth International Workshop on Pulmonary Image analysis*, 2011.

[124] D. Pace, A. Enquobahrie, H. Yang, S. Aylward, and M. Niethammer, "Deformable image registration of sliding organs using anisotropic diffusive regularization," in *International Symposium on Biomedical Imaging: From Nano to Macro, 2011 IEEE*. IEEE, 2011, pp. 407–413.

[125] L. Risser, H. Baluwala, and J. Schnabel, "Diffeomorphic registration with sliding conditions: Application to the registration of lungs CT images." *Fourth International Workshop on Pulmonary Image analysis*, 2011.

[126] Y. Yin, E. Hoffman, and C. Lin, "Lung lobar slippage assessed with the aid of image registration," *Medical Image Computing and Computer-Assisted Intervention–MICCAI 2010*, pp. 578–585, 2010.

[127] A. Schmidt-Richberg, R. Werner, H. Handels, and J. Ehrhardt, "Estimation of slipping organ motion by registration with direction-dependent regularization," *Medical Image Analysis*, 2011.

[128] J. Vandemeulebroucke, S. Rit, J. Kybic, and P. Sarrut, "Spatio-temporal motion estimation for respiratory-correlated imaging of the lungs," *framework*, vol. 20, no. 21, p. 25, 2010.

[129] T. Yoo, *Insight into images: principles and practice for segmentation, registration, and image analysis*. AK Peters Wesllesley^ eMassachusetts Massachusetts, 2004, vol. 203.

[130] J. Sieren, Y. Ohno, H. Koyama, K. Sugimura, and G. McLennan, "Recent technological and application developments in computed tomography and magnetic resonance imaging for improved pulmonary nodule detection and lung cancer staging," *Journal of Magnetic Resonance Imaging*, vol. 32, no. 6, pp. 1353–1369, 2010.

[131] Y. Tai, K. Lin, C. Hoh, S. Huang, and E. Hoffman, "Utilization of 3-d elastic transformation in the registration of chest X-ray CT and whole body PET," *IEEE Transactions on Nuclear Science*, vol. 44, no. 4, pp. 1606–1612, 1997.

[132] R. Shekhar, V. Walimbe, S. Raja, V. Zagrodsky, M. Kanvinde, G. Wu, and B. Bybel, "Automated 3-dimensional elastic registration of whole-body PET and CT from separate or combined scanners," *Journal of Nuclear Medicine*, vol. 46, no. 9, pp. 1488–1496, 2005.

[133] D. Mattes, D. Haynor, H. Vesselle, T. Lewellen, and W. Eubank, "PET-CT image registration in the chest using free-form deformations," *IEEE Transactions on Medical Imaging*, vol. 22, no. 1, pp. 120–128, 2003.

[134] O. Camara, G. Delso, O. Colliot, A. Moreno-Ingelmo, and I. Bloch, "Explicit incorporation of prior anatomical information into a nonrigid registration of thoracic and abdominal CT and 18-FDG whole-body emission pet images," *IEEE Transactions on Medical Imaging*, vol. 26, no. 2, pp. 164–178, 2007.

[135] S. Chambon, A. Moreno, A. Santhanam, J. Rolland, E. Angelini, I. Bloch *et al.*, "CT-PET landmark-based lung registration using a dynamic breathing model," *International conference on Image Analysis and Processing*, 2007.

[136] A. Moreno, S. Chambon, A. Santhanam, R. Brocardo, P. Kupelian, J. Rolland, E. Angelini, and I. Bloch, "Thoracic CT-PET registration using a 3D breathing model," *Medical Image Computing and Computer-Assisted Intervention–MICCAI 2007*, pp. 626–633, 2007.

[137] P. Slomka, D. Dey, C. Przetak, U. Aladl, and R. Baum, "Automated 3-dimensional registration of stand-alone 18F-FDG whole-body PET with CT," *Journal of Nuclear Medicine*, vol. 44, no. 7, pp. 1156–1167, 2003.

[138] T. Lange, T. Wenckebach, H. Lamecker, M. Seebass, M. Hünerbein, S. Eulenstein, B. Gebauer, and P. Schlag, "Registration of different phases of contrast-enhanced CT/MRI data for computer-assisted liver surgery planning: Evaluation of state-of-the-art methods," *The International Journal of Medical Robotics and Computer Assisted Surgery*, vol. 1, no. 3, pp. 6–20, 2005.

[139] A. Chandler, W. Wei, E. Anderson, D. Herron, Z. Ye, and C. Ng, "Validation of motion correction techniques for liver ct perfusion studies," *British Journal of Radiology*, 2012.

[140] C. Chefd'hotel and K. Saddi, "Method and system for registration of contrast-enhanced images with volume-preserving constraint," Nov. 27 2007, uS Patent App. 11/945,337.

[141] K. Zhai, Z. Zhu, Y. Cao, B. Wang, H. Liu, and H. Jiang, "Alternative iterations based registration for contrast-enhanced multiphase liver CT images," in *Biomedical Engineering and Informatics, 2009. BMEI'09. 2nd International Conference on.* IEEE, 2009, pp. 1–5.

[142] G. Yang, P. Burger, J. Panting, P. Gatehouse, D. Rueckert, D. Pennell, and D. Firmin, "Motion and deformation tracking for short-axis echo-planar myocardial perfusion imaging," *Medical image analysis*, vol. 2, no. 3, pp. 285–302, 1998.

[143] L. Bidaut and J. Vallée, "Automated registration of dynamic mr images for the quantification of myocardial perfusion," *Journal of magnetic resonance imaging*, vol. 13, no. 4, pp. 648–655, 2001.

[144] P. Yushkevich, J. Piven, H. Hazlett, R. Smith, S. Ho, J. Gee, and G. Gerig, "User-guided 3D active contour segmentation of anatomical structures: significantly improved efficiency and reliability," *Neuroimage*, vol. 31, no. 3, pp. 1116–1128, 2006.

[145] C. Bazan and P. Blomgren, "Image smoothing and edge detection by nonlinear diffusion and bilateral filter," *Research Report CSRCR*, vol. 21, 2007.

[146] A. Goshtasby, "On edge focusing," *Image and vision computing*, vol. 12, no. 4, pp. 247–256, 1994.

[147] J. Weickert and T. Brox, "Diffusion and regularization of vector-and matrix-valued images," *Contemporary mathematics*, vol. 313, pp. 251–268, 2002.

[148] F. Bergholm, "Edge focusing," *Pattern Analysis and Machine Intelligence, IEEE Transactions on*, no. 6, pp. 726–741, 1987.

[149] P. Perona and J. Malik, "Scale-space and edge detection using anisotropic diffusion," *Pattern Analysis and Machine Intelligence, IEEE Transactions on*, vol. 12, no. 7, pp. 629–639, 1990.

[150] E. Steen and B. Olstad, "Scale-space and boundary detection in ultrasound imaging, using signal-adaptive anisotropic diffusion," *Medical Imaging*, 1994.

[151] J. Weickert, "Theoretical foundations of anisotropic diffusion in image processing," *Computing-Wien-Supplements*, no. 11, pp. 221–236, 1996.

[152] G. Gerig, O. Kubler, R. Kikinis, and F. Jolesz, "Nonlinear anisotropic filtering of mri data," *Medical Imaging, IEEE Transactions on*, vol. 11, no. 2, pp. 221–232, 1992.

[153] J. Weickert, "A review of nonlinear diffusion filtering," *Scale-space theory in computer vision*, pp. 1–28, 1997.

[154] J. Kaftanab, A. Kiralyc, A. Bakaib, M. Dasd, C. Novakc, and T. Aacha, "Fuzzy pulmonary vessel segmentation in contrast enhanced ct data," in *Proc. of SPIE Vol*, vol. 6914, 2008, pp. 69 141Q–1.

[155] A. Kiraly, E. Pichon, D. Naidich, and C. Novak, "Analysis of arterial sub-trees affected by pulmonary emboli," 2004.